DGK Ausschuss Geodäsie (DGK)
der Bayerischen Akademie der Wissenschaften

Reihe C Dissertationen Heft Nr. 962

Asha Vincent

Clock Networks for Geodetic Applications

München 2025

Verlag der Bayerischen Akademie der Wissenschaften, München

ISSN 0065-5325 ISBN 978-3-7696-5374-8

Ausschuss Geodäsie (DGK)
der Bayerischen Akademie der Wissenschaften

Reihe C Dissertationen Heft Nr. 962

Clock Networks for Geodetic Applications

Von der Fakultät für Bauingenieurwesen und Geodäsie
der Gottfried Wilhelm Leibniz Universität Hannover
zur Erlangung des akademischen Grades
Doktor-Ingenieur (Dr.-Ing.)
genehmigte Dissertation

von

Asha Vincent, M. Sc.
geboren am 17. January 1996 in Kerala, Indien

München 2025

Verlag der Bayerischen Akademie der Wissenschaften, München

ISSN 0065-5325 ISBN 978-3-7696-5374-8

Adresse des Ausschusses Geodäsie (DGK)
der Bayerischen Akademie der Wissenschaften:

Ausschuss Geodäsie (DGK) der Bayerischen Akademie der Wissenschaften

Alfons-Goppel-Straße 11 ● D – 80 539 München

Telefon +49 – 89 – 23 031 1113 ● Telefax +49 – 89 – 23 031 - 1283 / - 1100

e-mail post@dgk.badw.de ● http://www.dgk.badw.de

Prüfungskommission:

Vorsitzender: Apl. Prof. Dr. techn. Franz Rottensteiner

Hauptreferent: Prof. Dr.-Ing. habil. Jürgen Müller

Korreferenten: Prof. Dr. rer. nat. Claus Lämmerzahl (ZARM, University of Bremen)

Prof. Dr.-Ing. habil. Monika Sester

Tag der mündlichen Prüfung: 21.05.2025

:

Diese Dissertation ist auf dem Server des Ausschusses Geodäsie (DGK)
der Bayerischen Akademie der Wissenschaften, München unter <http://dgk.badw.de/>
sowie unter Wissenschaftliche Arbeiten der Fachrichtung Geodäsie und Geoinformatik
der Leibniz Universität Hannover (ISSN 0174-1454), Nr. 411,
<https://doi.org/10.15488/19225>, Hannover 2025, elektronisch publiziert

ISSN 0065-5325 ISBN 978-3-7696-5374-8

Abstract

Relativistic geodesy enables a novel approach that utilises atomic clocks for deriving geodetic parameters. A clock lifted by 1 cm or affected by a gravity potential variation of 0.1 m^2/s^2 observes a fractional frequency change of 10^{-18}. To study the detection of time-variable gravity signals with clocks, case studies have been conducted in five regions characterised by different mass change processes: the Himalayas, Amazon, Greenland, Fennoscandia, and Japan. Clock observations, affected by both mass changes and vertical land deformations, have been simulated as gravity potential variations. In the Himalayas and Amazon, seasonal potential variations reveal regional precipitation and hydrological cycles, while in Greenland, long-term ice mass loss is captured. In Fennoscandia, glacial isostatic adjustment mainly leads to vertical deformations, and in Japan, clock measurements provide insights into co-seismic and post-seismic potential variations, illustrated for the 2011 Tōhoku earthquake. The reference clock for the comparisons was assumed to be realised by a combination of ground-based and space-based clocks in known satellite orbits, with overall uncertainties better than 10^{-18}. These case studies demonstrate the great potential of clock networks to detect subtle geophysical signals, enhancing our understanding of the Earth's dynamic processes. To realize an international height reference system, a comprehensive study using closed-loop simulations has been carried out with the goal of unifying regional/local height systems in Europe and Brazil, targeting an accuracy of 1 cm. Various error sources were investigated such as datum offsets, slopes (both in latitude and longitude direction), accumulated tilts based on the distance from reference tide gauges, and elevation-dependent errors. Clocks with fractional uncertainties of 10^{-18} and 10^{-17} were assumed, accounting for intrinsic clock uncertainties, temporal correlations, external factors like tidal effects, propagation delays, and the presence of outliers. Different clock distribution strategies were tested to determine some optimised network setup for a good estimation of these errors considering clocks at distant levelling points, reference tide gauges, and elevated locations. A network design involving master and local clocks with reduced linkages appears quite good. A unification accuracy of 1 cm can be achieved. Moreover, the unified height systems of Europe and Brazil related to the global geoid can be realised with a height accuracy of 3 cm. The third application of clock networks focuses on monitoring the global sea level, which has been increasing over several decades due to climate change. Up to now, Absolute Sea Level (ASL) changes can only be accurately determined from Relative Sea Level (RSL) measurements by properly accounting for vertical land movements at tide gauge benchmarks. Atomic clocks at these tide gauges can provide real-time, absolute physical height changes. Since RSL is affected by regional tidal datums, local variations must be considered to ensure a consistent, global ASL measurement. By incorporating land motion derived from clock observations, it is possible to establish a uniform reference datum, enabling accurate, geoid-based assessments of global sea level changes. These applications show that relativistic geodesy with clocks can revolutionize geodesy by near real-time, pointwise and direct measurements of the time-variable gravity potential.

Keywords: Atomic clocks, chronometric Geodesy, time-variable gravity, global height system, absolute sea level

Zusammenfassung

Die relativistische Geodäsie ermöglicht einen neuartigen Ansatz, bei dem Atomuhren zur Ableitung geodätischer Parameter verwendet werden. Eine Uhr, die um 1 cm angehoben wird oder bei der sich das Schwerepotential um 0,1 m^2/s^2 ändert, erfährt eine Frequenzänderung von 10^{-18}. Um die Erfassung zeitvariabler Schweresignale mit Uhren zu untersuchen, wurden Fallstudien in fünf Regionen durchgeführt, die durch unterschiedliche Massenänderungsprozesse gekennzeichnet sind: Himalaya, Amazonas, Grönland, Fennoskandien und Japan. Uhrenbeobachtungen, die sowohl von Massenänderungen als auch von vertikalen Landdeformationen beeinflusst werden, wurden als Schwerepotentialschwankungen simuliert. Im Himalaya und im Amazonasgebiet geben die saisonalen Potentialschwankungen Aufschluss über regionale Niederschläge und hydrologische Zyklen, während in Grönland der langfristige Eismassenverlust erfasst wird. In Fennoskandien führt der glazial-isostatische Ausgleichsprozess hauptsächlich zu vertikalen Deformationen, und in Japan liefern Zeitmessungen Einblicke in koseismische und postseismische Potentialschwankungen, wie sie für das Tōhoku-Erdbeben 2011 veranschaulicht wurden. Als Referenzuhr für die Vergleiche wurde eine Kombination aus boden- und weltraumgestützten Uhren in bekannten Satellitenbahnen angenommen, wobei die Gesamtunsicherheiten besser als 10^{-18} sind. Diese Fallstudien zeigen das große Potenzial von Uhrennetzwerken zur Erkennung subtiler geophysikalischer Signale, die unser Verständnis der dynamischen Prozesse der Erde verbessern. Um ein internationales Höhenreferenzsystem zu verwirklichen, wurde eine umfassende Studie mit Hilfe von Closed-Loop-Simulationen mit dem Ziel durchgeführt, regionale/lokale Höhensysteme in Europa und Brasilien zu vereinheitlichen und eine Genauigkeit von 1 cm zu erreichen. Es wurden verschiedene Fehlerquellen untersucht, wie z. B. Datumsabweichungen, Neigungen (sowohl in Breiten- als auch in Längenrichtung), akkumulierte Neigungen, die auf der Entfernung von Referenzpegeln basieren, und höhenabhängige Fehler. Es wurden Uhren mit relativen Unsicherheiten von 10^{-18} und 10^{-17} angenommen, wobei intrinsische Unsicherheiten der Uhren, zeitliche Korrelationen, externe Faktoren wie Gezeiteneffekte, Ausbreitungsverzögerungen und das Vorhandensein von Ausreißern berücksichtigt wurden. Es wurden verschiedene Strategien zur Verteilung der Uhren getestet, um ein optimales Netzwerk für eine gute Schätzung dieser Fehler unter Berücksichtigung von Uhren an entfernten Nivellierpunkten, Referenzpegeln und Standorten mit größerer Höhe zu ermitteln. Ein Netzwerkdesign mit Haupt- und lokalen Uhren sowie reduzierten Verbindungen erscheint recht gut zu sein. Es kann eine Vereinheitlichungsgenauigkeit von 1 cm erreicht werden. Darüber hinaus konnten die vereinheitlichten Höhensysteme Europas und Brasiliens mit Bezug auf das globale Geoid mit einer Höhengenauigkeit von 3 cm realisiert werden. Die dritte Anwendung von Uhrennetzen konzentriert sich auf die Überwachung des globalen Meeresspiegels, der aufgrund des Klimawandels seit mehreren Jahrzehnten ansteigt. Bislang können Änderungen des absoluten Meeresspiegels (ASL) nur aus Messungen des relativen Meeresspiegels (RSL) genau bestimmt werden, indem vertikale Landbewegungen an Gezeitenmesspunkten geeignet berücksichtigt werden. Atomuhren an diesen Pegeln können absolute physikalische Höhenänderungen in Echtzeit liefern. Da der RSL durch regionale Gezeitendaten beeinflusst wird, müssen lokale Schwankungen berücksichtigt werden, um eine konsistente, globale ASL-Messung zu gewährleisten. Durch die Einbeziehung von Landbewegungen, die von Uhrenbeobachtungen abgeleitet werden, ist es möglich, ein einheitliches Referenzdatum festzulegen, das eine genaue, auf das Geoid basierende Bestimmung der globalen Meeresspiegelveränderungen ermöglicht. Diese Anwendungen zeigen, dass die relativistische Geodäsie mit Uhren die Geodäsie durch punktuelle und direkte Messungen des zeitvariablen Schwerepotenzials nahezu in Echtzeit revolutionieren kann.

Schlagwörter: Atomuhren, chronometrische Geodäsie, zeitvariables Schwerefeld, globales Höhensystem, absoluter Meeresspiegel

Contents

1 Introduction

1.1 Background & Motivation

Geodesy, based on advanced mathematical formulations, seeks to model and determine Earth's shape, gravity field, and rotation (Hofmann-Wellenhof and Moritz, 2006). The ticking rate of a clock is influenced by both gravitational potential and velocity, according to the theory of relativity, with both effects contributing to time dilation (Pützfeld and Lämmerzahl, 2019). These frequency changes, measurable with high-performance atomic clocks, provide a novel method to observe Earth's geodetic parameters (Müller et al., 2008; Denker et al., 2018; Müller et al., 2018).

Temporal gravity signals, arising from mass redistribution processes such as glacier melting, groundwater depletion, and tectonic activity, are crucial for understanding climate change and resource management (Tapley et al., 2019; Pail et al., 2015). They can also be observed with clocks in the future. High-performance clocks provide a unique advantage by directly measuring the total effective gravity potential change at a specific point over time, accounting for both mass redistribution and associated vertical land displacement on a deformable Earth (Schröder et al., 2021). In contrast, satellite gravimetry, such as GRACE, measures only the gravitational potential variations caused by mass anomalies under a rigid Earth assumption (Wahr, 1985). To determine the total effective potential variation at a point, satellite gravimetry data must be combined with GNSS-derived observations of vertical land motion at the location of interest. This integration introduces complexities and potential inaccuracies. Clocks bypass these challenges by offering direct, pointwise measurements of the total effective potential, making them an unparalleled tool for studying dynamic Earth processes (Vincent and Müller, 2023).

Classical geodetic methods such as terrestrial gravimetry, levelling, and satellite gravimetry, have advanced our understanding of the gravity field and physical heights. However, these methods are constrained by limitations due to their spatial and temporal resolution and inaccuracies from measurement techniques and modelling assumptions (Sánchez et al., 2021). Height systems referenced to the local mean sea level vary across regions and are not aligned with the global geoid, creating inconsistencies. The IAG has defined the concept of an International Height Reference System (IHRS), which standardizes vertical coordinates as geopotential numbers (Ihde et al., 2017). This system facilitates the unification of diverse local height systems that currently employ orthometric, dynamic, or normal heights (Jekeli, 2000). While GNSS provides ellipsoidal heights, the determination of geopotential numbers still requires combining gravity and levelling data. Clocks directly measure gravity potential values relative to a reference clock at a known datum point, making them a valuable tool for determining vertical datum parameters or errors in the local height systems and unifying them (Wu et al., 2018; Wu and Müller, 2022). Through clock-based observations, the realization of a globally consistent height system becomes achievable, ensuring accurate and consistent elevation data worldwide (Vincent et al., 2025).

Monitoring sea level changes is vital for understanding climate impacts, particularly in low-lying coastal regions (Lindsey, 2007). Currently, Absolute Sea Level (ASL) is measured either by satellite altimetry, which provides sea surface heights or by combining Relative Sea Level (RSL) from tide gauges with vertical land motion derived from GNSS (Peng et al., 2021). However, RSL is referenced to local benchmarks, such as GNSS points or tidal datums, which vary across locations and introduce inconsistencies. Clocks provide a solution by offering both relative sea level and vertical land motion, directly referenced to a common standard, thereby enabling globally consistent absolute sea level measurements (Vincent and Müller, 2024). By integrating clock observations into sea level monitoring networks, it becomes possible to achieve uniform and accurate ASL monitoring on a global scale, advancing our understanding of sea level dynamics.

Optical atomic clocks, with fractional uncertainties as low as 10^{-18}, corresponding to 0.1 m^2/s^2 in gravity potential or a 1 cm height change, can overcome the limitations of classical techniques (Bothwell et al., 2019; McGrew et al., 2018). These clocks offer real-time, pointwise measurements with better accuracy, paving the way for transformative advancements in geodesy (Grotti et al., 2024; Voigt et al., 2016). The applications of this technology are vast. From time-variable gravity signals to global height systems and absolute sea level monitoring, their integration into geodesy offers promising insights into Earth's dynamic processes, infrastructure development, and addresses critical challenges posed by climate change within a relativistic framework.

By exploring the potential of optical atomic clocks, the research aims to bridge fundamental physics with applied geodesy, laying the groundwork for a new era in Earth observation.

1.2 State of the Art

Chronometric geodesy, leveraging high-precision atomic clocks, is rapidly developing as a tool to measure geodetic parameters. Early numerical studies by Voigt et al. (2016) analyzed tidal temporal gravity signals relevant for clock comparisons, while Schröder et al. (2021) extended simulations to non-tidal signals across Europe. Additionally, optical clocks have been proposed as a means to continuously monitor geoid changes with high temporal resolution, offering potential applications in earthquake prediction, volcanic activity monitoring, and detecting surface deformation from activities like hydraulic fracturing (Bondarescu et al., 2015). Recent work has expanded these analyses globally, incorporating a variety of non-tidal mass redistribution signals over longer time series, highlighting the potential of clock networks to complement satellite gravimetry in monitoring time-variable gravity (Vincent and Müller, 2023).

The International Height Reference System (IHRS) (Sánchez et al., 2023) framework, promoted by the International Association of Geodesy, aims to unify vertical datums globally. Implementation currently relies on combined satellite gravimetry (e.g., GRACE, GOCE), terrestrial gravity measurements, and GNSS positioning (Gerlach and Rummel, 2013; Sideris et al., 2014). The study by Lion et al. (2017) focuses on regional high-resolution geopotential determination using synthetic clock and gravity data. A major milestone was achieved by the ICON Collaboration, which demonstrated international comparisons of transportable optical clocks without relying on high-performance frequency links or precise geopotential knowledge, enabling centimeter-level height offset determination and validating clock transportability for global geodetic applications (Clock et al., 2024). Two strategies for clock-based IHRS realization have been proposed: (i) establishing a hierarchical global network of atomic clocks, and (ii) using clock networks to detect and correct systematic errors in existing local height systems (Wu et al., 2018; Wu and Müller, 2022). Simulations show that optical clock networks connected by fibers can transfer height information between datums at centimeter-level accuracy, aiding height system unification (Hoang et al., 2023). Shen et al. (2023b) proposed a satellite frequency signal transmission (SFST) method to unify distant vertical height systems using clock comparisons, achieving centimeter-level accuracy in simulations between China and the US. Recent advancements include optimized clock network designs that reduce link requirements and incorporate realistic error sources such as tidal influences and time-correlated clock noise, demonstrated through test cases of European and Brazilian height systems (Vincent et al., 2025).

In sea level monitoring, satellite altimetry missions (e.g., JASON, Sentinel-6) provide global sea surface height data referenced to geoid models, while GNSS stations support land motion measurements combined with tide gauges for relative sea level assessment (Fu and Cazenave, 2000; Peng et al., 2021). Integrating these datasets poses challenges related to reference frame consistency and geoid model accuracy (Featherstone, 2001). Clock-based geodesy offers a novel approach by replacing GNSS benchmarks with clocks, enabling consistent, real-time, and pointwise measurements of both relative sea level and vertical land motion directly tied to the geoid (Vincent and Müller, 2024).

Technological progress in optical lattice clocks and ion clocks has pushed frequency uncertainties to the 10^{-18} level, with institutions such as NIST, RIKEN, and PTB leading these advances (Aeppli et al., 2024; Rojo et al., 2024; Takamoto and Katori, 2024; Grotti et al., 2024; Leibrandt et al., 2024). Systematic uncertainties as low as 10^{-19} have been achieved with fibre links under realistic field conditions (Lisdat et al., 2016; Koke et al., 2019). Wu et al. (2024) used hydrogen clocks and satellite time transfer to estimate geopotential differences between remote sites, with deviations aligning with clock stability limits. Space-based clock missions, including ESA's ACES, aim to extend these capabilities for global gravitational field mapping and relativistic geodesy (Cacciapuoti and Salomon, 2011; Cacciapuoti et al., 2024).

1.3 Overview

This research explores the potential of terrestrial clock networks in geodesy by addressing three main applications:

1. Detection of Time-Variable Gravity Signals: Time-variable gravity signals, driven by continuous mass redistributions in the Earth system, are critical for understanding climate change, resource management, and sustainable development. How high-performance optical atomic clocks can observe such signals by simulating realistic observation scenarios is investigated. The focus is on non-tidal signals, including terrestrial water storage variations, glacial isostatic adjustment, present-day ice mass loss, and seismic activities. By leveraging the ability of clocks to provide direct measurements of gravity potential variations on a deformable Earth, the research question is:

How sensitive are clock networks for detecting different time-variable gravity signals under realistic configurations?

2. Realization of an International Height Reference System (IHRS): A unified global height system referenced to the geoid is essential for consistent height data, where current systems rely on the local mean sea level and classical levelling, which accumulate errors over distance. Satellite and ground-based gravimetry methods, while useful, are limited by spatial resolution and model assumptions. Chronometric levelling is used in this study to unify existing local/regional height systems. By simulating clock observations and considering realistic error sources, the aim is to answer:

How can local height systems be unified into a global IHRS using clock observations under realistic conditions?

What are the optimal configurations and error tolerances for achieving the relevant high accuracy in global height system unification?

3. Globally Consistent Absolute Sea Level Monitoring: Current methods for monitoring absolute sea level changes rely on relative sea level measurements combined with vertical land motion estimates at GNSS benchmarks, which are limited by local tidal datum inconsistencies and ellipsoidal reference. The feasibility of using clock networks at tide gauge locations to directly monitor ASL changes in a physical height frame is explored in this study. By simulating clock observations as vertical land motion, the addressed research question is:

How well can clock networks provide consistent, geoid-related ASL measurements on a global scale?

Through dedicated simulations of realistic observation scenarios, the thesis aims to establish a framework for using high-performance atomic clocks for various geodetic applications.

1.4 Outline

The major goal of the research is to study various geodetic applications of clock networks through simulations. The first chapter introduces the general background and motivation followed by an overview of the main research objectives. The second chapter 2 provides the theoretical background, beginning with relativistic geodesy, based on Einstein's general relativity theory, gravitational time dilation, and redshift. The principle benefits of high-performance atomic clocks for geodetic applications are introduced. Further, mass redistribution in the Earth System, exploring time-variable gravity signals, including surface deformation, tidal, and non-tidal effects are discussed with how clocks can be used as geodetic sensors for dynamic Earth monitoring. The next section addresses the global height system, covering geopotential numbers, physical heights, and height system unification techniques focusing on chronometric levelling with detailing on biases in local heights and uncertainties of clock observations. The clock-based adjustment procedure is further discussed. The chapter concludes with global sea level monitoring, distinguishing between relative and absolute sea levels and describing how clocks can measure land motion. Chapters 3, 4, and 5 are dedicated to these three major research fields for possible applications of clock networks in Geodesy. Chapter 3 focuses on how clock networks can monitor temporal gravity changes. It addressed the impact of centrifugal potential variations. The role of reference clocks in time-series analysis is discussed. Simulation strategies are detailed, followed by various case studies: Himalayas (hydrological signals and monsoon dynamics), Amazon (seasonal hydrological patterns), Greenland (ice mass loss), Fennoscandia (GIA signals), and Japan (Tōhoku earthquake with co-seismic and post-seismic processes). Each case demonstrates how clock observations can detect specific gravity signals. Chapter 4 explores clock-based height system unification. It begins with the impact of tidal effects on clock observations. Later, details height system unification, presenting case studies in Europe (linked to NAP) and Brazil (linked to Imbituba). In Europe, complex error parameters are estimated with a discussion on optimal clock network configuration and unification using different frequency standards. In Brazil, modified links, robust parameter estimation, and time correlation effects are included. The chapter concludes by linking the unified height system to the global geoid, emphasizing the need for consistency in the global framework. Chapter 5 is dedicated to the potential of clock networks for monitoring absolute sea level changes. The methodology is explained, including the simulation of clock observations and derivation of absolute sea level changes. Land motion monitoring using clocks is discussed, with simulations of tidal and non-tidal signals. The chapter concludes with an assessment of geoid-based absolute sea level changes, particularly along the European coast, highlighting the advantages of using clock networks for coastal monitoring. Chapter 6 summarizes the main research results, discussing the benefits and limitations of clock networks as geodetic tools. It highlights open questions and proposes directions for future investigations to advance the field.

2 Fundamentals

2.1 Relativistic Geodesy/ Chronometric Geodesy

Relativistic geodesy with clocks or chronometric geodesy, represents a novel and promising approach that harnesses the principles of Einstein's theory of relativity to enhance our understanding of Earth's gravity field and its applications in geodesy. The foundation of this concept lies in the idea that the ticking rates of precise atomic clocks are affected by the gravitational potential at the location of the clock (Pützfeld and Lämmerzahl, 2019). This stems directly from Einstein's general theory of relativity, which predicts that clocks run slower in stronger gravitational fields—a phenomenon known as gravitational time dilation (Dirac, 1996; Schmidt, 2000). Using highly accurate clocks as a new tool in geodesy opens up a new dimension of measurements, where time becomes a geodetic observable. One can determine differences in the gravitational potential by comparing the ticking rates of clocks positioned at different locations (Bjerhammar, 1985). This capability allows for the determination of height differences and gravitational potential variations that are related to mass redistributions in the Earth.

The idea of using time measurements in geodetic applications was first proposed by Bjerhammer (Bjerhammar, 1986). In his seminal work, Bjerhammer explored the potential of using precise clock measurements to enhance traditional geodetic methods, which rely on spatial measurements. He suggested that by utilizing clocks with extreme precision, one could directly measure the gravitational potential differences across the Earth's surface, offering a new and potentially more accurate and consistent way to conduct geodetic surveys. Bjerhammer's pioneering concept laid the groundwork for what is now known as chronometric geodesy, which has since then gained attraction as an innovative approach for future geodetic applications (Denker et al., 2018; Müller et al., 2018; Delva et al., 2019).

As technology advances and atomic clocks become increasingly accurate, the practical implementation of relativistic geodesy is becoming more feasible. The transformation of clock rates into geodetic information can revolutionize the field, providing new tools for monitoring sea-level changes, understanding geodynamic processes, and improving positioning systems like GNSS (Global Navigation Satellite Systems) (Schröder et al., 2021; Vincent and Müller, 2024; Wu et al., 2018). Chronometric geodesy, therefore, holds significant promise for enhancing our understanding of the Earth's shape, gravity field, and dynamic processes, potentially leading to more accurate and efficient geodetic measurements in the future (McGrew et al., 2018; Wu and Müller, 2022; Grotti et al., 2024).

2.1.1 Einstein's Relativity Theory and Gravitational Redshift

Introduction to General Relativity

General Relativity Theory (GRT) is a comprehensive theory of the gravitational field, developed within the framework of the theory of relativity (Einstein, 1915). According to GRT, matter and energy are responsible for generating the gravitational field, which in turn affects the motion of matter (Lämmerzahl, 2009; Wald, 2010). This interaction fundamentally differs from the classical Newtonian view, where gravity is seen as a force acting at a distance. In GRT, gravity is not a force but a manifestation of the curvature of space-time caused by the presence of mass and energy (Misner et al., 2017).

The mathematical relation of this curvature is given by the metric tensor ($g_{\mu\nu}$), a fundamental object in general relativity that defines the geometry of space-time (Hawking and Ellis, 1975). The metric tensor $g_{\mu\nu}$ is used to determine the distance between nearby points in space-time and governs the motion of objects under the influence of gravity. The Einstein field equations, which are the core of GRT, relate the metric tensor to the stress-energy tensor $T_{\mu\nu}$, representing the distribution of matter and energy (Hartle, 2021; Ryder, 2020). In essence, the gravitational field is defined as a change in the metric of space-time as determined by $g_{\mu\nu}$. When analyzing the time interval or line element for a time-like world-line in the context of general relativity, the gravitational field plays a central role (Philipp et al., 2017).

For a time-like world-line, which represents the path traced by an object with mass moving through space-time, the interval ds^2 corresponds to the proper time $d\tau$ experienced by the object. This proper time is given by

$$d\tau^2 = -\frac{ds^2}{c^2} \tag{2.1}$$

where ds^2 is the space-time interval when using Einstein's summation convention[1],

$$ds^2 = g_{\mu\nu}(x^\gamma)dx^\mu dx^\nu. \tag{2.2}$$

$x^\gamma = (x^0,x^1,x^2,x^3)$ represents the space-time coordinates with $x^0 = ct$ where t is the coordinate time and c is the velocity of light. Here, x^1,x^2,x^3 denote the spatial coordinates, and dx^μ and dx^ν are the differentials of the space-time coordinates. The proper time $d\tau$ represents the time measured by a clock moving along the time-like world-line. It is the time interval experienced by the observer or object in its own reference frame. Hence, the interval ds^2 quantifies the separation between events in space-time, while for a time-like world line, it specifically measures the proper time, reflecting the time taken according to the observer's own clock

[1]Einstein's summation convention implies that when an index appears twice in a single term, once as a subscript and once as a superscript, summation over that index is assumed. For example, $A^\mu B_\mu = \sum_\mu A^\mu B_\mu$.

(Lämmerzahl and Dittus, 2007).

Time Dilation and Gravitational Redshift

Time dilation refers to the phenomenon where the elapsed time $d\tau$ between two events is affected by the presence of a gravitational field or relative velocity. Clocks run slower in the presence of a stronger gravitational field (Pützfeld and Lämmerzahl, 2019). The time dilation effect is quantified by comparing the proper time experienced by an observer in a gravitational field to that experienced by an observer far from any gravitational source. Gravitational redshift is a consequence of time dilation (Wilhelm and Dwivedi, 2014). As light or any electromagnetic signal comes closer to a gravitational field, its frequency decreases, leading to a redshift.

The relation between proper and coordinate time is obtained by

$$\left(\frac{d\tau}{dt}\right)^2 = -\frac{1}{c^2}\left(g_{00}\left(\frac{dx^0}{dt}\right)^2 + 2g_{0i}\frac{dx^0}{dt}\frac{dx^i}{dt} + g_{ij}\frac{dx^i}{dt}\frac{dx^j}{dt}\right) \tag{2.3}$$

where $\frac{d\tau}{dt}$ represents the time dilation factor (Pützfeld and Lämmerzahl, 2019; Lämmerzahl and Dittus, 2007). By defining $v^i(t)$ as the coordinate velocity along $x^i(t)$, the equation can be reduced into

$$\left(\frac{d\tau}{dt}\right)^2 = -g_{00} - g_{0i}\frac{2v^i}{c} - g_{ij}\frac{v^i v^j}{c^2}. \tag{2.4}$$

The post-Newtonian form of the metric tensor which relates $g_{\mu\nu}$ to gravitatnal potentials of time and spatial coordinates, V and V^i as (Müller et al., 2018)

$$g_{00} = -1 + \frac{2V}{c^2} - \frac{2V^2}{c^4} + O(c^{-6}) \tag{2.5}$$

$$g_{0i} = -\frac{4V^i}{c^3} + O(c^{-5}) \tag{2.6}$$

$$g_{ij} = \delta_{ij}\left[1 + \frac{2V}{c^2}\right] + O(c^{-4}). \tag{2.7}$$

The gravitational potential observed in different reference frames affects the time dilation experienced by clocks (Damour et al., 1991). The observed time dilation and redshift will differ based on these frame-dependent potentials. There exist different metrics. That of the Geocentric Celestial Reference System (GCRS) centred in the non-rotating Earth can be given in a simplified way as

$$g_{\mu\nu}^{GCRS} = \begin{bmatrix} -1 + \frac{2V}{c^2} & 0 & 0 & 0 \\ 0 & 1 & 0 & 0 \\ 0 & 0 & 1 & 0 \\ 0 & 0 & 0 & 1 \end{bmatrix} + O(c^{-4}). \tag{2.8}$$

As the Barycentric Celestial Reference System (BCRS) has its origin in the solar system's centre of mass (Soffel, 2013), the metric is computed with a different potential w as given by Müller et al. (2018). For terrestrial clocks, the GCRS is crucial as it provides a local frame of reference that accounts for Earth's gravity (Denker et al., 2018). The BCRS, on the other hand, is important for astronomical observations and for understanding the broader gravitational context in which these measurements are made. The choice of the reference frame affects the interpretation of time dilation and redshift measurements (Kopejkin, 1988).

The metric tensor $g_{\mu\nu}$ is generated based on the gravitational fields and relative motions in its respective reference frame (Kopejkin, 1991). The GCRS metric tensor accounts for Earth's gravitational influence and rotation, while the BCRS metric tensor incorporates the gravitational effects of the solar system as a whole (Kopeikin et al., 2011). These metric tensors are derived from the Einstein field equations and provide the necessary components for analyzing time dilation and redshift. The post-Newtonian approximation refines the Newtonian gravitational potential by including relativistic corrections (Jekeli, 2007). In a post-Newtonian approximation, i.e., including terms up to $\frac{1}{c^2}$ with c being the speed of light, when inserting the GCRS metric terms (equations (2.5) - (2.7)) into equation (2.3), the fundamental equation reads

$$\left(\frac{d\tau}{dt}\right) = 1 - \frac{W}{c^2} + O(c^{-4}) \tag{2.9}$$

with the gravity potential $W = V + \frac{v^2}{2}$, where V is the Newtonian potential and v is the coordinate velocity (Denker et al., 2018).

2.1.2 High-performance Atomic Clocks and Geodetic Applications

As the ticking rate or frequency of atomic clocks varies under the influence of gravity fields, the relative gravity potential difference or the corresponding physical height difference between any two Earth's surface sites can be obtained by comparing the respective clock observations. For clocks positioned at different gravity potentials W_A and W_B, the g_{00} component varies, resulting in different proper times τ_A and τ_B (Müller et al., 2018). However, the coordinate time t,

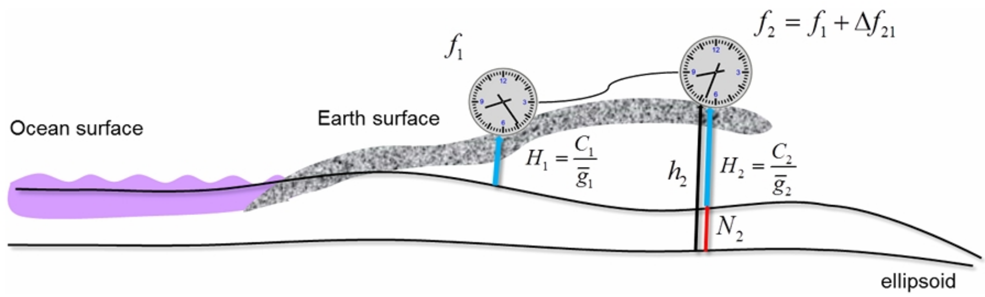

Figure 2.1: Relativistic geodesy with atomic clocks (Müller et al., 2018)

which is the time measured by an observer at infinity or in a common reference frame, remains the same for both clocks if they are synchronized and their measurements are compared simultaneously. This consistency in coordinate time allows us to express the ratio of proper times from equation (2.9) as,

$$\frac{d\tau_B}{d\tau_A} = \frac{f_A}{f_B} = \frac{1 - W_B/c^2}{1 - W_A/c^2}. \tag{2.10}$$

Given that the fractional frequency f of a clock is inversely proportional to its proper time (i.e., $f \propto \frac{1}{\tau}$), the fractional frequency difference between the two clocks can be expressed as

$$\frac{\Delta f}{f} = \frac{f_B - f_A}{f_B} = \frac{W_B - W_A}{c^2} = \frac{C_A - C_B}{c^2} = \frac{\overline{g_A} H_A - \overline{g_B} H_B}{c^2} \tag{2.11}$$

where, $C \approx \overline{g} H$ represents the geopotential number with $\overline{g}$ denoting the mean gravity along the plumb line and H representing the orthometric height (Torge et al., 2023). This equation reveals that the fractional frequency difference between the two clocks is directly proportional to the difference in their gravity potentials or the corresponding height differences between the clocks, making it a powerful tool for geodetic applications.

An atomic frequency standard is operated as a clock by counting the number of cycles of unperturbed transitions between two long-lived energy levels from a well-defined starting time (Le Targat et al., 2013). Clock performances are often characterized by their fractional uncertainty (accuracy) and instabilities (Mehlstäubler et al., 2018; Sharma et al., 2020). The statistical uncertainty of the output frequency of the frequency standard is defined as instability while the systematic uncertainty of the deviation of the frequency standard from the unperturbed atomic reference frequency is termed as accuracy. The fractional frequency uncertainty determines the sensitivity of the shift detection. From equation (2.11), one can derive that a gravity potential variation of 0.1 $\mathrm{m}^2/\mathrm{s}^2$ or a physical height difference of 1 cm produces a fractional frequency change of 10^{-18} (Bothwell et al., 2022). The ability to measure such small fractional frequency differences with high precision is made possible by modern high-performance optical clocks, which have reached accuracies that allow for the detection of potential differences corresponding to height changes as small as a few centimetres (McGrew et al., 2018; Takamoto et al., 2022). This capability forms the basis for many geodetic applications, including precise height measurements and the monitoring of Earth's gravity field (Voigt et al., 2016; Wu and Müller, 2022).

Atomic clocks have undergone significant evolution in the past 60 years. The first atomic clocks, based on microwave transitions in Caesium atoms, were developed in the mid 20^{th} century (Bauch, 2003). These clocks provided a major leap in timekeeping accuracy, setting the standard for the International System of Units (SI) seconds (Beehler et al., 1965). The development of Caesium fountain clocks in the late 20^{th} century marked another milestone, allowing for even higher precision

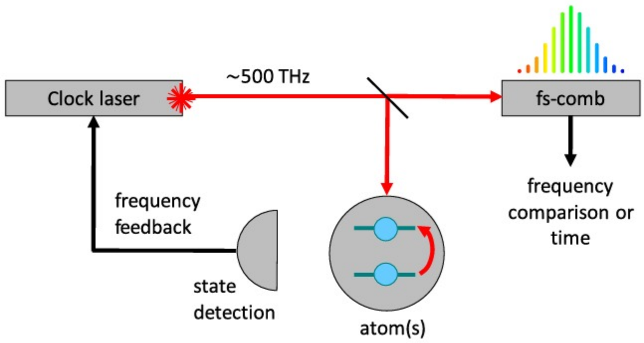

Figure 2.2: Schematic of an optical frequency standard (Mehlstäubler et al., 2018)

in measuring the SI second (Schroder et al., 2002). However, the most significant advancements have come with the development of optical clocks, which operate at much higher frequencies than microwave-based clocks. The higher frequency of optical transitions allows for higher precision in time measurement, leading to the current generation of optical lattice and ion clocks. Recent years have seen ongoing improvements in clock stability and accuracy, driven by advances in laser technology, cooling and trapping techniques, and quantum state control (Riehle, 2015; Mehlstäubler et al., 2018). As a result, today's high-performance atomic clocks are capable of measuring time with such precision that they can detect minute changes in the gravity potential or small height differences, making them novel tools for geodetic applications (Takamoto and Katori, 2024; Grotti et al., 2024; Collaboration et al., 2021).

Optical lattice clocks trap atoms in a lattice formed by standing waves of light. These clocks achieve remarkable stability and accuracy, with fractional frequency uncertainties reaching the 10^{-18} level. Recent advancements in this field have been driven by leading research institutions such as the National Institute of Standards and Technology (NIST), the RIKEN Center for Advanced Photonics, and the Physikalisch-Technische Bundesanstalt (PTB) in Germany. These teams have consistently improved the clock performance, pushing the boundaries of precision in timekeeping. Ion clocks, which use single ions trapped in electromagnetic fields as their timekeeping element, have achieved similarly high precision, with some systems also approaching the 10^{-18} uncertainty level (Rojo et al., 2024; Takamoto and Katori, 2024; Grotti et al., 2024). PTB, along with other institutions like the University of Colorado Boulder, has been at the forefront of advancing ion clock technology (Leibrandt et al., 2024; Steinel et al., 2023; Tofful, 2023). There is also growing interest in deploying high-performance optical clocks in space, where they could be used for precise measurements of Earth's gravitational field on a global scale. Projects such as the European Space Agency's ACES (Atomic Clock Ensemble in Space) mission aim to demonstrate the potential of these clocks for space-based geodesy (Cacciapuoti and Salomon, 2011).

2.2 Mass Redistribution in Earth System

The Earth is a complex and dynamic system composed of several sub-systems that constantly interact with each other, which are typically categorized into five major spheres: atmosphere, hydrosphere, lithosphere, cryosphere and biosphere (Jacobson et al., 2000). Weather and climate dynamics, along with the exchange of energy and matter between the Earth's spheres, are significantly influenced by the atmosphere, the layer of gases surrounding the planet. The hydrosphere encompasses all liquid water bodies on Earth, including oceans, rivers, lakes, and groundwater, hence, it provides major contributions to mass redistribution through processes like the water cycle, ocean currents, and glacial melting (Kusche et al., 2012; Huggett, 2024). The solid outer layer of the Earth, including the crust and the upper mantle, is called the lithosphere and is subject to tectonic activities, erosion, and other geological processes that contribute to mass redistribution. The cryosphere includes all frozen water on Earth, such as glaciers, ice caps, and permafrost. Significant mass redistribution occurs in the cryosphere due to melting and freezing processes, which are particularly influenced by climate change (Tapley et al., 2019). While there is no direct contribution to mass redistribution by the biosphere, which consists of all living organisms on Earth, it plays a significant role in carbon and nutrient cycles.

Continuous mass redistribution within the Earth system is driven by a variety of processes, both internal and external (Petit et al., 2010; Voigt et al., 2016; Vincent and Müller, 2023). Significant changes occur due to non-tidal factors such as precipitation, groundwater changes, ice mass loss influenced by climate change, glacial isostatic adjustment, etc. Additionally, tidal effects due to external effects, caused by the gravitational pull of the Moon and the Sun, temporal changes in the Earth's rotation, like polar motion, changing rotational speed, atmospheric tides, etc. also play a crucial role in redistributing mass. Together, these processes contribute to the dynamic nature of the Earth's gravity field, making it essential to understand their impacts on various geodetic applications (Pail et al., 2015).

The Earth's gravity potential is a combination of the gravitational potential, which arises from the attraction of mass distribution of the Earth, and the centrifugal potential, which results from the Earth's rotation. The gravitational potential varies across the Earth due to its irregular shape and the non-uniform distribution of mass in it. The centrifugal potential, on the other hand, varies with latitude but also due to polar motion and Earth rotation. Together, these potentials define the Earth's gravity field (Telford et al., 1990; Torge et al., 2023). To accurately describe and utilize the Earth's gravity potential, different reference surfaces are defined. The ellipsoid is a mathematically simple surface that approximates the Earth's shape, accounting for the flattening at the poles due to rotation. It is primarily used for horizontal positioning, such as latitude and longitude coordinates (Leick, 2015). The realization of the physical shape is provided by the geoid, a more complex surface that closely follows the mean sea level and represents an equipotential surface of the Earth's gravity field. The geoid is critical for measuring physical heights and understanding variations in the grav-

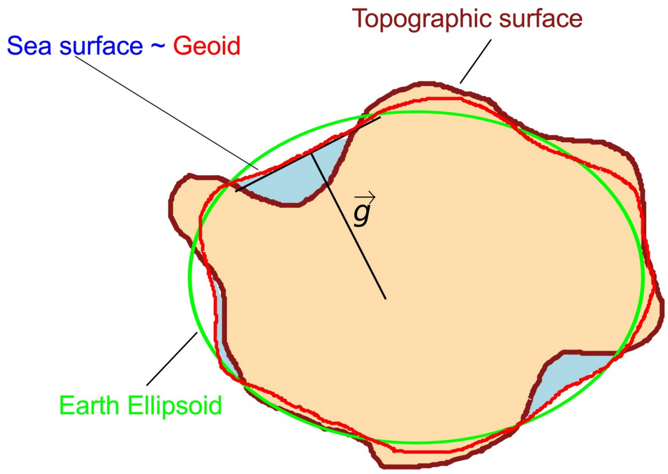

Figure 2.3: Ellipsoid vs. geoid (Favier, 2016)

ity potential (Torge et al., 2023). These reference surfaces are fundamental in geodesy, as they allow for precise positioning, mapping, and interpretation of the Earth's gravity variations.

To represent the Earth's gravitational potential with higher resolution in the spatial domain, it can be expanded into a series using surface spherical harmonics (Hofmann-Wellenhof and Moritz, 2006). This mathematical expansion allows the potential to be expressed as a sum of terms that account for variations at different spatial scales (Burkard, 1977). The spherical harmonic expansion is a powerful tool in geodesy, enabling the modelling of the Earth's gravity field at various resolutions and facilitating the determination of global geopotential models (Barthelmes, 2014). The coefficients of this expansion, derived from satellite gravimetry, gravimetric surveys, and further geodetic measurements, are essential for accurately characterizing the Earth's gravitational field.

2.2.1 Time-variable Gravity Signals

The gravity potential of the Earth consists of both the time-independent static $W(t_0)^{static}$ and the time-dependent temporal $W(t-t_0)^{temp}$ components (Denker et al., 2018)

$$W(t) = W(t_0)^{static} + W(t-t_0)^{temp}. \tag{2.12}$$

The static component includes the gravitational potential and centrifugal potential that remains constant over time and gives the physical Earth's shape, the geoid. The temporal gravity potential accounts for variations over time due to dynamic processes and external effects. It can be divided into tidal and non-tidal components.

Mass Anomalies and Surface Deformation

Mass anomalies reflect the inhomogeneous distribution of mass in the Earth system. They can change due to various temporal geophysical effects. These variations in mass distribution lead to changes in the gravitational field, which can be detected by satellite gravimetry (Tapley et al., 2019). Surface deformation occurs when the Earth's crust bends in response to these mass changes due to elasticity, altering the shape and further influencing the gravitational field (Farrell, 1972). The effective potential at a given point on the Earth's surface is the combined effect of mass anomalies and the accompanied surface deformation, playing a critical role in geodesy and contributing to our understanding of dynamic processes in the Earth (**?**).

In the simplest case, when considering the gravitational potential change due to mass anomalies, we assume a fixed Earth model where the Earth's surface does not deform in response to mass redistribution (Wahr et al., 1998). This approximation is often used as a starting point for understanding more complex interactions (Ramillien et al., 2008; Rodell and Reager, 2023; Eicker et al., 2024). The gravitational potential at a point $\mathbf{r}$ on or above the Earth's surface due to a mass distribution can be expressed using a spherical harmonic expansion (Burkard, 1977). This method decomposes the potential into a series of spherical harmonics, each characterized by a degree n and order m, which describe the spatial variations of the potential. The change in gravitational potential $\delta V(\lambda,\theta,\mathbf{r})$ due to mass anomalies, under the fixed Earth assumption, can be written as

$$\delta V(\lambda,\theta,r) = \frac{GM}{R} \sum_{n=0}^{\infty} \left(\frac{R}{r}\right)^{n+1} \sum_{m=0}^{n} \overline{P}_n^m(\cos\theta)(\delta\overline{C}_{nm}\cos m\lambda + \delta\overline{S}_{nm}\sin m\lambda), \tag{2.13}$$

where $\delta\overline{C_{nm}}$ and $\delta\overline{S_{nm}}$ are the fully normalized Stokes coefficients representing the mass anomalies, and $\overline{P}_n^m(\cos\theta)$ are the normalized associated Legendre functions (Hofmann-Wellenhof and Moritz, 2006). This expansion provides a global representation of the gravitational potential change and is particularly useful for analyzing data from satellite missions like GRACE and GRACE-FO, which observe the Earth's gravity field with high precision (Chen et al., 2022).

Elastic loading and Love numbers: While the fixed Earth model provides a useful approximation, it is essential to account for the Earth's elastic response to surface loading. When a mass is redistributed on the Earth's surface, the Earth's crust deforms elastically. This deformation changes the Earth's shape, affecting the gravitational potential in a more complex manner (Farrell, 1972). To quantify this deformation, one introduces Love numbers, denoted as h_n, k_n, and l_n, which describe the Earth's elastic response to surface loads in terms of vertical displacement, potential change, and horizontal displacement, respectively (Love, 1909). The gravitational potential change considering elastic loading can be modified from the fixed Earth case by incorporating the Love numbers h_n and

k_n (Hofmann-Wellenhof and Moritz, 2006):

$$\delta U(\lambda,\theta,r) = \frac{GM}{R} \sum_{n=0}^{\infty} (1 + k_n - h_n) \left(\frac{R}{r}\right)^{n+1} \sum_{m=0}^{n} \overline{P}_n^m(\cos\theta) \\ (\delta\overline{C}_{nm} \cos m\lambda + \delta\overline{S}_{nm} \sin m\lambda). \tag{2.14}$$

The term $1 + k_n - h_n$ represents the combined effects of gravitational potential changes in the mass anomalies and the additional potential resulting from the Earth's elastic deformation (Longman, 1963). The term k_n captures the self-gravitating effect of loading or unloading potentials, which describes how the redistribution of mass directly affects the gravitational field. In contrast, h_n reflects the surface deformation, an indirect effect that arises as the Earth's crust adjusts to the changes in mass distribution. Thus, k_n represents the direct gravitational changes, while h_n accounts for the Earth's elastic response, together providing a comprehensive picture of the gravitational potential changes due to mass redistribution and surface deformation (Wahr et al., 1998; Schröder et al., 2021).

Viscoelastic formulation: The Earth's response to surface loads is not purely elastic but also exhibits some viscoelastic behaviour, particularly over long time scales (Dorman and Lewis, 1970). Viscoelasticity refers to the combination of elastic and viscous properties in the Earth's materials (Peltier, 1974). Over short time scales, the Earth behaves elastically, but over longer periods, it shows viscous flow, leading to time-dependent deformation. This behaviour is especially relevant in processes like a post-glacial rebound, where the Earth slowly adjusts to the removal of ice masses over thousands of years and also for present-day ice-mass, loss e.g., in Greenland (Michel and Boy, 2022). To model this time-dependent deformation, one uses time-dependent Love numbers, $k_n(t)$ and $h_n(t)$ which evolve as the Earth's structure relaxes over time as

$$h_n(t) = h_n^v(t) + h_n^e\delta(t), \tag{2.15}$$

$$k_n(t) = k_n^v(t) + k_n^e\delta(t). \tag{2.16}$$

$\delta(t)$ indicates the elastic response which occurs instantaneously at time t=0, the moment the load is applied (Peltier, 1974). This formulation accounts for the gradual relaxation of the Earth's structure, providing a more accurate representation of the long-term evolution of the Earth's gravity field in response to surface loading. Green's functions, when used in conjunction with these time-dependent Love numbers, provide a powerful mathematical tool used to relate surface mass loads to the resulting deformation and gravitational potential changes (Farrell, 1972; Longman, 1963). They provide the displacement components and potential perturbations caused by point surface mass loads and depend on the angular distance between the points of load and the observation point on the Earth's surface.

Tidal Effects

Tidal effects on the Earth's gravitational potential arise from the gravitational interaction with celestial bodies, primarily the Moon and the Sun. Solid Earth Tides (SET) are caused by the deformation of the Earth's crust, resulting in periodic changes of the gravity potential (Wahr, 1995). This effect is characterized by variations in the Earth's shape and mass distribution. On a deformable Earth surface, the effective solid Earth tidal potential at a specific point is given as

$$
\begin{aligned}
\delta U^{SET}(t) = &\sum_{n=0}^{\infty} (1 + k_n - h_n) \left(\frac{R}{r}\right)^{n+1} \sum_{m=0}^{n} \overline{P}_n^m(\cos\theta) \\
&\sum_{i=1}^{\text{ß}_{max}} (C_{nm}(t)\cos[\alpha_i(t)] + S_{nm}(t)\sin[\alpha_i(t)])
\end{aligned}
\tag{2.17}
$$

where $C_{nm}(t)$ and $S_{nm}(t)$ are the time-dependent coefficients for the cosine and sine components of the tidal potential (Petit et al., 2010). These coefficients vary with time due to the relative positions of Earth, Moon, and Sun. $\alpha_i(t)$ represents the time-dependent arguments, which are the phase angles associated with different tidal waves (i.e., different periodic components of the tidal potential). The index i runs over all the significant tidal frequencies, with i_{max} representing the total number of tidal components considered.

Ocean load tides (OTL) refer to the gravitational potential changes caused by the redistribution of ocean mass due to tidal forces, which alters the local gravitational field as the ocean water is displaced (Jentzsch, 2005). The Green's function ($G(\xi)$) is formed by a weighted sum of the load Love numbers (h'_n, k'_n) and Legendre polynomials $P_n(\cos\xi)$, which depicts the dependence on the spherical distance ξ between the computation point and the surface mass load. The tidal potential at a surface point on Earth is given as

$$
\delta U^{OTL}(t) = \int_{\text{Earth's surface}} G(\xi)\,\sigma(\theta', \varphi', t)\,dA' \tag{2.18}
$$

$$
G(\xi) = \sum_{n=0}^{\infty} (1 + k'_n - h'_n)\,P_n(\cos\xi) \tag{2.19}
$$

where $\sigma(\theta', \varphi', t)$ is the surface mass density distribution of the ocean load at time t and dA' represents the differential surface area element over the Earth's surface (Agnew, 2012).

Pole tides (POL) result from changes in the Earth's gravitational potential due to shifts in the position of the rotational axis, affecting mass distribution at the poles (Wahr, 1985):

$$
\delta U^{POL}(t) = -\,(1 + k'_2 - h'_2)\,\omega^2 r^2 \sin\theta\cos\theta\Delta\theta \tag{2.20}
$$

where ω represents the mean angular velocity (Petit et al., 2010). The deviation in the co-latitude due to pole tide effects is derived from the instantaneous rotation pole (x_p,y_p) with respect to the mean rotation pole ($\overline{x_p}$,$\overline{y_p}$) as, $\Delta\theta(t) = (x_p - \overline{x_p})\cos\lambda - (y_p - \overline{y_p})\sin\lambda$.

Length-of-Day tides (LOD) are linked to variations in the Earth's rotation rate, which affects the centrifugal potential and consequently the gravitational field, obtained by differentiating the centrifugal potential with respect to ω (McCarthy and Luzum, 1993).

In addition, atmospheric tides are caused by the gravitational pull of the Moon and the Sun on the Earth's atmosphere, leading to periodic variations in atmospheric pressure and density (Lindzen and Chapman, 1969). These atmospheric tides contribute to fluctuations in the gravitational potential by altering the distribution of the atmospheric mass. Collectively, these tidal effects provide valuable information about the dynamic processes affecting the Earth's gravitational field (Voigt et al., 2016).

Non-tidal Effects

Non-tidal mass redistributions in the Earth's four primary spheres, atmosphere, hydrosphere, cryosphere, and lithosphere, result in significant variations in the gravitational potential. Atmospheric variations are caused by changes in atmospheric pressure and density, which affect the gravitational field. Fluctuations due to weather systems, seasonal shifts, and pressure changes result in periodic or non-periodic alterations in the distribution of atmospheric mass, affecting both local and global gravity measurements (van Dam and Wahr, 1987). Oceanic variations involve changes in ocean mass distribution resulting from seasonal and climatic factors, such as those induced by El Niño and La Niña events (Collins, 2005). These variations lead to alterations in the gravitational potential as ocean mass is redistributed across different regions (van Dam et al., 1997). Cryospheric variations include the effects of ice loss from glaciers and ice sheets. As the ice melts and redistributes into the oceans, the mass shift impacts the gravitational field, especially in polar and high-latitude areas (Velicogna, 2009). Terrestrial Water Storage (TWS) reflects the redistribution of water in lakes, rivers, and reservoirs, which causes changes in the gravitational field due to variations in water mass (Wahr et al., 1998; Tregoning et al., 2009). Additionally, Glacial Isostatic Adjustment (GIA) describes the Earth's crust's gradual response to changes in ice mass distribution, such as the rebound effect following the last ice age and ongoing adjustments related to current ice mass loss (Ekman, 1996; Olsson et al., 2019). These non-tidal mass redistributions across the Earth's spheres provide crucial insights into the dynamic processes and help in understanding the implications of mass redistribution for geophysical studies. The potential variations associated with these non-tidal loading or unloading effects can be estimated from the corresponding time-dependent spherical harmonic coefficients and load Love numbers $(k_n^{'}, h_n^{'})$ as Schröder et al. (2021)

$$\delta U(\lambda,\theta,r) = \frac{GM}{R}\sum_{n=0}^{\infty}\left(1 + k_n^{'} - h_n^{'}\right)\left(\frac{R}{r}\right)^{n+1}\sum_{m=0}^{n}\overline{P}_n^m(\cos\theta) \\ (\delta\overline{C}_{nm}\cos m\lambda + \delta\overline{S}_{nm}\sin m\lambda). \tag{2.21}$$

2.2.2 What a Clock Measures

A terrestrial clock measures the combined effect of gravity potential variation due to mass anomalies and the corresponding surface deformation in response to loading or unloading. Satellites like the GRACE mission measure changes in the Earth's gravitational potential caused by temporal mass anomalies. The potential change, δV, is calculated from the spherical harmonic coefficients derived from the satellite data. These measurements assume a fixed Earth model, meaning they do not directly account for surface deformations at the locations of the Earth. These surface deformations must be accounted for to fully understand the clock's readings. The deformation δh, which can be measured by GNSS, contributes to the total gravitational potential δU observed by the clock. In essence, clock measurements reflect the combined effect of mass anomalies and the corresponding Earth's response (deformation), providing a comprehensive view of the local gravity potential. Thus, the effective potential variation associated with a loading potential $V_n^{'}$ at a terrestrial clock site is (Vincent and Müller, 2023)

$$\delta U = \sum_{n}(1 + k_n^{'}(t) - h_n^{'}(t))V_n^{'} = \delta V - g\delta h \tag{2.22}$$

where $\delta V = \sum_n(1+k_n^{'}(t))V_n^{'}$ is what one can obtain from satellite-based measurements, $g\delta h = \sum_n h_n^{'}(t)V_n^{'}$, the potential variation due to geometrical distortions is given as vertical deformation δh from GNSS-like measurements. Clocks resting on the Earth's surface are always sensitive to the combined effect.

2.3 Global Height System

A global height system such as the International Height Reference System (IHRS) is essential in geodesy for providing a unified and consistent framework facilitating the basis for local and regional systems, global scientific research, infrastructure development, and disaster management (Sánchez, 2012; Ihde et al., 2017). Traditionally, different countries have used their own local height systems, which are typically based on mean sea level observations at nearby tide gauges. However, this leads to inconsistencies due to variations in sea level, geoid differences and measurement errors in the levelling approach (Delva et al., 2019).

Chronometric geodesy, using atomic clocks, provides a promising new approach to defining a global height system (Wu and Müller, 2022; Grotti et al., 2024). As detailed in section 2.1.1, according to the theory of general relativity, time ticks differently depending on the gravity potential. Highly accurate atomic clocks can measure these time or frequency differences, which directly relate to height differences between points on the Earth's surface. Chronometry does not require a continuous network of physical benchmarks and can be applied across regions that are difficult to access, making it a valuable complement or alternative to traditional levelling methods (Wu et al., 2018; Lisdat et al., 2019).

2.3.1 Geopotential Number and Physical Heights

Heights are crucial in geodesy for defining the position of points on the Earth's surface and for applications like navigation, engineering, and geophysics. Heights can be broadly classified into two categories: geometric and physical (Torge et al., 2023). Geometric heights, such as ellipsoidal heights, are measured from a reference ellipsoid, which is a mathematically defined surface approximating the shape of the Earth. These heights are typically obtained from GNSS or other satellite-based positioning systems. However, they do not consider the Earth's gravitational field, which means they do not reflect the "true" height in a physical sense, such as how water would flow (Jekeli, 2000). Physical heights, on the other hand, take into account the Earth's gravity field. They reflect the vertical distance along the direction of gravity from a reference surface such as the geoid, which approximates the mean sea level (Rummel and Teunissen, 1988). Physical heights are more meaningful in practical applications involving water flow, construction, and environmental studies because they represent heights in relation to the gravitational potential of the Earth.

Geoid-referenced heights are types of physical heights that fundamentally relate to the difference in gravitational potential between a reference surface (the geoid) and a point on the Earth's surface. This difference in gravity potential is expressed using the geopotential number

$$C_p = W_o - W_p \tag{2.23}$$

where W_o is the gravity potential on the geoid (approximates mean sea level) and W_P is the gravity potential at the point P. The three main types of geoid-referenced heights are orthometric heights, normal heights, and dynamic heights (Torge et al., 2023). Each of these height types is based on the geopotential number to account for spatial variations in the gravity potential and provides a practical vertical coordinate system for different applications (Sánchez et al., 2021).

The dynamic height is a potential-based measure converted into distance units using a constant scale factor. It is computed by dividing C_P by a constant nominal value of gravity, often chosen as a representative value for a mid-latitude location. The formula for the dynamic height is

$$H_P^D = \frac{C_P}{\gamma_0^{45}}. \tag{2.24}$$

The gravity value, γ_0^{45} corresponds to normal gravity at the ellipsoid surface at the latitude 45°(Hofmann-Wellenhof and Moritz, 2006). Despite this conversion, dynamic heights do not correspond to a true physical height above a reference surface but rather reflect the potential difference. This makes dynamic heights fundamentally different from orthometric or normal heights, which have direct physical interpretations as distances above sea level or another reference surface.

The orthometric height H_P^O or H (figure 2.4) represents the vertical distance from a point on the Earth's surface to the geoid, measured along the curved plumb line, which is perpendicular to the Earth's gravity field at every point, given as

$$H_P^O = \frac{C_P}{\overline{g}} \tag{2.25}$$

where $\overline{g}$ is the mean gravity along the plumb line from the geoid to the surface point. Orthometric heights are most useful for practical applications since they reflect true vertical distances above sea level. Measuring $\overline{g}$ would require gravity data at numerous points along the plumb line, which is challenging, time-consuming, and often impractical. Therefore, it is calculated from surface values applying models e.g., the Helmert reduction (Torge et al., 2023).

Then, normal height H_P^N or H^* (Figure 2.4) is a type of height used in geodesy to provide a geometrically interpretable measure of elevation that avoids assumptions about the density of the Earth's crust. Unlike orthometric heights, which are based on the Earth's gravitational field and require integration of gravity along the plumb line, normal heights are based on a reference normal gravity field which is an idealized gravity field that assumes a constant density and neglects local variations (Hofmann-Wellenhof and Moritz, 2006). The normal height is calculated from the ellipsoid by integrating the normal gravity field (U) along the normal plumb line to the telluroid point Q, U is defined based on the reference ellipsoid, which approximates the shape of the Earth. The normal height is calculated by

$$H_P^N = \frac{C_P}{\overline{\gamma_Q}}. \tag{2.26}$$

$\overline{\gamma_Q}$ is the average value of normal gravity along the normal plumb line from the ellipsoid surface to the telluroid point Q, which is given by the condition $W_P = U_Q$, i.e. where the normal gravity potential U_Q corresponds to the gravity potential value W_P of the corresponding surface point P.

2.3.2 Height System Unification

Traditionally, height systems are established using spirit levelling, which determines height differences relative to a reference surface, relying on precise optical instruments and the assumption that the mean sea level at a tide gauge represents the zero height reference (Torge et al., 2023). However, these classical techniques face limitations due to local variations in the geoid, errors in measurement propagation, and the labour-intensive nature of levelling over large distances (Gerlach

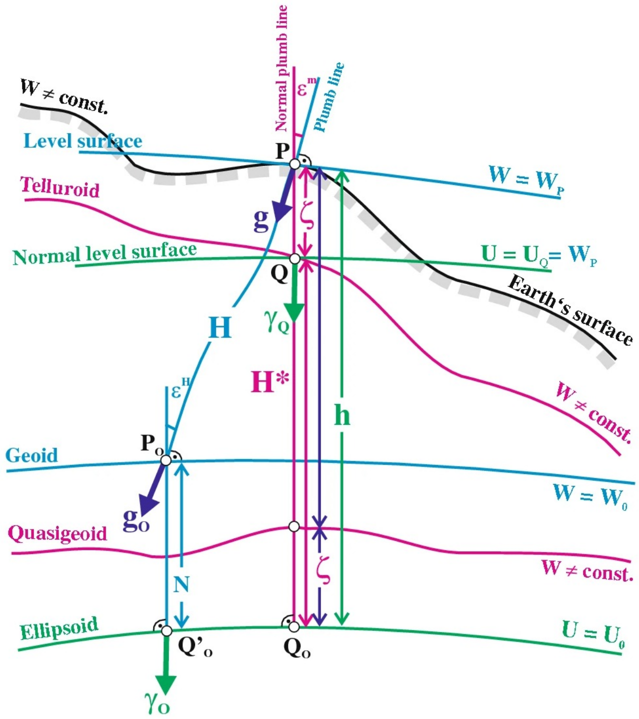

Figure 2.4: Heights and reference surfaces. (Sánchez et al., 2021)

and Rummel, 2013).

IHRS

The International Height Reference System (IHRS) represents a globally consistent framework for defining and measuring heights that are directly related to the Earth's gravity field (Sánchez et al., 2023). The IHRS was proposed to address the inconsistencies and limitations inherent in regional height systems, which are often based on different local datums and conventions, making them incompatible with one another. According to Ihde et al. (2017); Sánchez et al. (2021), the IHRS establishes a unified reference for physical heights by using the geopotential number $C_P = W_0 - W_P$ as vertical coordinate, where W_0 is the geoid potential and W_P is the potential at a given point P on the Earth's surface. This approach allows the IHRS to integrate various national and regional height systems into a common, globally consistent framework. To achieve this, the IHRS relies on the adoption of a common reference potential value, precise geoid models, local gravity data, and advancements in technologies such as satellite gravimetry (e.g., from missions like GRACE and GOCE), GNSS, and in future relativistic geodesy using atomic clocks (Gerlach and Rummel, 2013; Sideris et al., 2014; Rülke et al., 2012; Wu et al., 2018). The establishment of the IHRS involves a strategy that includes the development of standards, conventions, and methodologies to maintain and disseminate the reference frame, which is essential for diverse applications like sea-level monitoring, climate studies, and engineering projects across borders (Ihde et al., 2000). For the IHRS, the target accuracy for vertical station positions is ± 3 cm (1 cm long-term) and ± 0.03 m^2/s^2 in terms of geopotential differences at the global level (Ihde et al., 2017). Till now, achieving this accuracy requires the integration of both spaceborne and terrestrial gravity data, along with precise geodetic positioning techniques like GNSS (Gerlach and Rummel, 2013).

Unification Techniques

Unification using Global Gravity Models: The initial approach for height system unification involves the direct computation of the geopotential value W_P at a point P on the Earth's surface by introducing the ITRF coordinates using Global Gravity Models (GGMs) (Sánchez et al., 2021). GGMs provide the Earth's gravitational potential in terms of spherical harmonic coefficients derived from satellite observations (such as those from the GRACE-FO, GOCE) and other geodetic data sources. These models provide a detailed description of the global Earth's gravity field up to a specific degree and order (i.e. only up to a certain spatial resolution), allowing for the computation of the geopotential value W_P at any point on or above the Earth's surface. W_P can then be related to the conventional reference potential W_0 to compute C_P (Hofmann-Wellenhof and Moritz, 2006). This method allows for the integration of various regional and national height systems, which may be based on different datums, into a globally consistent framework (Rummel, 2012). The use of GGMs provides a significant advantage by enabling the computation of W_P across large areas without the need for extensive ground-based gravity measurements, thereby simplifying the unification process. Additionally, since GGMs are derived from high-precision satellite data, they can inherently account for both the static and temporal variations in the Earth's gravity field, providing an accurate and dynamic approach to height system unification. The GRACE-FO and GOCE missions provide geopotential models with an accuracy of about 1-2 cm in geoid height for spatial scales larger than 300 km (e.g. GRACE) and 100 km (e.g. GOCE) (Drinkwater et al., 2006; Wahr et al., 2006).

Unification using regional gravity field modelling: Another method for height system unification involves regional gravity field modelling with high resolution applying the Global Boundary Value Problem (GBVP) approach (Gerlach and Rummel, 2013; Denker, 2012). This method aims to compute the geopotential value W_P at specific points by combining high-resolution regional gravity data with GGMs from satellite missions like GRACE-FO and GOCE. The GBVP approach leverages the strengths of both global and regional data: the global models provide the low-frequency, long-wavelength part of the Earth's gravity field, while regional data enhance the spatial resolution and accuracy with detailed local gravity data. By solving the GBVP, it is possible to estimate the disturbing potential (the difference between the actual and normal gravity potentials) with high resolution, and subsequently, determine geopotential differences between height reference stations (Sideris et al., 2014). This method is particularly advantageous in regions where dense gravity data are available (e.g. Europe), allowing for the refinement of global geopotential models, e.g., European gravimetric (quasi) geoid (EGG2015) (Denker et al., 2009; Denker, 2015) and enhancing the consistency and precision of the International Height Reference Frame (IHRF).

In the context of height system unification, the GBVP can be approached in two main forms, the free GBVP (also known as the scalar or Molodensky problem) and the fixed GBVP (Hofmann-Wellenhof and Moritz, 2006). Each approach offers different methods for modelling the Earth's gravity field, which are crucial for determining geopotential values accurately (Wang, 2016). The Molodensky problem does not assume that the Earth's surface coincides with a specific equipotential surface, such as the geoid. Instead, a boundary surface that represents the Earth's shape more realistically by accounting for actual topography, on which the horizontal coordinates are known and where the vertical coordinate and the gravity potential are unknown, is defined, called telluroid (Grafarend, 1978). It is at a distance from Earth's surface to the point where the normal gravity potential U^* has the same value as W at the Earth's surface. The goal is to find the normal height of a point Q at the telluroid. The disturbing potential, $T = W - U^*$, is computed directly using gravity anomaly observations ($\Delta g = g_P - \gamma_Q$) (Hackney and Featherstone, 2003) on the Earth's surface. Then, by utilising a reference U_R^*, C_P is determined. Further, the height anomaly ζ defining the quasi-geoid, which relates to the normal height is derived. Hence, the Molodensky approach uses directly observable quantities (such as gravity anomalies) without reductions that require a model for the Earth's internal density distribution or gravity values along the plumb line. This makes it more practical in geodetic applications.

While the fixed GBVP assumes that a fixed reference surface, typically the geoid, coincides with a specific equipotential surface of the Earth's gravity field with unknown gravity potential (Wang, 2016). The objective is to compute the orthometric height above this fixed geoid surface. The difference between the actual gravity potential W_P at a point P and the gravity potential on the geoid W_0 can be computed from the given gravity disturbance observations, $\delta g = g_P - \gamma_P$ (Oliveira Jr et al., 2018). A downward continuation from Earth's surface to the geoid is performed with topographic reduction (Bouguer anomaly), gravity reduction (free-air anomaly) and ellipsoidal correction (Earth as sphere). Hence, this approach requires knowledge of the gravity along the plumb line between the geoid and the Earth's surface (Heck, 2011).

Unification of existing height systems through combination: One effective method to unify existing height systems is to incorporate these height systems into the observation equations of a GBVP (Sánchez et al., 2021; Rummel and Teunissen, 1988). This approach leverages the combination of ellipsoidal heights (from GNSS measurements) and orthometric or normal heights (from local levelling data) to compute the geopotential differences between local and global height reference systems (Sánchez and Sideris, 2017). The main idea is to express the height differences between local and global systems in terms of geopotential values and then solve for these differences using combined geodetic data.

Unification with atomic clocks: The use of highly precise atomic clocks, particularly optical clocks, offers a novel and promising method with the key advantage of their ability to directly measure differences in the Earth's gravity potential between two locations, providing a direct link to geopotential numbers and bypassing many of the limitations associated with traditional height determination methods (Wu et al., 2018; Wu and Müller, 2022). By comparing the frequency of signals from high-precision clocks at different locations, the differences of the gravity potentials (and therefore height differences) can be determined with better accuracy. These clocks can detect small variations in the gravity potential, a direct point-wise almost real-time measurement that satellite missions cannot achieve (Vincent et al., 2025).

There are two methods to implement clock networks for a global height system: (i) realisation of clock-based IHRS with a hierarchical network of clocks of highly accurate atomic clocks distributed across different locations globally, and (ii) unification of existing local height systems (Wu and Müller, 2022). The network method of (i) comprises core clocks located at primary reference stations, often within national metrological institutes. These core clocks serve as the most stable and accurate reference points in the system, providing a benchmark for comparing other clocks in the network. National clocks are deployed at major national geodetic stations, and regional clocks are established at additional key points to ensure comprehensive coverage and connectivity. To tie the entire clock network to a global height reference, a datum clock is selected, typically positioned at a globally recognized reference point with a well-defined geopotential value, serving as the "zero point" of the height system. The second method focuses on unifying existing local height systems by using clock networks to measure error parameters (tilts and offsets) between them (Wu et al., 2018; Vincent et al., 2025). Local height systems, typically based on different vertical datums, can be referenced to a global equipotential surface (the geoid) by determining the differences in gravity potential using clock measurements. With clock-derived geopotential numbers at specific points in different height systems, the differences (offsets, tilts, etc.) between these systems can be defined and corrected through a joint adjustment with levelling-based local heights. This method allows for the integration of regional and national height systems into a single, consistent global framework.

2.3.3 Height System Unification Applying Chronometric Levelling

Chronometric levelling offers a novel approach to resolve these limitations by using highly accurate clock observations to determine the relative height difference between two points. Unlike traditional methods, clock observations are directly referenced to a common reference, in the ideal case the geoid, thus eliminating errors associated with datum variations, such as offsets and tilts. By measuring the difference in gravity potential between two points, clocks provide a more direct and globally consistent reference (Delva et al., 2019). Moreover, this method takes into account nearly all possible uncertainties associated with clock observations, such as temporal stability, accuracy, link uncertainties (fibre and space links), tidal effects, etc. offering a more precise and reliable means of height determination across different regions. The benefits of using clock networks in height system unification are quantified via simulations. The unification process employs a joint adjustment approach, integrating local height observations with simulated clock observations to establish a globally consistent height system (Wu et al., 2018). This methodology involves defining a common reference datum to which all local height systems are unified (figure 2.5).

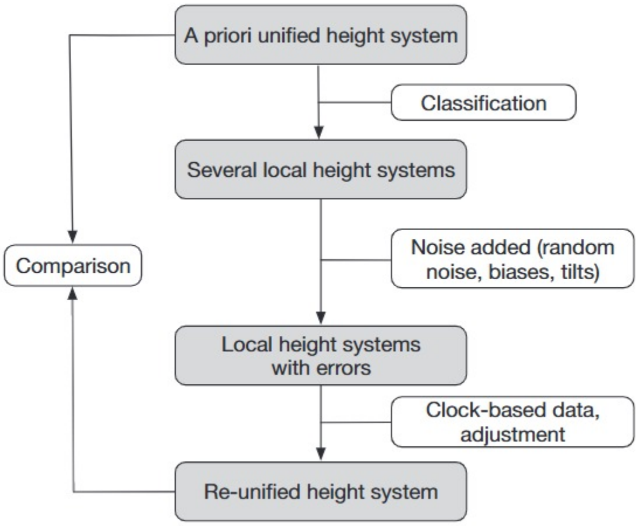

Figure 2.5: The scheme of simulator (Wu et al., 2018)

First, an a priori height system is selected as the reference framework. In order to produce the local height values that need to be unified, levelling points are classified into different Local Height Systems (LHSs) based on their proximity to designated tide gauges and their administrative attribution. Local height observations are then generated by introducing various systematic error parameters into the a priori height values. These error parameters are encountered in classical height determination methods, including offsets (representing deviations from the global geoid), latitudinal and longitudinal tilts, tide gauge tilts, mountain tilts, and noisy levelling tilts with respect to pre-defined unifying datum. Closed loop simulations (2.3.6) are carried out using local heights and clock measurements as observations to estimate reunified heights along with the transformation parameters between LHSs. By assuming a random noise (RN), offsets (OT), and systematic tilts (ST) that exist between the LHS with respect to the pre-defined unifying datum, local height values (in terms of gravity potential difference equivalents) are generated. The accuracy of the reunification is determined by comparison to the a priori height values.

2.3.4 Error Sources in Local Height Observations

Local height systems around the globe are typically defined with respect to local tide gauges, which are in turn referenced to a local undisturbed mean sea level. These regional height observations rely on classical geodetic techniques, such as spirit levelling and gravimetric measurements (Torge et al., 2023). However, these methods introduce several sources of error, leading to inconsistencies between different local systems (Gruber et al., 2014; Wu et al., 2018; Sánchez et al., 2021). Common errors include:

1. Offsets, $c^L = OT^L/g$ (cm): Deviations from the global geoid, which create systematic biases in different height reference systems.

2. Latitudinal Tilt, a^L (cm/degree): A gradual increase of deviations with latitude.

3. Longitudinal Tilt, b^L (cm/degree): Similar to latitudinal tilt, but along the east-west direction.

4. Tide Gauge Tilt, t^L (cm/degree): A conical error pattern originating from the reference tide gauge itself, which can be affected by local sea level changes, land subsidence and uplift where levelling errors increase with distance to the tide gauge.

5. Mountain Tilt, m^L (cm): We keep in mind that in mountain regions levelling may be sparser and have increased errors if there are steep ascents. Those errors or measurement noise due to challenges in levelling at higher elevations are termed m^L. Errors that depend on the elevation of levelling points are modelled as increasing proportionally to the height of the point (e.g., an increase with a factor of local height/500m). An elevation step of E = 500 m, is chosen as an arbitrary value that determines the offset ranges.

6. Noisy Levelling Tilt, n^L (cm/degree): Errors that show up along specific erroneous levelling lines due to accumulated inaccuracies in the levelling process.

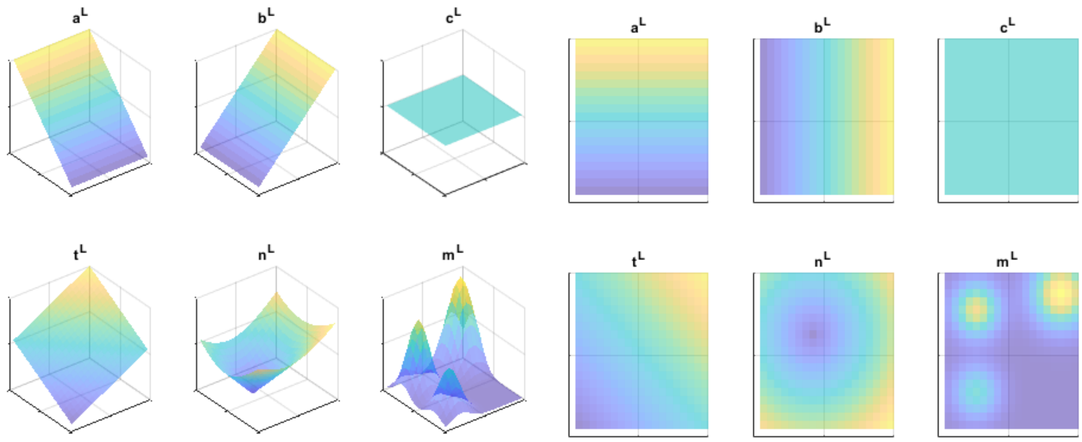

Figure 2.6: 3D-view (left) and 2D-view (right) of assumed error parameters in local height observations considering LHS defined in an XYZ system. The color scale represents the magnitude of errors symbolically, with blue indicating the minimum and yellow indicating the maximum error values.

The observation equations for local heights (H_i^L) in terms of geopotential numbers

(C_i^L) generated from the a priori C_i^U is

$$C_i^L = C_i^U + ST_i^L + OT_i^L + RN. \tag{2.27}$$

This synthetic dataset represents the local height systems with realistic error characteristics, enabling the simulation of real-world scenarios.

2.3.5 Realistic Clock Observations

To simulate the clock observations, several levelling points within each local height system are designated as clock sites. At these locations, the clock observations are generated by calculating the differences in geopotential numbers between them. For the following the framework of the first-order post-Newtonian theory for clock comparison is employed (Müller et al., 2018; Denker et al., 2018). The gravity potential differences are taken as clock observations instead of relative frequency shifts. This requires first converting all a priori heights into corresponding geopotential numbers, which represent the gravity potential at the Earth's surface. Clock intrinsic uncertainties both statistical and systematic (CE), external effects those caused by tidal effects (TE) (Voigt et al., 2016), propagation delay in terms of link uncertainty (Lisdat et al., 2016; Riedel et al., 2020) (PD), etc. which induce dynamic height changes, must be carefully modelled and removed. By comprehensively modelling these effects, the simulated clock observations provide a realistic basis for integrating clock-based geodetic data into the process of height system unification. The observation equations for clock measurements (ΔW_{ij}) are generated from the a priori/unified geopotential numbers (C_i^U), as follows,

$$\Delta W_{ij} = -(C_i^U - C_j^U) - (TE_i - TE_j) + PD_{ij} + CE_i + CE_j. \tag{2.28}$$

Clock Intrinsic Uncertainties and Time Correlations

Clock observations are affected by the intrinsic uncertainties (CE) of the two clocks being compared. Each clock has a random but constant offset from its true frequency, reflected by its inherent systematic uncertainty. In the context of height system unification, we focus primarily on clocks with systematic uncertainties in the order of 10^{-18} (Type B uncertainty). This is because the random (Type A) uncertainty, which arises from statistical noise, can be mitigated by increasing the averaging time, effectively reducing its contribution to the overall uncertainty (Grotti et al., 2024).

Systematic uncertainties of atomic clocks are modelled as a random but constant offset, which is unique to each clock and is fixed for a given clock over the observation period. Hence, it is unpredictable but remains within the specified uncertainty range. Here it is treated as a normally distributed variable with a zero mean and a standard deviation of 10^{-18}. A normal distribution model is particularly adopted because systematic biases can statistically cancel out to yield an effective zero-mean uncertainty. This assumption aligns with the idea that positive and negative deviations are equally likely.

If the same clock participates in multiple observations, its systematic offset will affect multiple comparisons, leading to correlations between those observations. In our study, we assume that each observation between two clocks is made at a unique epoch. No clock is simultaneously involved in observations with multiple sites at the same epoch. Under this assumption, generally, the systematic uncertainties of the clocks are treated as uncorrelated between observations. This assumption simplifies the treatment of uncertainties in the network and allows for independent modelling of each clock pair. In subsequent stages of the analysis, time correlation between clock observations is incorporated (4.1.3). This is achieved by considering correlations between observations involving the same clocks within each local height system. By addressing these time correlations of systematic uncertainties across observations, we refine the adjustment procedure, thus enhancing the accuracy and realism of the network model.

Clock Comparison/ Link Uncertainties

The clock comparison uncertainties in PD can be further divided into three independent contributions:

1. Statistical Noise of the Clocks: This reduces with increasing averaging time, as the stochastic fluctuations in the clock signal average out.

2. Noise from the Signal Distribution (Link Noise): This includes random and systematic errors in the medium used to link the clocks for comparison.

3. Systematic Errors in the Link: These are constant or slowly varying biases that arise from imperfections in the link infrastructure or methods.

The significance of each contribution to PD depends on the type of link used for clock comparisons and the averaging time applied to reduce the random noise.

Optical Fibre Links:

When optical interferometric fibre links (Williams et al., 2008) are employed for clock comparisons, the complexity of handling PD is significantly reduced. This is because:

1. Rapid Reduction in Link Noise: The statistical noise from fibre links diminishes much faster with averaging time than the intrinsic noise of the clocks themselves (Lisdat et al., 2016). Typically, after averaging for durations exceeding 100 seconds, the clock noise becomes the dominant source of uncertainty.

2. Negligible Systematic Errors: Fibre links can achieve systematic uncertainties as low as 10^{-19} under realistic field conditions. This was demonstrated in experimental loop configurations (Koke et al., 2019), where such values were achieved consistently. Consequently, the contribution of link-related uncertainties becomes negligible compared to the systematic uncertainties (CE_i) of the clocks.

3. Practical Averaging Requirements: Clock-related statistical noise can be reduced to below the systematic uncertainty level with sufficient averaging. For state-of-the-art optical clocks, averaging periods ranging from several hours to days are sufficient, which are feasible under current operational conditions. Thus, the systematic clock uncertainties dominate the error budget, simplifying the analysis, as the error contribution from the fibre links can be neglected.

Free-Space Links:

When infrastructure for optical fibre links is unavailable or the distance between the clocks is too big, free-space links become necessary. These links often rely on space-based platforms and employ either microwave or optical technologies. Free-space links introduce additional challenges. Current capabilities include existing microwave-based technologies which can achieve uncertainties at the low 10^{-17} level (Fujieda et al., 2018; Jian et al., 2023). Promising developments, such as the ACES (Atomic Clock Ensemble in Space) mission (Cacciapuoti and Salomon, 2011), are expected to enable global frequency transfer with uncertainties as low as 5×10^{-17}. The ACES mission uses MicroWave Link (MWL) and European Laser Timing (ELT) for time transfer. Current studies predict time uncertainties ($\Delta\tau$) of approximately 4 ps with one day of averaging, corresponding to frequency uncertainties near 5×10^{-17} (Cacciapuoti et al., 2024).

Optical free-space links, still under development (Caldwell et al., 2023; Rovera et al., 2016), aim to achieve uncertainties at the 10^{-18} level. While not yet operational, these systems offer a promising solution for future clock comparisons over large distances. Free-space links experience non-reciprocal behaviour due to ionospheric dispersion and drift in relay station delays. Also, their inherent instability requires longer averaging times to suppress statistical noise, further complicating the comparison process.

For free-space links, we consider two scenarios in our simulations:

- Presently achievable uncertainties of 10^{-17};
- Optimistic future optical link uncertainties of 10^{-18}.

In practical clock comparison scenarios, the choice of link technology and the averaging time play critical roles in determining the dominant uncertainty source. For optical fibre links, CE dominate due to negligible link contributions. In contrast, free-space links, especially at current and near-future levels of development, exhibit significant PD uncertainties, requiring careful consideration in the error budgets.

External Effects on Clock Observations

In real-world scenarios, clock observations are affected by the Earth's fluctuating gravity potential, which includes contributions from various external factors. Among these, tide-generating potentials play a significant role and require precise modelling and reductions to ensure the needed accuracy of clock-based measurements. These tidal effects are accounted for by applying precise models to predict and subtract them from the clock observations. Any residual error from these models represents the model error, which remains as a source of uncertainty in the simulated clock data.

The primary contributors to tidal variations in the Earth's gravity potential as described in section 2.2.1 are: Solid Earth Tides (SET), Ocean Load Tides (OTL), pole tides (POL), Length-of-Day Tides (LOD), and atmospheric tides. While LOD and atmospheric tidal potentials contribute to the overall tidal effects, their magnitude falls below the sensitivity threshold of high-precision optical clocks (10^{-18}, corresponding to $\approx 0.1\ \mathrm{m^2/s^2}$) (Voigt et al., 2016). Therefore, these components are typically neglected in clock-based geodetic studies.

To account for the significant tidal effects (SET, OTL, POL), we use established tidal potential models and data processing packages:

- Solid Earth Tides, Pole Tides: These are modelled using a modified version of the ETERNA34 (PREDICT program) Earth tide data processing package (Wenzel, 2022), with the HW95 (Hartmann and Wenzel, 1995) tidal potential catalogue (TGP).
- Ocean Load Tides: OTL variations are computed using the SPOTL3.3.0.2 package (Agnew, 2012), based on the EOT11a ocean tide model (Savcenko and Bosch, 2011).

2.3.6 Clock-based Adjustment

The core of the method involves a reunification process through a joint adjustment of the local height observations (equation (2.27)) and the simulated clock observations (equation (2.28)). The clock observations, which provide the relative height differences between points with respect to a common pre-defined datum, are considered independent and free from the systematic errors associated with classical height determination techniques. By incorporating these clock observations, we aim to correct the various errors present in the local height systems and align them to a common reference datum. The unknown parameters in this reunification process include both the assumed error parameters for each local system and the unified height values. Through the joint adjustment, these parameters are estimated simultaneously, providing a re-unified height solution that minimizes discrepancies between the local systems and aligns them with the re-unified datum.

We assume having a certain number of clocks distributed across each LHS with multiple connections between them. To obtain overdetermined solutions, the number of clock observations must exceed the total number of introduced error parameters. If all clocks are interconnected, the total number of unique observations is given by $\binom{n}{2}$, corresponding to the number of unique combinations between n clocks.The accuracy of the reunification is assessed by comparing the results with the a priori height values.

Least-squares Adjustment Theory

Least-squares adjustment is a mathematical approach used to find the best fit solution for an over-determined system, where the number of observations exceeds the number of unknown parameters (Koch, 2013; Richter, 1995). The goal is to minimize the sum of the squared differences (residuals) between the observed values and the estimated values predicted by the model. This method is widely applied in geodesy and many other fields for parameter estimation, data fitting, and error analysis.

In real-world applications, different observations may have different levels of precision or reliability. Weighted least squares (WLS) is an extension of the ordinary least squares (OLS) method that accounts for these differences by assigning a weight to each observation (Huber, 2011). The weight represents the reciprocal of the variance of the observation's measurement error. This means that observations with smaller variances (higher reliability) receive higher weights, while those with larger variances receive lower weights (Koch, 2013). The weighted least-squares solution can be formulated as

$$\mathbf{X} = (\mathbf{A}^T\mathbf{P}\mathbf{A})^{-1}\mathbf{A}^T\mathbf{P}\mathbf{l} \tag{2.29}$$

where $\mathbf{X}$ is the vector of unknown parameters to be estimated, $\mathbf{A}$ is the design matrix.$\mathbf{l}$ is the vector of observations and $\mathbf{P}$ is the weight matrix, which represents the precision of the observations.

In our simulation, the observation matrix $\mathbf{l_{nc+nw\times1}}$ consists of the local heights in terms of geopotential numbers $\mathbf{C_{nc\times1}}$ and clock observations $\mathbf{\Delta W_{nw\times1}}$. The functional model expressed is given as

$$\begin{bmatrix}\mathbf{C}\\ \mathbf{\Delta W}\end{bmatrix} = \begin{bmatrix}\mathbf{A1} & \mathbf{A2}\\ \mathbf{A3} & \mathbf{A4}\end{bmatrix}\begin{bmatrix}\mathbf{X1}\\ \mathbf{X2}\end{bmatrix} \tag{2.30}$$

where $\mathbf{A1}, \mathbf{A2}, \mathbf{A3}, \mathbf{A4}$ are the components of the design matrix $\mathbf{A}$ based on the observation equations (2.27) and (2.28). The vector of unknown parameters $\mathbf{X_{nc+nu\times1}}$ is represented by $\mathbf{X1} = \{..., C_i^U, ...\}'_{nc\times1}$, the set of re-unified heights and $\mathbf{X2} = \{a^L, b^L, c^L, t^L, m^L, n^L\}'_{nu\times1}$, the set of error parameters from every LHS (L). Here, the weight matrix is $\mathbf{P} = \begin{bmatrix}\mathbf{P1} & \mathbf{0}\\ \mathbf{0} & \mathbf{P2}\end{bmatrix}$ where, $\mathbf{P1}$ and $\mathbf{P2}$ represent weighting matrices for $\mathbf{C}$ and $\mathbf{\Delta W}$ when there is no correlation.

Homocedasticity and Heterocedasticity

According to Koch (2013), the weight matrix $\mathbf{P}$ is a crucial component in the least-squares adjustment process, reflecting the stochastic properties of the observations. For uncorrelated observations, the weight matrix $\mathbf{P}$ is typically diagonal, where each diagonal element is the inverse of the variance of the corresponding observation:

$$\mathbf{P} = \operatorname{diag}\left(\frac{1}{\sigma_1^2}, \frac{1}{\sigma_2^2}, \ldots, \frac{1}{\sigma_n^2}\right). \tag{2.31}$$

However, in cases where observations are correlated, the weight matrix is no longer diagonal. Instead, it incorporates the covariances between the different observations, represented by the inverse of the covariance matrix $\mathbf{D}_l$ of the observations

$$\mathbf{P} = \mathbf{D}_l^{-1}. \tag{2.32}$$

When the variances of the observational errors are constant (equal) across all observations, it is referred to as a homoscedastic case (Hawkins, 1981). Here, the least-squares solution can be computed with a simple weighting scheme (e.g., equal weights for all observations, $\mathbf{P} = \mathbf{I}$). On the other hand, heteroscedasticity occurs when the variances of the observational errors differ across the observations (Müller and Stadtmüller, 1987). This is more realistic in many real-world scenarios, such as for geodetic data, where measurements can vary in precision depending on the instrument, location, or environmental factors. In heteroscedastic cases, the weighting matrix follows equation (2.31) when no correlations exist or equation (2.32) with correlated observations. The covariance between two observations can be calculated using the correlation coefficient ($-1 > r_{ij} < 1$) and the standard deviations of the two variables. The formula is:

$$D_{ij} = r_{ij} \cdot \sigma_i \cdot \sigma_j. \tag{2.33}$$

This relationship is especially useful in geodetic data processing and adjustment models where correlations between observations must be accounted for in the variance-covariance matrix.

Koch (2013) emphasizes that the correct construction of the weight matrix is essential to obtaining an optimal solution in the least squares adjustment process, as it ensures that all sources of uncertainty and correlation in the observations are appropriately accounted for. The choice of the weights directly impacts the adjustment results, affecting the precision and reliability of the estimated parameters. By incorporating the weight matrix into the least-squares adjustment, the method can effectively handle different scenarios like the presence of outliers, etc., yielding more accurate and meaningful estimates of the unknown parameters.

Robust Parameter Estimation using the Huber Estimator

Robust parameter estimation methods aim to reduce the effect of outliers in the data, which can distort parameter estimates in classical least squares. The Huber estimator is a widely used approach for robust parameter estimation (Huber, 2011). It combines the benefits of least squares (sensitivity to small residuals) and least absolute deviations (resilience to large residuals) with an iterative reweighting algorithm. It uses a piecewise loss function that is quadratic for small residuals (like least squares) and linear for large residuals (like least absolute deviations). This makes it robust to outliers while maintaining efficiency for

Gaussian-distributed data. The loss function is defined as

$$\rho(v) = \begin{cases} \frac{1}{2}v^2 & \text{if } |v| \leq k, \\ k(|v| - \frac{k}{2}) & \text{if } |v| > k, \end{cases} \tag{2.34}$$

where here v is the residual, and k is the tuning parameter. The algorithm iteratively updates weights assigned to the residuals, depending on their magnitude relative to k:

$$w_i = \begin{cases} 1 & \text{if } |v_i| \leq k, \\ \frac{k}{|v_i|} & \text{if } |v_i| > k, \end{cases} \tag{2.35}$$

where w_i is the weight for the residual v_i. Residuals are standardized by dividing them by the estimated standard deviation (σ) to ensure comparability.

The parameter k in the Huber estimator is a critical threshold that determines the treatment of the residuals based on their magnitude (Freedman, 2006). For residuals smaller than k, the estimator applies a quadratic loss function, mimicking the behaviour of least squares and prioritizing sensitivity to small deviations. For larger residuals, the estimator transitions to a linear loss function, reducing the effect of outliers and enhancing the robustness. The value of k directly affects the balance between robustness and efficiency: smaller k values improve robustness by minimizing the impact of outliers but may reduce efficiency for Gaussian-distributed data. Conversely, larger k values make the estimator more sensitive to smaller residuals while diminishing its ability to handle outliers effectively.

Huber selected $k = 1.345\sigma$, where σ is the standard deviation, as this value ensures approximately 95% efficiency under Gaussian assumptions (Huber, 2011). This means the Huber estimator can perform nearly as well as the least squares method for normally distributed data while remaining robust against outliers.

Closed-Loop Simulation

This unification approach is validated using a closed-loop simulation, where the re-unified heights obtained from the adjustment process are compared with the a priori height values (Wu et al., 2018). The true error e^t is defined as the difference between the local heights and a priori heights in terms of geopotential numbers. The accuracy of the unification is determined based on the differences between the reunified and a priori heights which is termed as adjusted error (e^a). The equations of e^t and e^a are given as

$$e_i^t = C_i^L - C_i^{U_{apriori}} \tag{2.36}$$

$$e_i^a = C_i^{U_{reuni}} - C_i^{U_{apriori}}. \tag{2.37}$$

The standard deviation of the estimated error parameters from the covariance matrix is also of critical importance as it gives the significance of the estimated residuals. By using both clock and traditional levelling observations in this manner, the method ensures that the local height systems are rigorously adjusted to a consistent global height framework, enhancing the accuracy and reliability of the IHRF in the near future.

2.4 Global Sea Level Change Monitoring

Sea level change is a critical indicator of climate change, impacting coastal communities, ecosystems, and global weather patterns (Lindsey, 2007). Monitoring sea level changes is essential for understanding both short-term variations due to tides, storm surges, and longer-term trends driven by thermal expansion of seawater, melting ice sheets, and glaciers (Cazenave and Nerem, 2004). However, to fully grasp the complexities of sea level change, it is important to distinguish between relative sea level, which includes local land motion, and absolute sea level, which measures the sea surface heights relative to a globally consistent reference (Wöppelmann and Marcos, 2016). Moreover, integrating new technologies, such as precise clocks, allows for monitoring vertical land motion with a few cm accuracy, enhancing our understanding of sea level variations at both local and global scales (Vincent and Müller, 2024).

2.4.1 Relative Sea Level vs. Absolute Sea Level

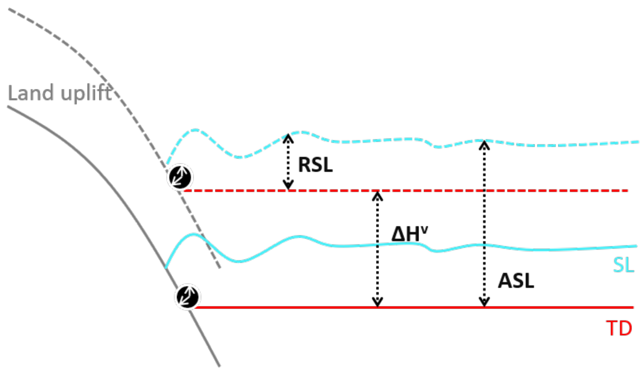

Figure 2.7: Absolute Sea Level (ASL) and Relative Sea Level (RSL) change with respect to tidal datum (TD) in the case of land uplift ΔH and sea level (SL) rise (Vincent and Müller, 2024)

Relative Sea Level

Relative Sea Level (RSL) refers to the height of the sea surface relative to a specific reference point on land, such as a tide gauge station, which is fixed to a coastal structure or a benchmark (figure 2.7). It reflects the combined effects of changes in the ocean volume and local vertical land movements at the measurement site (Jeon et al., 2018). Thus, RSL is a localized measure that varies depending on both oceanographic processes and geophysical changes affecting the land.

Tide gauges are the primary instruments used to measure RSL (Douglas, 2001). They are installed along coastlines and are usually attached to a stable structure, such as a pier or a seawall, and provide a consistent reference point over time. These measurements are affected by various factors, including tides, waves, barometric pressure changes, and seasonal variations. To account for land movement at tide gauge sites, GNSS stations are often colocated with tide gauges (Larson et al., 2013). GNSS provides precise measurements of vertical land motion, crucial for distinguishing true sea level changes from land movements (Dawidowicz, 2014). By combining tide gauge data with GNSS measurements, scientists can correct for local vertical land motion and thus better understand sea level changes attributed to oceanographic processes (Peng et al., 2021). According to the PSMSL's documentation, long-term sea level trends can be measured with accuracies of $\pm$ 0.3 to 1 mm/year, depending on the correction for land motion and the length of the data record (Woodworth and Player, 2003).

Local land movements, such as subsidence (sinking) or uplift (rising) of the ground, significantly influence RSL measurements. These movements can be caused by various factors, including tectonic activity (e.g., earthquakes, faulting), post-glacial rebound (also known as glacial isostatic adjustment or GIA), sediment compaction, and anthropogenic activities like groundwater extraction or mining (Nicholls et al., 2021). The relative sea level will appear to rise more in regions experiencing land subsidence and less, or even fall, in regions experiencing land uplift (Shirzaei et al., 2021; Steffen and Wu, 2011). Oceanographic processes such as the thermal expansion of seawater (due to global warming), changes in ocean currents, wind patterns, and regional changes in salinity also affect RSL (Gornitz, 1995). Seasonal variations, storm surges, and local meteorological events can cause short-term fluctuations in RSL. RSL measurements are often tied to a local datum or reference level, such as the "Mean Sea Level" (MSL) or a "tidal datum" established over a specific time period (e.g., the average sea level over 19 years) (Gill and Schultz, 2001). The use of local datums means that RSL data are inherently region-specific and may not be directly comparable between different locations without appropriate transformations.

The limitations of RSL measurements include local biases and inconsistencies in reference datums with variations in both spatial and temporal scales. Short-term fluctuations in sea level due to tides, weather events, or seasonal changes can obscure longer-term trends in RSL. Since RSL is measured relative to a local benchmark, it inherently reflects local conditions and may not represent global sea level changes accurately. Local land movements (e.g., subsidence or uplift) can skew RSL data, making it difficult to discern whether observed changes are due to actual changes in sea level or changes in the land.

Absolute Sea Level

Absolute Sea Level (ASL) refers to the height of the sea surface relative to a fixed, global reference frame (Dietrich, 2014). Unlike Relative Sea Level, which measures changes relative to local benchmarks or tidal datums, ASL provides a measure that is consistent across the globe, irrespective of local land movements (figure 2.7). This makes ASL crucial for understanding global sea level rise and other large-scale changes (Baker, 1993). ASL is referenced to a global mean surface, often the geoid.

One of the primary methods for measuring ASL is satellite altimetry (Fu and Cazenave, 2000). Satellites such as those of the JASON series or Copernicus Sentinel-6 provide high-precision measurements of sea surface heights from space (Benveniste et al., 2020; Donlon et al., 2021), which are then referenced to the global geoid and ellipsoid models. Alternatively, as mentioned in the previous section, GNSS stations installed on land can be used to measure vertical land movements, which can then be combined with tide gauge data to obtain accurate ASL measurements (Peng et al., 2021).

ASL measurements offer a uniform method for monitoring sea level changes globally, providing insights into phenomena such as global warming and polar ice melting. Integrating data from various sources (e.g., satellite altimetry, GNSS, tide gauges) and ensuring consistency across different measurement systems can be challenging. The accuracy of ASL measurements depends on the precision of the geoid model used as a reference (Featherstone, 2001). Variations and updates of the geoid models can affect the interpretation of sea level data.

2.4.2 Benefits of Land Motion from Clocks

The physical height at a point on the Earth's surface is subject to continuous variation, primarily due to external tidal effects and non-tidal mass distributions within the Earth system, see (Voigt et al., 2016). Tidal effects encompass a range

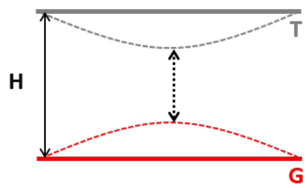

(a) loading

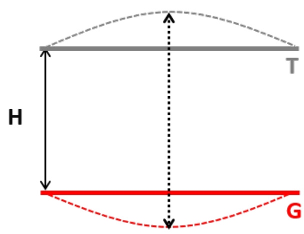

(b) unloading

Figure 2.8: Loading and unloading effects on physical heights which depend on the geoid (G) height and vertical displacements of the Earth surface (T) (Vincent and Müller, 2024)

of phenomena, such as solid-Earth tides and ocean-load tides caused by the gravitational forces of external celestial bodies like the Sun, Moon, and other planets. These effects also include centrifugal forces resulting from polar motion, which generate pole tides, and variations in the Earth's angular velocity, which lead to length-of-day tides, along with atmospheric tides. Non-tidal effects, on the other hand, arise from the redistribution of mass within the geosphere, hydrosphere, atmosphere, and biosphere, all of which impact the geopotential at any given point by inducing mass changes and associated vertical displacements (Schröder et al., 2021). On the deformable Earth's surface, the potential variations due to the vertical displacement also have to be accounted for by defining the total potential variation (figure 2.8) as discussed in section 2.2.2.

Using terrestrial clock observations, it is possible to infer these physical height changes, in contrast to GNSS which only provides measurements of ellipsoidal height changes. By combining RSL measurements, which reflect changes in the local sea surface height relative to a nearby reference point, with time-variable land motion data (ΔH^v) derived from clock observations, one can compute ASL changes with respect to the geoid. This relationship can be expressed mathematically as

$$ASL = RSL + \Delta H^v. \tag{2.38}$$

Atomic clocks offer an alternative by providing a direct reference to a global equipotential surface, such as the geoid. By using highly precise atomic clocks as benchmarks, both land and sea level measurements can be referenced to the same equipotential surface, thereby maintaining uniformity without the need to consider regional tidal datum variations. This method ensures that the measurements are consistently tied to the global geoid, eliminating the biases and uncertainties associated with local vertical datums. Here, clocks directly measure changes in gravity potential, which is independent of whether the mass changes occur above or below the Earth's surface, meaning that clocks can detect changes regardless of whether they are due to surface or subsurface mass movements.

Tidal and non-tidal effects induce variations in physical heights, represented by ΔH^v_{tidal} for tidal effects and $\Delta H^v_{non-tidal}$ for non-tidal loading and unloading effects, respectively (Vincent and Müller, 2024). The overall change in the physical height ΔH^v can be obtained from clocks, where the static part cancels out for clocks at a fixed location or can be reduced with levelling:

$$\Delta H^v = \Delta H^v_{tidal} + \Delta H^v_{non-tidal}. \tag{2.39}$$

Sea level change has two contributions, classified into: "Steric" and "Eustatic" (Cazenave and Nerem, 2004). Steric changes involve the expansion or contraction of seawater due to temperature (thermosteric) and salinity (halosteric) variations. Ocean mass changes, detected directly by GRACE and GRACE-FO, are primarily driven by the addition or removal of water to and from the oceans due to processes like melting ice sheets, glaciers, and variations in terrestrial water storage and atmosphere. While steric changes do not alter the total mass of the oceans, they affect sea level by changing the volume of the seawater. Here, clocks and altimetry observe the combined effect.

Incorporating atomic clocks into sea level monitoring offers the advantage of directly referencing measurements to a globally consistent surface, the geoid. This method not only mitigates the issues of local biases and datum inconsistencies but also allows real-time and pointwise tracking of sea level changes by accounting for all relevant gravity potential changes.

3 Application I - Detection of Time-variable Gravity Signals

3.1 Effect of Temporal Centrifugal Potential Variations

A terrestrial optical clock is sensitive to the gravity potential, which reflects the combined effects of gravitational and centrifugal forces at a given location, as described in equation (2.12). This chapter focuses on evaluating the potential of optical clocks to observe time-variable gravity signals by simulating gravity potential variations at points of interest. The impact of centrifugal potential variations is then estimated and compared with the clock's uncertainty.

An assumption is made that the Earth's rotational velocity is constant over time, to analyze how local displacements at each latitude produce time-dependent variations in the centrifugal potential. For a fixed latitude and angular velocity ($\omega = 2\pi/86164$ rad/s), Earth's temporal rotational variations depend on the distance from the rotation axis ($r(t)\cos\theta$) (Roman, 2020).

$$Z(r) = \frac{1}{2}\omega^2 r(t)^2 \cos^2\theta. \tag{3.1}$$

The radius corresponding to each latitude (θ) can be computed as described by (Clynch, 2002):

$$R(\theta) = \sqrt{\frac{(a^2\cos\theta)^2 + (b^2\sin\theta)^2}{(a\cos\theta)^2 + (b\sin\theta)^2}} \tag{3.2}$$

where a and b represent the semi-major axis and semi-minor axis of the ellipsoid. The centrifugal potential at latitudes of 0°, 22.5°, 45°, 67.5°and 90°are calculated (figure 3.1(left)). Later, the centrifugal potential variations at each latitude for vertical displacements (d) from 0 to 4 m are computed with $r(t) = R(\theta) + d$ for various latitudes (figure 3.1(right)).

The maximum effect of the centrifugal potential is at the equator ($\theta = 0$), $Z(r_{equator}) = 108155.12$ m^2/s^2 where a radial displacement of 4 m results in a centrifugal potential variation of 0.13 m^2/s^2 ($\approx 10^{-18}$). Therefore, temporal rotational variations, which are primarily due to these radial displacements, are negligible and can be ignored when simulating the clock observations.

For a terrestrial clock B, $W_B = V_B + Z_B = W_0 - C_B$ (geopotential number $C_B = W_0 - W_B$), where V_B and Z_B represents the gravitational and centrifugal potentials. One can define a static (C_B^{static}) and time-variable part (δC_B) for C_B. Hence, if we consider the fractional frequency change of a terrestrial clock B with

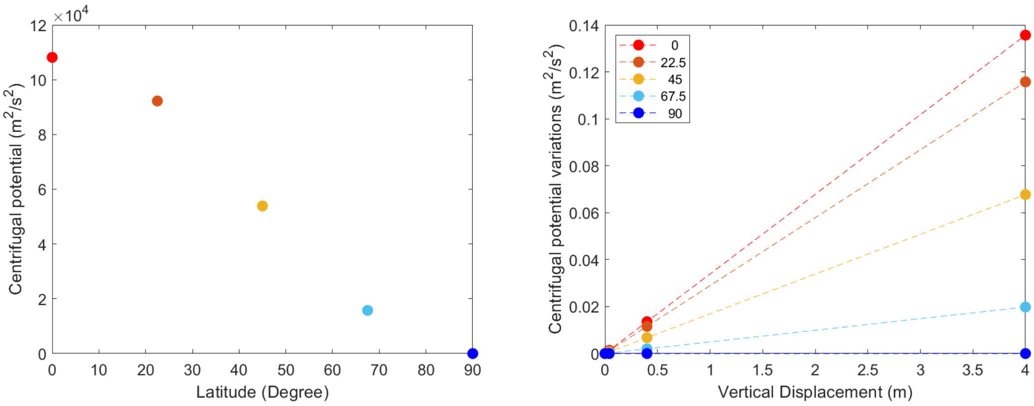

Figure 3.1: Centrifugal potential at selected latitudes in m^2/s^2 (left) and centrifugal potential variations at selected latitudes for vertical displacements (d) up to 4 m (right)

respect to a reference clock A ($\delta C_A \approx 0$), equation (2.11) can be modified with $W_B - W_A = C_A^{static} - C_B^{static} - \delta C_B$

$$\frac{\Delta f}{f} = \frac{f_A - f_B}{f_B} \approx \frac{C_A^{static} - C_B^{static} - \delta C_B}{c^2}. \tag{3.3}$$

As the temporal variation in the centrifugal potential is negligible, δC_B can be approximated by the effective gravitational potential variation δU_B equation (2.14). The corresponding time-variable geopotential changes at B ($\approx \delta U_B$) can be obtained from

$$\delta U_B = -\frac{\Delta f}{f} c^2 + C_A^{static} - C_B^{static} \tag{3.4}$$

when A is considered stable such that δC_A is negligible enough. C_A^{static} and C_B^{static} can be obtained from levelling techniques. Thus, the time-variable changes at location B are purely gravitational.

3.2 Concept of Reference Clock in Timeseries Analysis

Clock observations always involve two clocks since the relative fractional frequency change is our primary observation. For time series analysis, such as detecting time-variable gravity signals, we aim to extract the temporal variations of geopotential changes at a site of interest as given by equation (3.4). This requires a reference clock at a location where temporal geopotential changes are small enough to be below the sensitivities of the clocks in use, or where the instantaneous geopotentials can be modeled with uncertainties within the clock sensitivities. The other possibility is to use a space-based reference, preferably at a geostationary satellite where the gravitational effect of the Earth can well be modelled. But, there will be limitations from satellite visibility and exposure time.

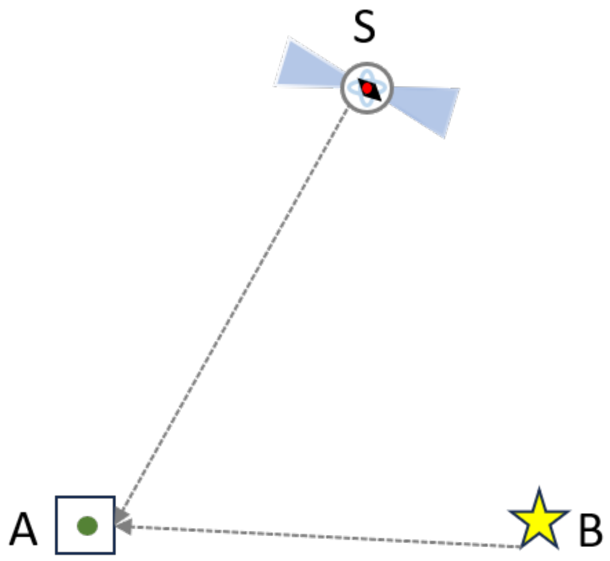

Figure 3.2: Configuration of reference clocks in time-series analysis illustrating how a clock at site of interest (B) can be linked to a stable space-based reference clock (S) and a ground-based reference/national clock (A)

Our approach defines a configuration of reference clocks, consisting of one space-based reference and one ground-based reference. Clocks located at sites of interest, where the geopotential changes need to be determined, should be connected to the ground-based clock, which can be designated as a national clock for the particular regional height system. In this setup, all ground reference clocks are connected to the space-based clock reference, where accurate modelling of geopotential time variations with uncertainties less than the clock sensitivity is possible. This configuration allows us not to be concerned about the stability of the reference clocks. Also, the number of space links can be reduced to a single connection of the national clock to the satellite clock. To compute the temporal variations at the site of interest (Clock B), simultaneous connections from the ground reference (Clock A) to B and from the space reference (Clock S) are required. Mathematically, it can be represented as

$$\frac{\Delta f_{AB}}{f} = \frac{W_A - W_B}{c^2} \tag{3.5}$$

$$\frac{\Delta f_{AS}}{f} = \frac{W_A - W_S}{c^2} \tag{3.6}$$

$$\frac{\Delta f_{BS}}{f} = \frac{\Delta f_{AS}}{f} - \frac{\Delta f_{AB}}{f} = \frac{W_B - W_S}{c^2} \tag{3.7}$$

$$\delta U_B = -\frac{\Delta f_{BS}}{f}c^2 - W_S + W_0 - C_B^{static} \tag{3.8}$$

in agreement with equation (3.4).

3.3 Simulation Strategy and Data Description

The goal is to separately evaluate the magnitude of different time-variable gravity signals as clock observations. These time-variable signals can be expressed in terms of geopotential variations at the sites of interest. Geopotential is unaffected whether the loading or unloading occurred beneath or above the clock location. Atomic clocks provide us with the direct measurement of the local geopotential, the only existing method to probe Earth's gravity potential for geodetic applications. As mentioned in section 2.2.2, clocks measure the combined effect of mass variations and associated surface deformations. Non-tidal gravity signals such as seasonal hydrological signals, linear variations due to present-day ice mass loss, secular Glacial Isostatic Adjustment (GIA) signals, and co-seismic and post-seismic signals are analysed in the following.

The aim of this simulation study is to demonstrate that the networks of high-performance clocks can enhance traditional geodetic techniques for detecting and quantifying mass variations on Earth. To achieve this, we focus on five regions characterized by different dominant mass redistribution processes: the Himalayas, the Amazon, Greenland, Fennoscandia and Japan. These regions represent diverse temporal changes in mass, such as glacial melting, hydrological cycles, GIA and seismic signals from earthquakes.

The effective potential variations, denoted as δU in equation (2.22), which result from these mass redistribution processes, are quantified. The simulations of those clock observations, that measure these potential variations, require combining data from both GRACE and GNSS measurements. GRACE data provide information on temporal potential variations due to mass changes, while GNSS data give the corresponding surface deformations. This integration allows us to model the clock observations on a deformable Earth.

We select clock sites based on existing GNSS stations from the Nevada Geodetic Laboratory (NGL) network. The stations are chosen for their availability of long time series, which is essential for accurately capturing temporal variations. The GRACE monthly solutions, specifically the ITSG-2018 dataset, are used to model mass variations. These solutions encompass the full range of hydrological, cryospheric, and GIA signals, with reductions applied for mass variations in the oceans and atmosphere as part of the standard processing (Kvas et al., 2019). The time-variable gravity signals are estimated on a monthly basis as differences to the static gravity field model EIGEN-6C4, which represents a long-term mean state (Förste et al., 2014).

To model the potential variations due to surface deformation, we use GNSS time series of vertical displacements. Specifically, the up components of the NGL daily time series solutions, given in the IGS14 reference frame (closely related to ITRF2014), provide monthly averages of these displacements (Blewitt et al., 2018). Non-tidal loading effects, such as atmospheric loading, ocean bottom pressure, and surface hydrology, are initially included in these GNSS solutions. However, since Non-Tidal Atmospheric Loading (NTAL) is a dominant factor affecting these displacements, we subtract it to isolate the signals of interest. Daily averages of the 3-hourly NTAL data from GFZ (Dill and Dobslaw, 2013) are computed and removed from the GNSS time series, ensuring consistency with the GRACE seasonal signals in test cases of Himalaya and Amazon.

By doing so, we simulate the seasonal signals from terrestrial water storage variations (in the Himalayas and Amazon), linear trends representing either current ice mass variations (in Greenland) or GIA signals (in Fennoscandia) and co-seismic and post-seismic variations (Japan - Tohoku earthquake). These variations are treated as potential clock observations, $\delta U \approx \frac{\Delta f}{f} c^2$, where $\Delta f / f$ represents the relative fractional frequency change. A clock with a sensitivity of 10^{-18} would be capable of detecting potential variations as small as 0.1 m^2/s^2. This level of sensitivity illustrates the potential of using high-performance clocks for detailed monitoring of mass redistribution processes on Earth.

3.4 Case A: Himalaya

The Himalayan region, often referred to as the "Water Tower of Asia," is a critical reservoir of fresh water, holding one-fifth of the Earth's total freshwater storage (Shamsudduha and Panda, 2019). With a glacier coverage of approximately 33,000 km^2, this region is pivotal for the hydrological balance in Asia. These glaciers feed some of the world's major river systems, including the Ganges, Brahmaputra, and Meghna rivers, which are vital sources of water for millions of people across several countries.

The climatic conditions in the Himalayas vary significantly from east to west. The Eastern Himalayas are characterized by a wetter climate, receiving substantial rainfall due to the influence of the Indian summer monsoon. In contrast, the Western Himalayas are relatively drier (Bookhagen and Burbank, 2010). This variation in climate leads to differences in glacial melt patterns, snow accumulation, and river discharge rates across the region.

For geodetic studies, particularly in monitoring temporal gravity signals, the Himalayas present a unique opportunity. The GNSS stations distributed in this region provide valuable data for observing the impacts of hydrological and glacial processes. These stations, located primarily within the Ganges-Brahmaputra-Meghna (GBM) river basin, can be considered specific sites for potential clock observations (figure 3.3).

The GBM river basin is one of the largest and most dynamic river systems globally. It is particularly sensitive to variations in terrestrial water storage, driven by seasonal changes in precipitation, snow melt, and glacial runoff. The region experiences significant mass redistribution due to the monsoon's influence, which leads to considerable fluctuations in water storage over time. These variations are critical for understanding regional hydrology and its contribution to global sea-level changes.

By integrating high-performance optical clocks at these GNSS stations, we can

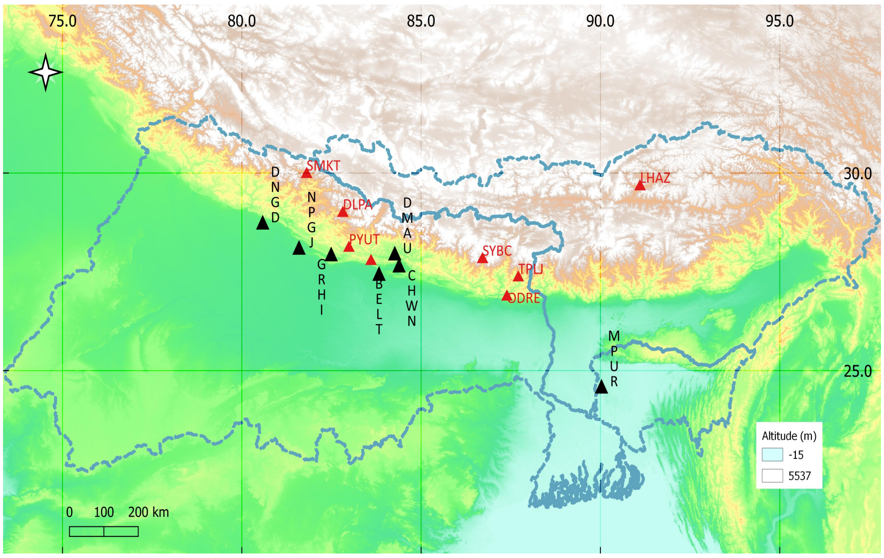

Figure 3.3: Himalayan region with the Ganges-Brahmaputra-Meghna river basin and assumed clock sites (high-altitude stations (red), low-altitude stations (black))

enhance our ability to detect and quantify the temporal variations in the Earth's geopotential associated with these dynamic processes. Clock observations in the Himalayas can help capture the intricate patterns of mass changes due to glacial melting and terrestrial water storage, providing a more refined understanding of how these processes contribute to global sea-level change. This methodology allows us to complement traditional geodetic techniques with a novel approach to monitor the Earth's changing mass distribution with high accuracy.

3.4.1 Simulation of Hydrological Signals as Clock Observations

In this simulation study, the focus is on capturing the seasonal hydrological signals in the Himalayan region by integrating detrended (to extract the seasonal signals alone) GRACE and GNSS datasets (as outlined in equation (2.22) in section 2.2.2). These datasets allow us to simulate the effective potential variations that would be observed by clocks. By fitting these seasonal potential variations into annual cycles, we can visualize the kind of signals that high-performance clock networks could detect.

A collection of 15 clock sites distributed across the Himalayan region was considered, with 8 stations located at high altitudes and 7 at lower altitudes. The distinction between high-altitude and low-altitude stations provides insights into how altitude affects the observed potential variations, offering a comprehensive understanding of the region's seasonal hydrological dynamics. Daily variations of NTAL result in surface deformations as large as ≈ 1 cm at some stations, e.g., at DNGD, that should be reduced from the GNSS data to extract the hydrologically driven vertical displacements alone. The NTAL reduced daily GNSS time series is provided in figure 3.4. As provided in section 3.3, in order to com-

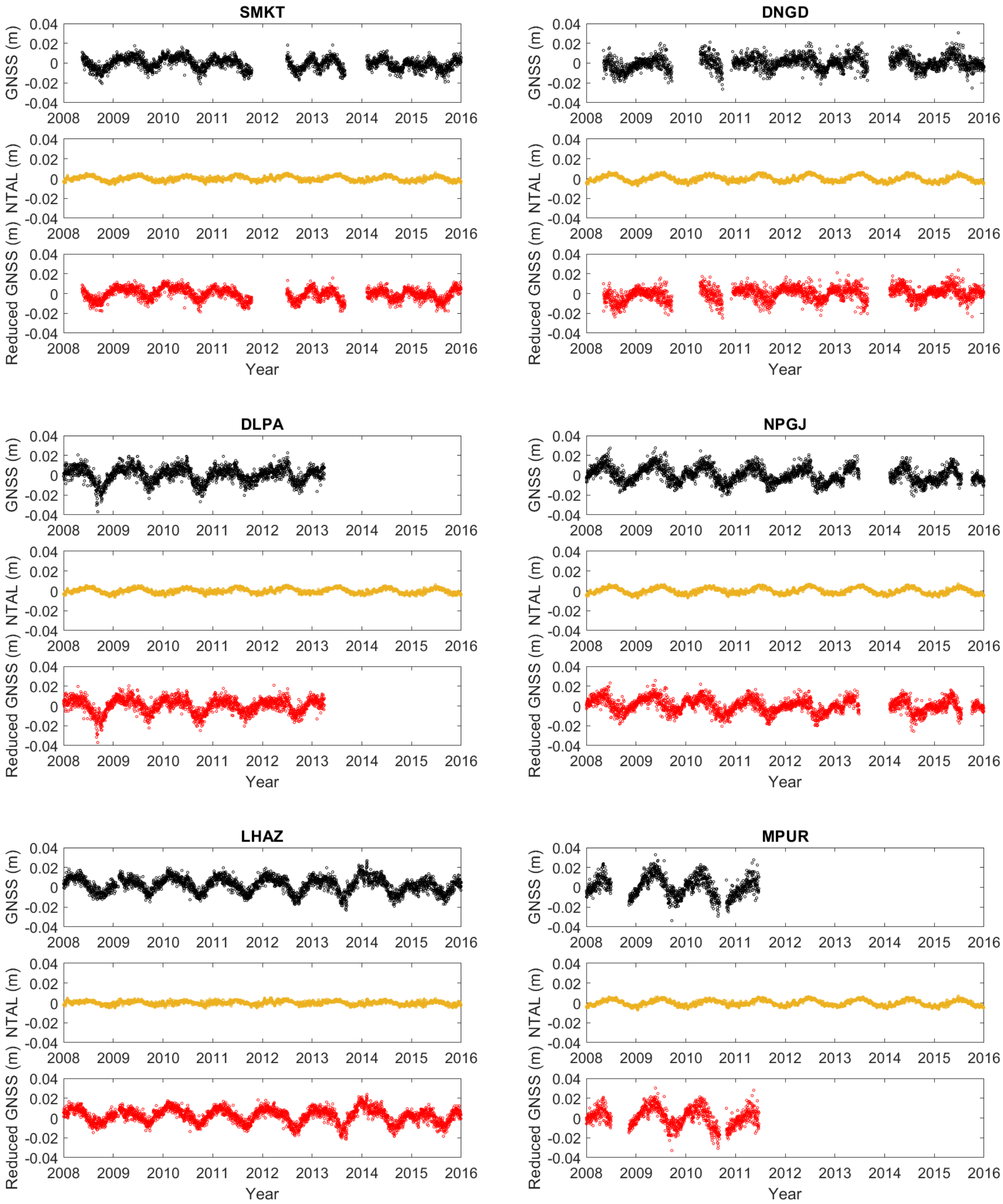

Figure 3.4: Vertical displacements due to seasonal loading/unloading at Himalayan high-altitude sites (SMKT, DLPA, LHAZ) and low-altitude sites (DNGD, NPGJ, LHAZ). The upper panel shows the total seasonal GNSS vertical displacements, and the middle panel illustrates the non-tidal atmospheric loading in terms of height changes. The lower panel provides the NTAL reduced GNSS displacements indicating the seasonal component due to hydrological signals.

bine with monthly potential variations from GRACE, the monthly mean of daily GNSS measurements is computed. NGS provides daily GNSS solutions with mm accuracy, the monthly averages reduced the uncertainties further into the sub-millimeter level, which is beyond the assumed clock uncertainty.

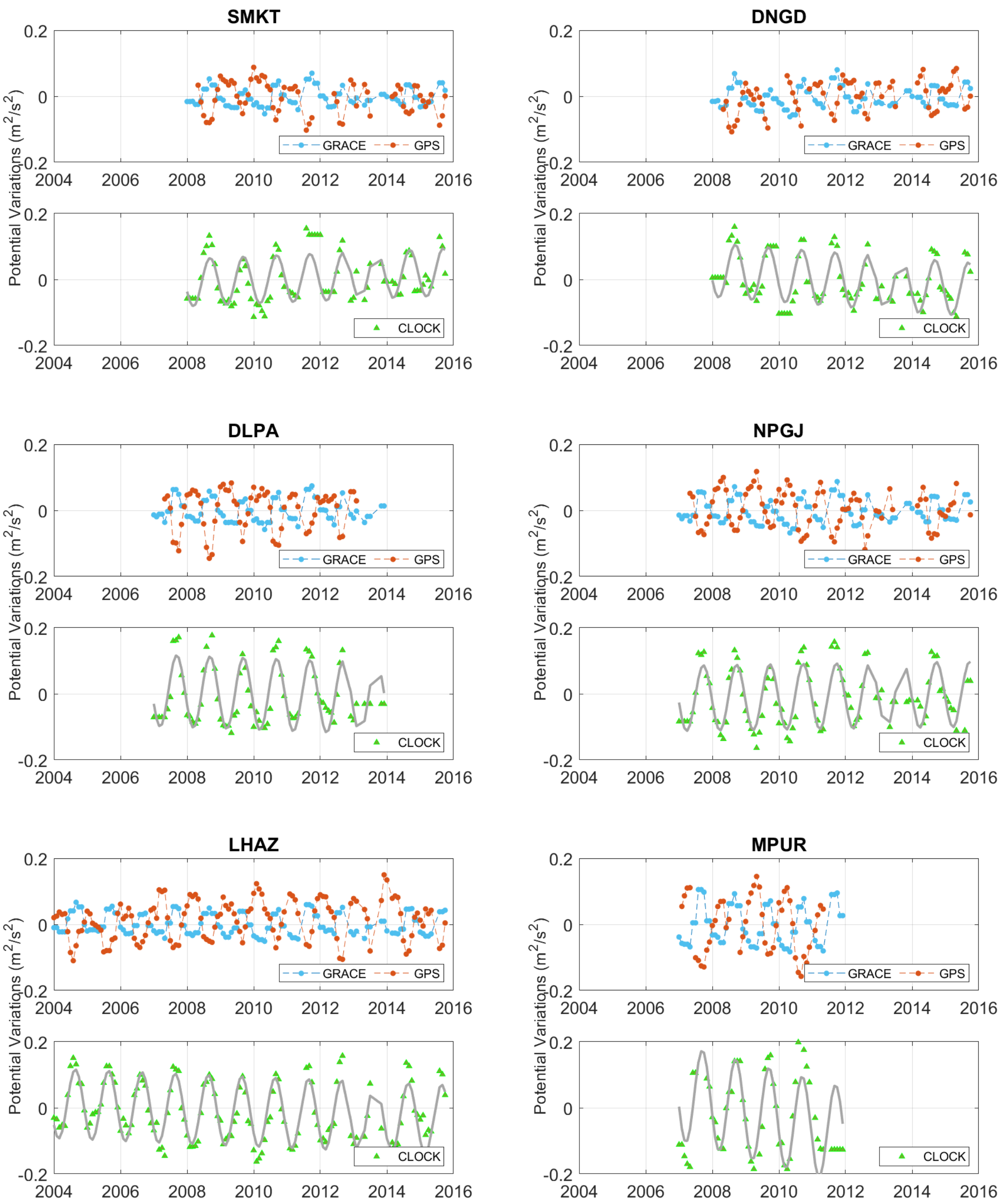

Figure 3.5: Seasonal hydrological signals in terms of potential variations at Himalayan high altitude sites (SMKT, DLPA, LHAZ) and low altitude sites (DNGD, NPGJ, LHAZ). The upper panels show the separate effect of mass anomalies (GRACE) and vertical deformation (GNSS). The lower panels give the combined effect as it could be observed by clocks (CLOCK), with the fitted seasonal signal in gray.

The simulated clock observations illustrated in figure 3.5 reveal that the Himalayan region exhibits seasonal variations in effective potential with a range of approximately $[-0.2\ 0.2]$ m^2/s^2. Such variations are well within the detection capabilities of clock networks with a performance level of 10^{-18}, corresponding to an uncertainty of 0.1 m^2/s^2. This demonstrates that high-precision clocks can indeed detect these subtle, yet significant changes in the Earth's geopotential caused by seasonal hydrological processes. This highlights the potential of clock networks to provide valuable data on the temporal changes in Earth's mass distribution, particularly in regions like the Himalayas, where seasonal hydrological processes play a significant role.

3.4.2 Clocks as Probes for Monsoon Dynamics in the Himalayas

The Himalayan region's precipitation pattern is heavily affected by the dynamics of the Indian monsoon, which is responsible for a substantial portion of the annual rainfall. The monsoon typically peaks in August, bringing intense precipitation across various locations and altitudes in the region. This peak timing remains consistent irrespective of specific geographic or topographic variations, underscoring the dominance of the monsoon system in shaping the hydrological cycle. The northeastern part of India experiences an early and prolonged rainy season, with precipitation gradually diminishing in intensity as the monsoon system progresses westward. This gradual spread plays a critical role in the redistribution of water mass within the region, influencing the local gravity potential. By measuring effective potential variations, clocks can trace the water mass accumulation and its spatial-temporal redistribution during the monsoon season.

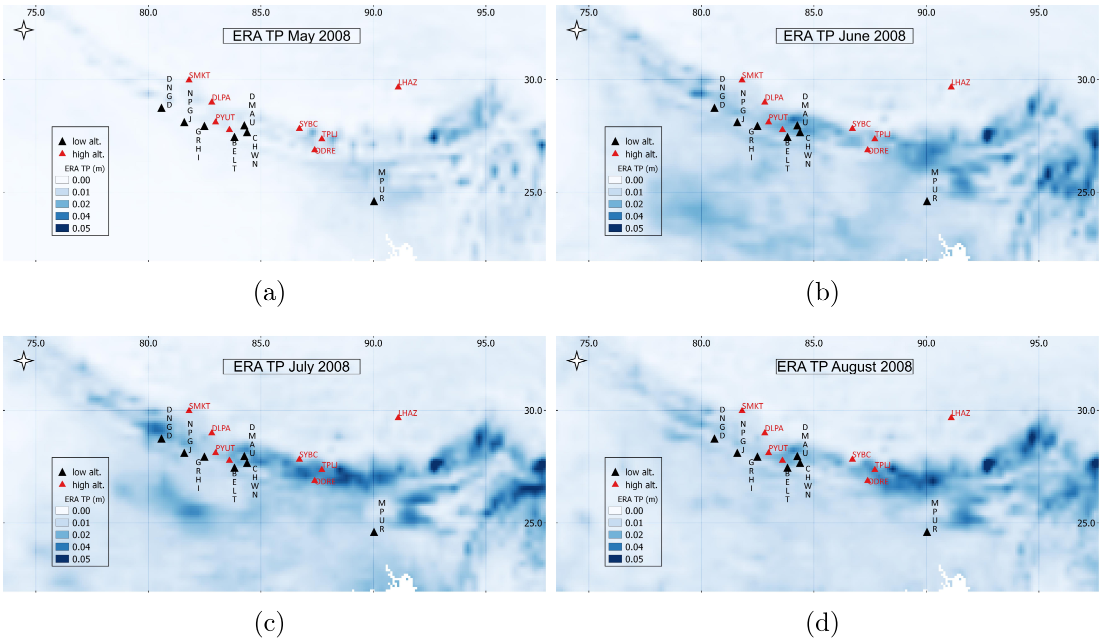

(a) (b) (c) (d)

Figure 3.6: ERA-5 monthly total precipitation grids in the Himalayan region for the months May (a), June (b), July (c) and August (d) in 2008

The ERA-5 ECMWF reanalysis product further highlights the monsoon's evolution by providing detailed Total Precipitation (TP) data for the key periods from May (early onset) till August (peak intensity) given in figure 3.6. The annual phases and amplitudes derived from the fitted clock observations at all stations align closely with the precipitation patterns (table 3.1). With this correlation, it becomes possible to study the monsoon's strength and its geographic progression at different sites.

Table 3.1: Annual phase and amplitude of seasonal signal at Himalayan clock sites.

Station	Annual phase (deg)	Amplitude (m^2/s^2)
DNGD	112.36	0.082
SMKT	111.93	0.072
NPGJ	97.26	0.099
DLPA	111.84	0.109
LHAZ	128.07	0.106
MPUR	107.18	0.146

In the future, a time series of clock measurements could allow for detailed monitoring of precipitation dynamics, including the early onset and prolonged patterns observed in northeastern India. This capability has significant implications for understanding and modelling the monsoon's impact on regional hydrology, water resource management, and climatic variability. Clocks, with their sensitivity to effective potential variations, can bridge the gap between atmospheric observations and geodetic measurements, offering a unified framework to study monsoon-induced changes.

3.5 Case B: Amazon

The Amazon basin, the world's largest river basin, is not only an iconic geographical feature but also a critical component of the Earth's hydrological and ecological systems. Spanning over 7 million square kilometers, the Amazon rainforest supports a vast diversity of life and plays a crucial role in regulating global climate patterns through carbon storage and water cycling. The seasonal dynamics of Terrestrial Water Storage (TWS) within this region is substantial, driven by monsoon precipitation, river discharges, and evapotranspiration processes.

The simulation focuses on four strategically chosen sites across the Amazon basin, selected based on the availability of long-term hydrological data and their suitability for clock placement. Figure 3.7 provides a visual representation of these sites. At these locations, TWS changes are modelled over an annual cycle, capturing the hydrological extremes that define the Amazon's seasonal rhythm. For instance, the peak TWS typically coincides with the wet season when precipitation dominates, while the lowest TWS occurs during the dry season as water storage depletes.

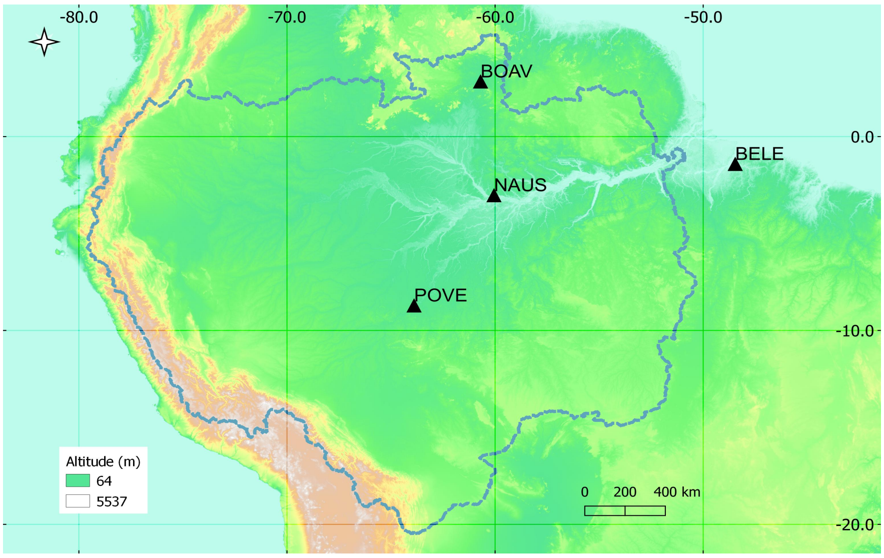

Figure 3.7: Simulated clock sites in the Amazon basin

3.5.1 Simulation of Hydrological Signals as Clock Observations

The methodological approach for simulating hydrological signals as clock observations in the Amazon Basin involves modelling TWS variations and translating these into gravity potential changes detectable by high-precision clocks. This simulation is based on equation (2.22), which connects TWS-induced mass redistribution to potential variations. NTAL is generally more pronounced in regions with higher elevations and greater atmospheric pressure variability. In the Amazon, NTAL is generally less pronounced than in the Himalayan region due to its lower altitude. However, the region's vast size and the influence of the Intertropical Convergence Zone (ITCZ) lead to seasonal variations in atmospheric pressure. These variations coincide with the seasonal shifts in rainfall and trade winds. While NTAL in the Amazon will not reach the levels observed in the Himalayas, its contribution is less than 5 mm.

The simulated TWS change in the Amazon region demonstrates a peak-to-peak range of $[-0.5, 0.5]$ m^2/s^2, which is significantly higher than the range observed in the Himalayan region (~ 0.2 m^2/s^2). This disparity is primarily due to the immense precipitation and hydrological activity in the Amazon, which is one of the most water-rich regions on Earth. The Amazon basin experiences a dominant seasonal hydrological cycle, with intense rainfall during the wet season contributing to large-scale changes in water mass distribution. Such a dynamic cycle generates more substantial gravity potential changes that clocks can observe.

Figure 3.8, showcasing the simulated clock signals at the stations BOAV, NAUS, BELE, and POVE, reflects the robust seasonal TWS variations in the Amazon. These stations highlight the basin-wide hydrological dynamics. Stations located closer to the Amazon River or its tributaries are likely to experience stronger gravitational potential variations, e.g. NAUS, due to the massive water mass

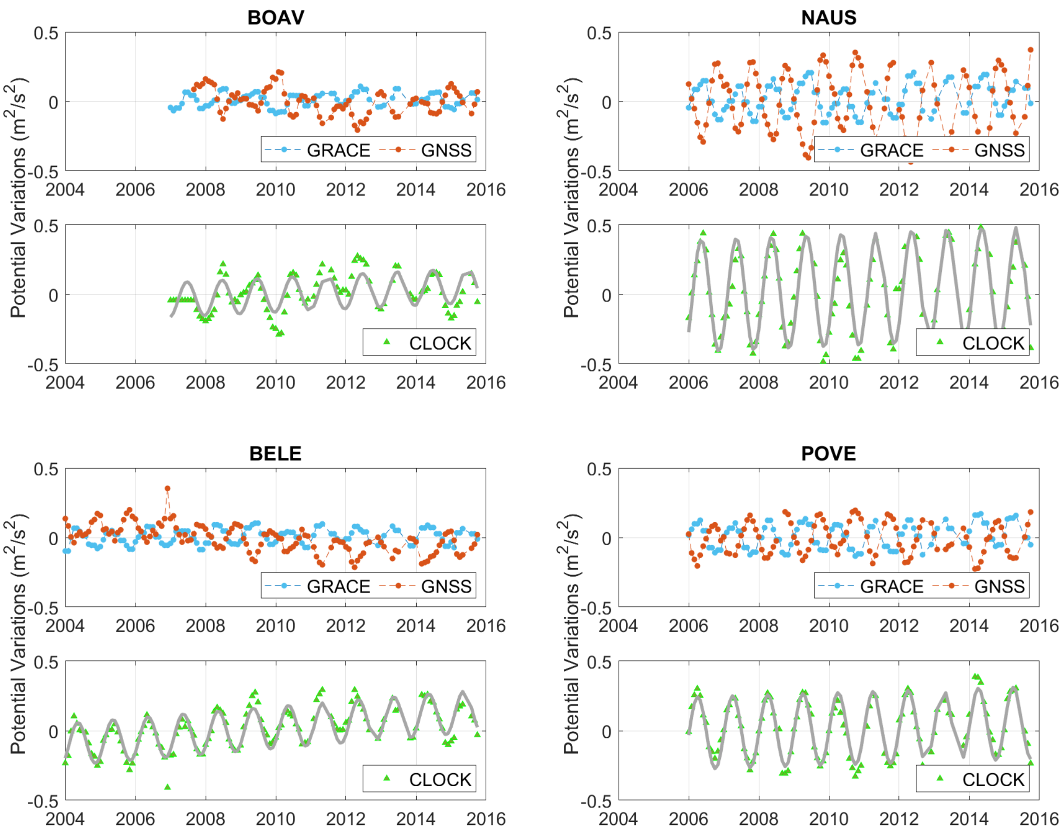

Figure 3.8: Simulated potential variations of hydrological signals at the Amazonian sites BOAV, NAUS, BELE and POVE. The upper panels show the variations separately derived from GRACE and GNSS. The lower panels show the combined effect of height change (GNSS) and mass change (GRACE) as it could be observed by clocks (CLOCK), with the fitted seasonal signal in gray.

movements during seasonal flooding and rainfall. The redistribution of water, both horizontally (floodplain dynamics) and vertically (groundwater recharge and river discharge), intensifies these signals, as the river and surrounding areas act as focal points for hydrological processes. The Amazon's distinct characteristics-like extensive rainfall, low-altitude floodplains, and large river systems—amplify the magnitude of TWS changes, making it a prime region for demonstrating the potential of clock-based hydrological monitoring. These observations highlight the promise of high-precision clocks in capturing diverse hydrological phenomena at contrasting regions globally.

3.5.2 Amazon's Seasonal Secret

The Amazon's hydrological cycle showcases distinct seasonal characteristics on either side of the equator, driven by the interplay of rainfall variability and trade wind directions. The northern and southern regions of the Amazon exhibit contrasting rainy seasons, which are influenced by the annual migration of the ITCZ

(Espinoza et al., 2019). This migration follows the Sun's position relative to the equator and is a key driver of precipitation patterns in the tropics.

In the northern Amazon (e.g., BOAV station), the rainy season typically occurs from June to August, with peak rainfall observed in July. This is due to the northward shift of the ITCZ during the northern hemisphere's summer, bringing moist trade winds and heavy rainfall. Conversely, in the southern Amazon, the rainy season spans from November to April, with peak rainfall around April. This pattern is attributed to the ITCZ moving southward during the southern hemisphere's summer, drawing moisture-laden winds from the Atlantic Ocean.

Table 3.2: Annual phase and amplitude of seasonal signals at clock sites in Amazonia

Station	Annual phase (deg)	Amplitude (m^2/s^2)	Month of maximum peak
NAUS	-129.37	0.406	May
POVE	-92.96	0.261	April
BOAV	-169.54	0.126	July
BELE	-129.34	0.153	May

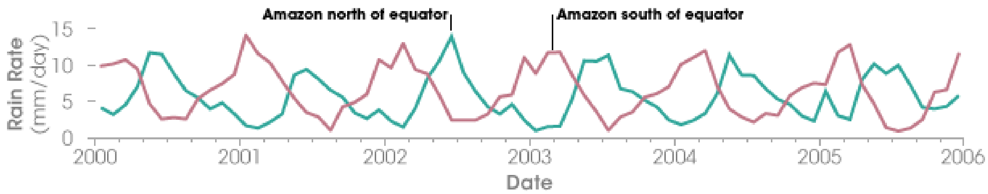

Figure 3.9: Rainfall variability in the north and south of the equator in the Amazon region. Image taken from NASA Earth Observatory (Lindsey, 2007)

Table 3.2 clearly illustrates these different seasonal properties through phase values derived from simulated clock observations, while figure 3.9 visually represents the temporal shift in rainfall. These results align with observations from studies such as those by Lindsey (2007), which highlight the role of trade winds and ITCZ dynamics in shaping Amazonian rainfall patterns.

The capability of clock networks to monitor these regional hydrological properties is a promising avenue for the future. High-precision clocks can provide unprecedented temporal and spatial resolution, capturing subtle variations in terrestrial water storage driven by these seasonal cycles. This demonstrates the potential of clock-based geodesy to enhance our understanding of the Earth's water cycle in complex and dynamic systems like the Amazon.

3.6 Case C: Greenland

Greenland, home to the world's second-largest ice sheet after Antarctica, is undergoing significant ice mass loss due to climate change. Surface melting and iceberg calving, especially along its coastal boundaries, have contributed to a steady decline in ice mass over recent decades (Zwally et al., 2002; Landerer, 2022). These changes are primarily driven by increasing temperatures and the interplay of atmospheric and oceanic dynamics, leading to a profound impact on the global sea level.

Using high-performance optical clocks, this study explores the potential of detecting these ongoing ice mass losses and the associated elastic land uplift. The simulated observations of effective potential variations, δU, align with the methodology employed in the prior test cases. To capture the spatial and temporal dynamics of ice loss, GNSS stations at four strategically distant locations across Greenland were selected as clock sites (figure 3.10). These stations provide insight into the regional variations in mass redistribution and their effect on the Earth's gravity field.

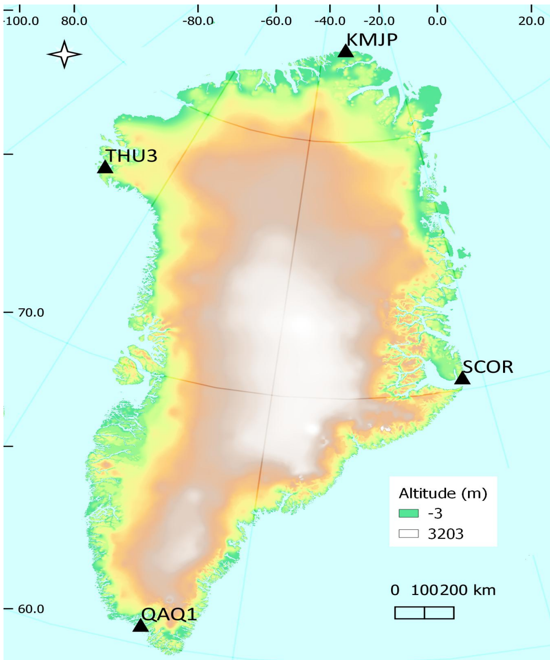

Figure 3.10: Simulated clock sites considered in Greenland

Satellite gravimetry missions, such as GRACE and its successor GRACE Follow-On, have provided pivotal data in quantifying Greenland's ice mass loss. According to Landerer (2022), the Greenland ice sheet lost approximately 280 gigatons of ice annually between 2002 and 2020, which corresponds to a global sea level rise of about 0.8 mm per year. The redistribution of this mass leads to changes in Earth's gravity potential, which can be observed as linear trends in clock-based measurements. In the case of Greenland, the elastic land uplift observed is primarily due to current ice mass loss, as the region was not heavily affected by GIA from the last glacial maximum compared to regions like Fennoscandia or North America. This provides a complementary and independent tool to traditional geodetic techniques, such as satellite altimetry and gravimetry, for understanding the implications of Greenland's ice mass loss on global and regional scales.

3.6.1 Simulation of Present-day Ice Mass Loss as Clock Observation

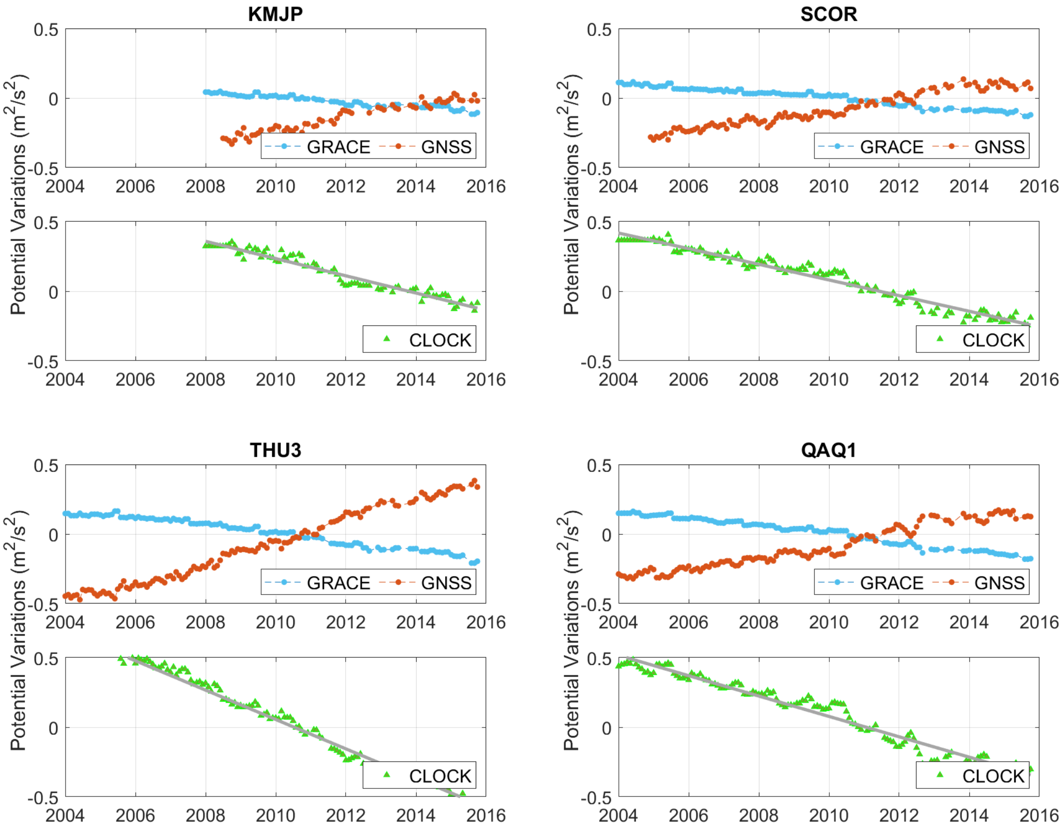

Figure 3.11: Linear potential variations over Greenland at sites KMJP, SCOR, THU3 and QAQ1. The upper panels show the variations separately derived from GRACE and GNSS. The lower panels show the combined effect of height changes (GNSS) and mass changes (GRACE) as it could be observed by clocks (CLOCK), with the fitted linear signal in gray.

The simulated linear potential variations at the four GNSS locations—KMJP, SCOR, THU3, and QAQ1—highlight the sensitivity of clock observations to ice mass loss in Greenland. These potential variations, shown in figure 3.11, reflect the long-term trend of effective potential changes resulting from ice mass loss between 2004 and 2015. The magnitude of these variations, reaching up to 1 m^2/s^2, is well within the sensitivity range of high-performance clocks, making these signals detectable with high accuracy. As the GNSS and GRACE time series differ in coverage and may contain data gaps, the combined clock signal is constructed by filling these gaps using nearest-neighbour interpolation to enable linear fitting.

The spatial variability of the ice mass loss is evident, with higher rates of potential changes in the western and southern parts of Greenland. This observation agrees with the known dynamics of the Greenland Ice Sheet, where significant melting and ice discharge occur along the island's periphery. The THU3 site, located in a region experiencing pronounced mass loss, exhibits the highest linear trend in potential variation, quantified at 0.11 m^2/s^2 per year. This emphasizes the capability of clock networks to detect and monitor regional differences in ice mass loss, providing a novel tool to complement satellite gravimetry and other geodetic methods.

3.7 Case D: Fennoscandia

Fennoscandia, the region that includes Sweden, Finland, Norway, and parts of Russia, has undergone significant post-glacial rebound, commonly referred to as GIA. This process began at the end of the last ice age and the corresponding deglaciation which was completed about 10,000 years ago and continues today as the Earth's mantle slowly adjusts to the loss of the vast ice sheets that once covered the region (Olsson et al., 2019). The present-day GIA signals are characterized by a secular gravity change and associated land uplift. The Earth's lithosphere, after being compressed by the weight of the ice, is slowly lifting back up viscoelastically as the mantle material flows and adjusts. The secular uplift in the central region of Fennoscandia is approximately 1 cm/year, with a corresponding secular gravity change of about -20 nm/s^2, as reported by Ekman (1996); Vestøl et al. (2019). This ongoing process plays a key role in the region's geoid dynamics, leading to observable changes that can be monitored with geodetic techniques.

3.7.1 Simulation of GIA Signals as Clock Observations

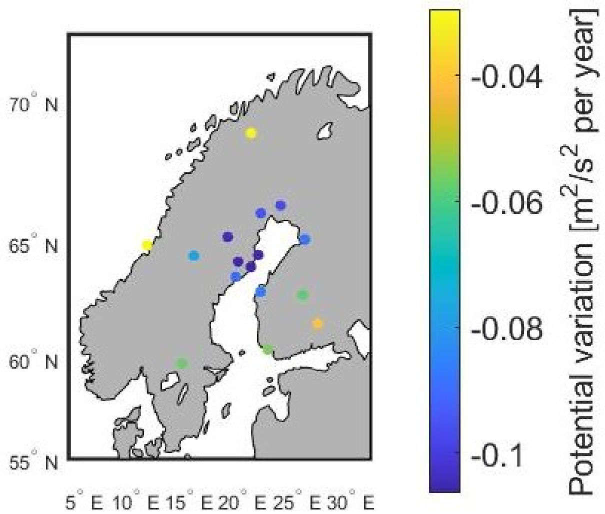

Figure 3.12: Simulated GIA signal over Fennoscandia in terms of effective potential variation per year

To simulate the GIA signals as observed by clock measurements, the methodology applied in previous test cases is followed. This includes simulating the linear potential variations due to GIA at 16 clock sites across Fennoscandia (figure 3.12). The sites closest to the uplift center experience a higher rate of potential variations, with values of 0.11 m^2/s^2 per year. However, as the distance from the uplift center increases, the magnitude of these variations decreases.

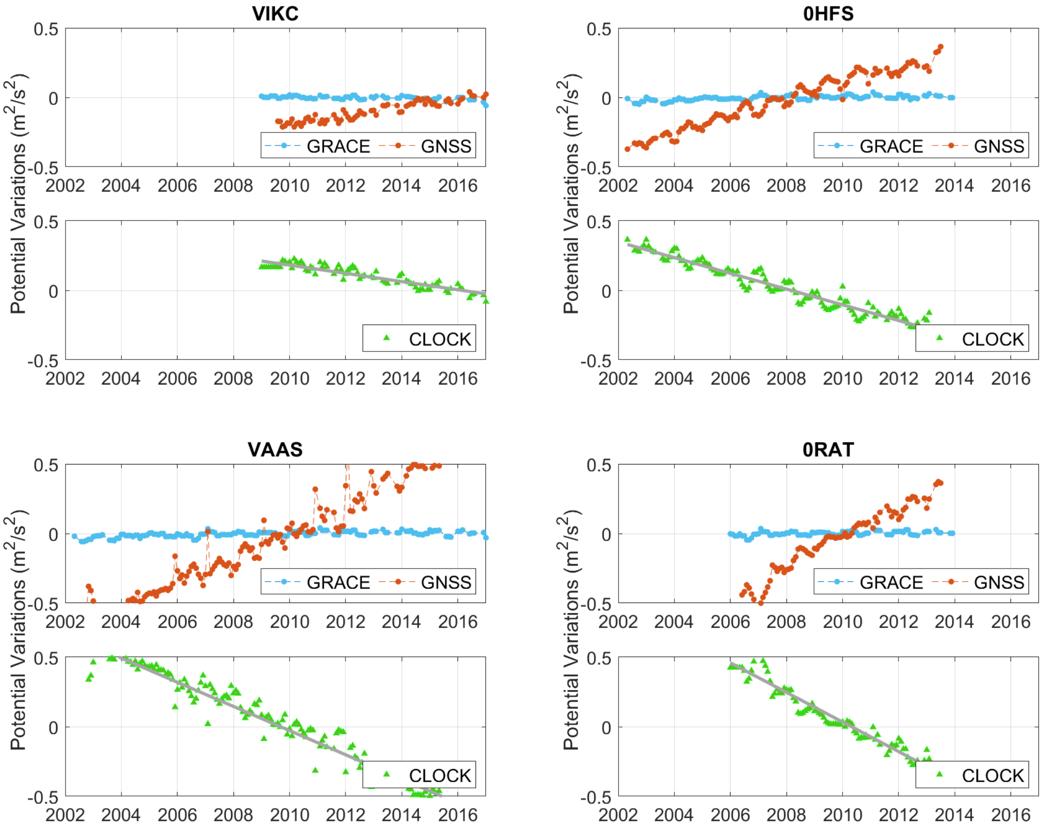

Figure 3.13: Linear potential variations in Fennoscandia at the sites VIKC, VAAS, 0RAT and 0HFS dominated by vertical deformation. The upper panels show the variations separately derived from GRACE and GNSS. The lower panels show the combined effect of height changes (GNSS) and mass changes (GRACE) as it could be observed by clocks (CLOCK), with the fitted linear signal in gray.

The clock observations simulate the secular trends in effective potential variations over a time span from 2002 to 2016, as shown in figure 3.13. However, it is important to note that, while vertical land uplift is the dominant signal in this region, the mass change contribution to the potential variations is relatively minor. Thus, the clock measurements in Fennoscandia provide a strong signal related to the vertical uplift but offer limited additional information compared to GNSS measurements. The secular geoid change in the Fennoscandian uplift centre is in the order of 0.4 mm/year, as per the ICE6G-D model (Peltier et al., 2018), which is beyond the sensitivity of current clock technology with fractional frequency uncertainties of 10^{-18}($\approx$ 1 cm).

While clock networks are capable of measuring changes in effective potential variations, the limited contribution of mass change to the observed signal in Fennoscandia makes GNSS a more comfortable tool for observing the vertical uplift associated with GIA. Clocks, therefore, may not provide significant additional insights beyond what is already achievable with GNSS measurements in this particular context.

3.8 Case E: Japan - Tōhoku Earthquake

The 2011 Tōhoku earthquake, with a moment magnitude (Mw) of 9.0, stands as one of the most significant seismic events of the 21st century (Imakiire and Koarai, 2012). It occurred along the Japan trench, a subduction zone where the Pacific plate is subducting beneath the North American plate. This tectonic interaction caused massive ground subsidence along the eastern coastline of Japan and a significant uplift of the seafloor near the trench, which triggered a devastating tsunami (Shibahara, 2011).

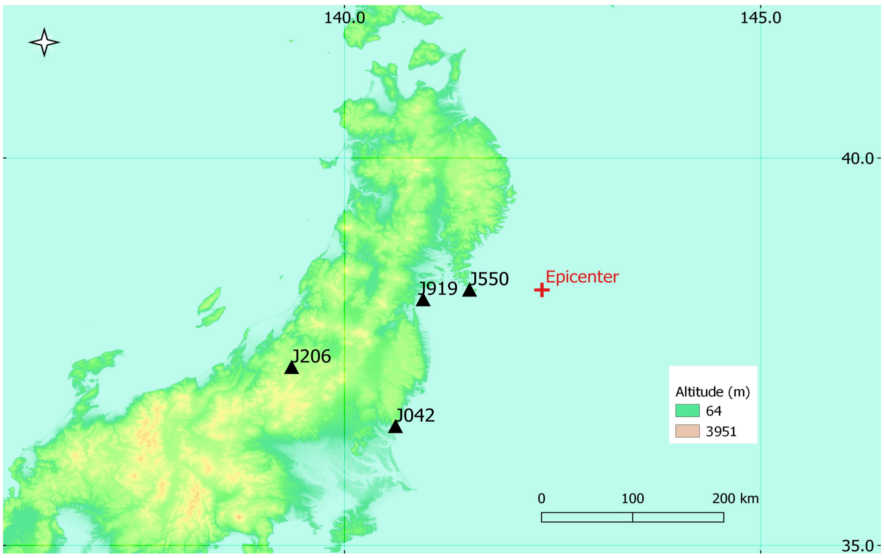

Figure 3.14: Simulated clock sites in Japan with the epicentre of Tohoku earthquake 2011.

The earthquake rupture zone extended over 500 km, with slip distributions reaching over 40 meters near the trench axis. In the region near the trench, the sea floor uplifts as the overriding North American plate releases from a downward pull of the subducting Pacific plate and rebounds upward. This causes the coastal areas on the mainland to experience ground subsidence (Imakiire and Kobayashi, 2011). The seafloor uplift near the plate boundary displaced large volumes of water, generating tsunami waves that inundated large areas of Japan's coast and impacted regions as far as the Indian ocean. GNSS signals show immediate vertical subsidence corresponding to the coseismic rupture, with significant downward displacement recorded along Japan's eastern coastline.

3.8.1 Co-seismic and Post-seismic Processes

Beyond the immediate co-seismic effects of the 2011 Tōhoku earthquake, the region has experienced several post-seismic processes that have continued to shape the Earth's crust and contribute to ongoing seismic activity (Ozawa et al., 2012). One of the most significant post-seismic processes is afterslip, which refers to the continued movement along the fault plane following the main rupture (Marone et al., 1991). Afterslip is a relatively slow but persistent phenomenon, where the fault gradually continues to slip after the main earthquake event. In the case of the Tōhoku earthquake, the afterslip was particularly notable along the shallow parts of the fault (Ozawa et al., 2011). This ongoing deformation redistributes stress along the fault, contributing to further adjustments in the crust.

Another critical post-seismic process in the aftermath of the Tōhoku earthquake is viscoelastic relaxation in the Earth's mantle (Sun et al., 2014). This process occurs as the Earth's mantle adjusts to the stress redistributed by the earthquake. Following the sudden release of strain during the earthquake, the mantle slowly relaxes to accommodate the new state of stress. This results in continued ground movement, albeit at a much slower rate compared to afterslip. For Tōhoku, the viscoelastic response was marked by ongoing uplift and subsidence, which was most noticeable in the years immediately following the earthquake. Researchers have used data from GNSS and satellite altimetry to track these gradual shifts in the crust, showing that the region continued to experience slow but detectable land movement due to the Earth's viscoelastic response.

Additionally, changes in crustal porosity and the migration of fluids within the Earth's crust played a role in post-seismic deformation (Unjoh et al., 2012). In the case of the Tōhoku earthquake, the rupture likely triggered changes in the pore pressure within the fault zone and surrounding regions, as well as the movement of fluids along fault planes and fractures. These changes can affect the local stress regime, contributing to further seismicity and crustal deformation. For example, the introduction of fluids into fault zones can reduce friction along the fault, potentially leading to increased afterslip or even triggering additional seismic events. Fluid migration may also play a role in the long-term deformation of the crust, particularly in the vicinity of the subduction zone, where water from the oceanic plate may be released into the mantle.

The earthquake and subsequent phenomena provide an excellent case study for using high-precision atomic clocks to detect effective potential variations caused by seismic activity. Clocks could help identify stress redistribution before seismic events and monitor co-seismic and post-seismic deformations, offering potential advancements in earthquake prediction and hazard assessment.

3.8.2 Simulation of Seismic Signals as Clock Observations

To better analyze the potential variations associated with the 2011 Tōhoku earthquake, GNSS daily observations were processed by calculating the mean values up to February 2011 (prior to the earthquake). This mean was then subtracted from

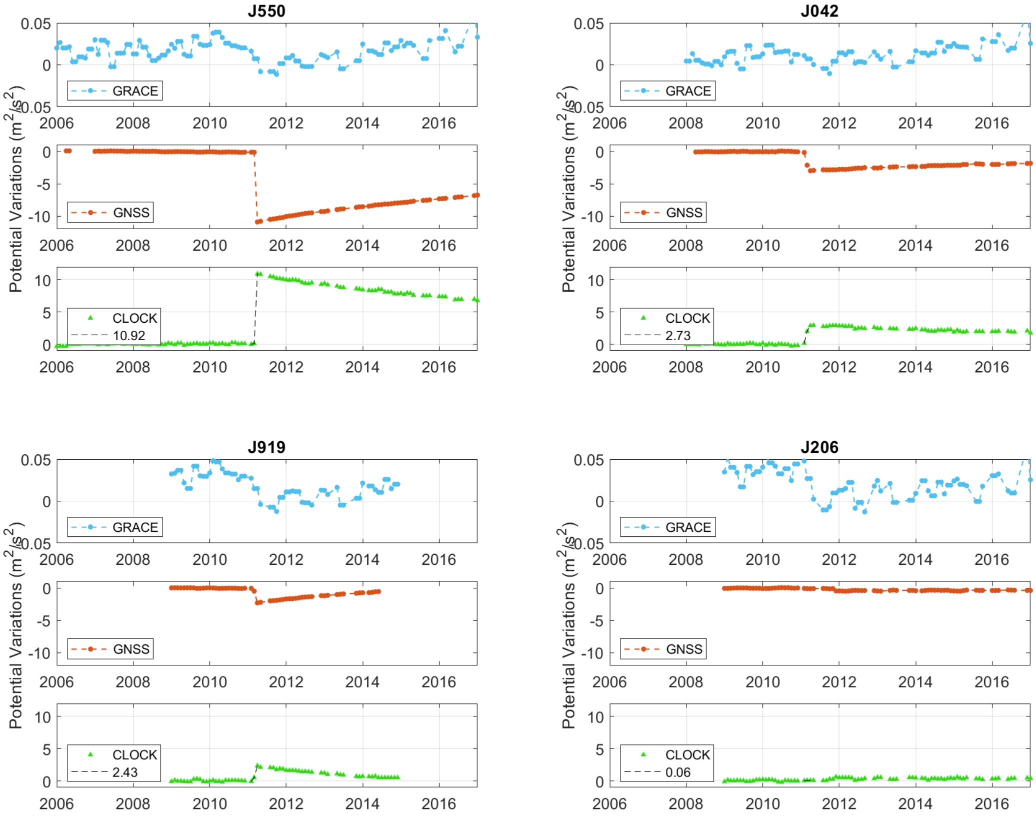

Figure 3.15: Effective potential variations in Japan at the sites J550, J042, J919 and J206 showcasing the pre-seismic, co-seismic and post-seismic effects related to the Tohoku earthquake in 2011. The upper panels show the variations separately derived from GRACE and GNSS. The lower panels show the combined effect of height changes (GNSS) and mass changes (GRACE) as it could be observed by clocks (CLOCK), with the mainshock's effective potential variation indicated.

the daily GNSS observations to isolate the anomalies. Subsequently, monthly averages of these processed observations were taken to provide a clearer representation of the potential variations before and after the earthquake. This methodology ensures that the potential variations caused by the earthquake and the subsequent postseismic processes are highlighted more effectively and allow a more precise comparison of the potential changes derived from GNSS data with GRACE observations, showcasing the consistent trends in mass redistribution and vertical displacement using equation (2.22).

Mainland subsidence during the 2011 Tōhoku earthquake can be interpreted as a local mass deficit from a geodetic perspective. This phenomenon occurs because the subsidence represents a downward movement of the land, reducing the gravitational potential at the surface due to the redistribution of mass from the crust and mantle. The simulated potential variations from GRACE and GNSS indeed show a consistent temporal pattern in response to the Tōhoku earthquake (figure 3.15). The effective potential variation associated with the mainshock of the 2011 Tōhoku earthquake is calculated as the difference between the simulated clock-derived gravitational potential values for April and February 2011. This approach is based on the fact that the earthquake occurred on March 11, making February a suitable pre-event baseline. The computed potential variations reflect the coseismic effects, including rapid mass redistribution and vertical displacement due to the earthquake.

The magnitude of these potential variations differs across sites, primarily influenced by their distances from the earthquake's epicenter. Sites closer to the epicenter experience larger variations due to the intense ground displacement and mass anomaly induced by the rupture, while more distant sites observe smaller changes. The spatial distribution of these variations can be understood from the figures 3.14 and 3.15.

3.8.3 Earthquake Forecasting

To investigate the potential of earthquake prediction using clock observations, the focus is on detecting precursor signals, such as those associated with Slow Slip Events (SSEs) that typically occur along subduction zones before major earthquakes. Utilizing ITS-GRACE 2018 daily gravity field solutions up to degree 40, the approach involves deriving daily potential variations by subtracting the EIGEN-6C4 static field, as it was done for the monthly GRACE solutions.

Daily clock observations were synthesized by integrating potential variations from daily GRACE and GNSS data using equation (2.22), see figure 3.16. While GNSS failed to show any precursor signals, GRACE data revealed small changes in mass distribution beginning approximately one month before the earthquake, in the order of 10^{-19} as observed from the figure. These subtle changes align with the hypothesis that early mass redistribution could be linked to SSEs preceding seismic events.

The GRACE solutions, constrained to degree 40, inherently limit spatial resolution due to their long wavelength sensitivity. Using the relationship $\lambda = \frac{2\pi R}{L}$, where R is Earth's radius and $L = 40$, the spatial resolution is about 1000 km (roughly $10°$ on the surface). This constraint causes the derived potential variations to be nearly uniform in a $10°$ region, impeding the ability to resolve station-specific daily variations.

Geometric changes dominate potential changes when considering tectonic applications. The complementarity of GRACE and GNSS in capturing both mass anomalies and vertical displacements provides a holistic view of the co-seismic and post-seismic evolution, demonstrating the potential for clocks to enhance our understanding of these processes through high-precision potential measurements. Hence, future high-performance atomic clocks with fractional frequency uncertainties of the order of 10^{-19} offer a promising potential for forecasting geophysical phenomena such as earthquakes or volcanic eruptions.

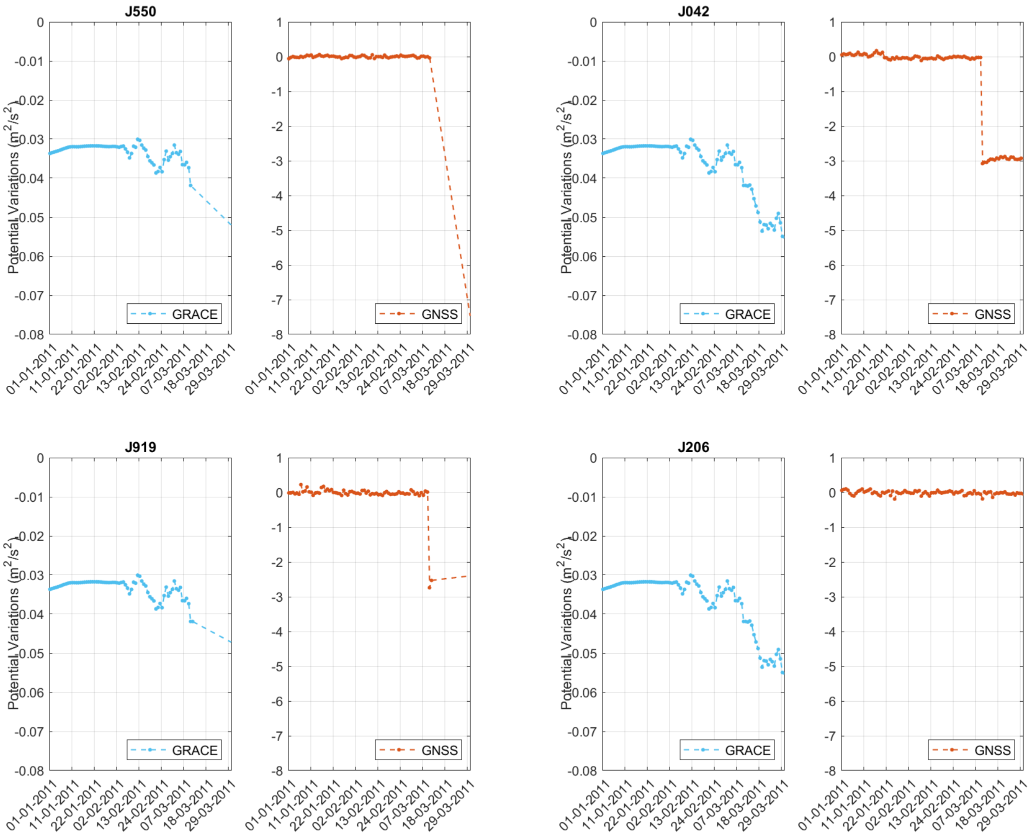

Figure 3.16: Daily potential variations separately derived from GRACE and GNSS in Japan at the sites J550, J042, J919 and J206 01.01.2011 till 30.03.2011.

Chapter Summary

In the future, clock observations will provide a powerful means of detecting potential variations resulting from mass changes and vertical deformations at specific sites. Five case studies have demonstrated the capability of terrestrial clock networks as a modern and complementary tool for capturing different time-variable signals arising from mass redistribution processes. Effective potential variations in the range of $0.1\,\mathrm{m^2/s^2}$ to $1\,\mathrm{m^2/s^2}$ can be reliably measured by high-performance clocks with fractional frequency uncertainties of 10^{-18} ($0.1\,\mathrm{m^2/s^2}$). Relativistic geodesy enables point-specific potential measurements over short timescales (hours to days) and provides an independent method of validating gravity variations observed via satellite geodesy techniques.

The simulations of time-variable signals included hydrologically driven annual variations in the Himalayas and the Amazon, linear trends caused by present-day ice mass loss in Greenland, post-glacial rebound effects in Fennoscandia and seismic potential variations from the 2011 Tohoku earthquake in Japan. GRACE and GNSS data formed the basis of these simulations, offering insight into distinct geophysical processes. The reference clock for comparisons was assumed to be at a combination of a ground-based and a space-based (known satellite orbit) clocks, with links providing uncertainties better than 10^{-18}.

Looking ahead, advancements in atomic clock technology and optical links with uncertainties better than 10^{-18} may revolutionize geodetic techniques, allowing for innovative Earth system monitoring. This synergy between clock-based relativistic geodesy and existing geodetic methods positions clocks as indispensable tools for understanding dynamic Earth processes.

4 Application II - Realization of Clock-based Global Height System

4.1 Height System Unification to a Pre-defined Datum

The unification of height systems across different continents in our simulation uses the integration of classical levelling and gravimetric data with simulated clock observations that capture gravity potential differences. For this study, we focus on two regions: Europe and Brazil, each representing different vertical reference systems tied to distinct datums. In Europe, the a priori system for our simulation is the European Vertical Reference Network (EUVN2000), linked to the NAP (Normaal Amsterdams Peil) datum, while in Brazil, the reference is based on the Imbituba tide gauge, as part of the Brazilian vertical datum. Clock observations are simulated as gravity potential differences, derived either directly from potential values C_p or from normal heights $H^N = \frac{C_p}{\overline{\gamma}}$, where $\overline{\gamma}$ is the mean normal gravity along the plumb line (Jekeli, 2000). The study models regional height systems (LHS) in both regions, introducing transformations and error terms to achieve unification to their respective reference datums.

4.1.1 Tidal Corrections and Impact on Clock Observations

The tidal effects $\Delta C_i(t)$ at a clock site are represented as variations in the geopotential number C, calculated on an hourly basis. Daily averages of the tidal effects are computed from the modelled hourly solutions to align with the typical averaging period of clock observations.

To account for potential model inaccuracies, the tidal potential variations were estimated using alternative tidal potential catalogue and ocean tide models, such as Tamura87 (Tamura et al., 1991) and FES2004 (Lyard et al., 2006). The resulting model differences (δTE_i) were treated as additional uncertainties and combined with the modelled tidal potential values,

$$TE_i = \Delta C_i(t) + \delta TE_i \tag{4.1}$$

where TE_i represents the total tidal effect at a given site, including model errors.

The tidal potential variations depend on geographic latitude and exhibit significant hourly changes. The variations for SET, OTL, and POL combined are typically within $[-4, 4]$ $\mathrm{m}^2/\mathrm{s}^2$ on an hourly basis, reducing to $[-0.4, 0.4]$ $\mathrm{m}^2/\mathrm{s}^2$ when averaged daily. Similarly, model errors (δTE_i) reduce from ≈ 0.1 $\mathrm{m}^2/\mathrm{s}^2$

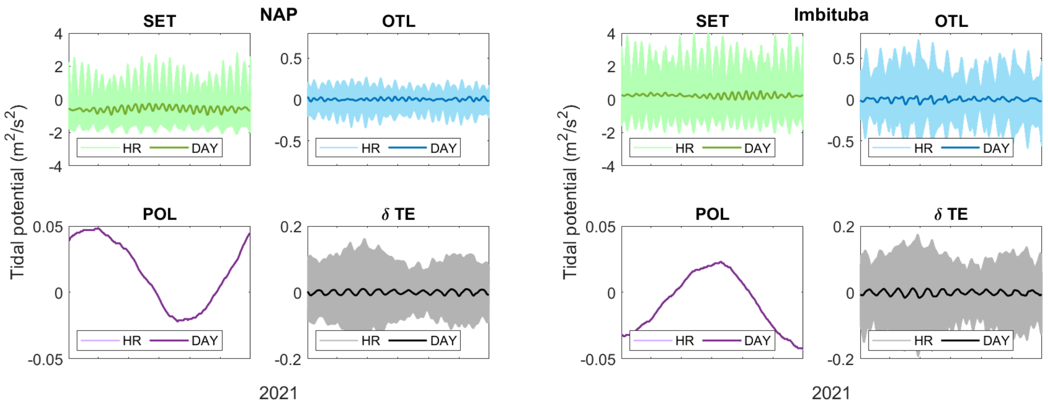

Figure 4.1: Hourly and daily potential variations due to solid earth tide (SET), ocean load tide (OTL) and pole tide (POL) with corresponding model error (δTE) at NAP, datum point of the European system (left) and the Imbituba, the datum point of Brazilian system (right).

(hourly) to ≈ 0.02 m^2/s^2 (daily averages). Hence, this difference allows for an efficient handling of tidal effects based on the clock observation averaging time. Hourly averaged observations require precise corrections, while daily or higher averages benefit from the natural cancellation of tidal effects below the clock uncertainty of 10^{-18}. This approach ensures that clock observations are as free as possible from tidal effects, matching the precision requirements of 10^{-18} clocks. Tidal potential variations generated at the datum point of the European system (NAP) and Brazilian system (Imbituba) are shown in figure 4.1.

For short-baseline clock comparisons, tidal effects tend to cancel out due to the similar effects at the two locations. However, for long baselines, where the tidal effects vary significantly between the sites, precise corrections are essential to achieve the desired accuracy. By addressing tidal effects comprehensively, we enable high-precision geodetic applications such as height system unification.

4.1.2 Case A: European Height System - Relate to NAP

Data Preparation

The European Vertical Reference Network (EUVN), used as the a priori unified system, consists of 202 levelling points distributed across Europe. The EUVN system is based on the European Vertical Reference Frame (EVRF), which provides high-accuracy normal heights referenced to the NAP datum (Ihde et al., 2000). This network ensures the integration of the European height systems with consistent and precise normal height definitions, enabling robust geodetic applications across the continent. To facilitate the simulation process, these levelling points are divided into four local height systems (LHS): G1, G2, G3, and G4 (figure 4.2). This classification is based on administrative boundaries and proximity to prominent tide gauges at Marseille, Newlyn, NAP, and Genova.

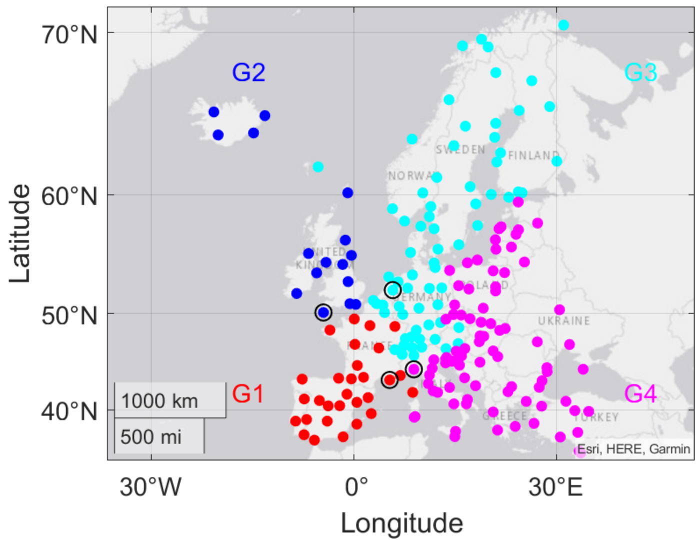

Figure 4.2: Classified EUVN height system. The generated 4 LHSs G1, G2, G3, and G4 are indicated in different colours. The tide gauge locations for each LHS are indicated by a black circle.

Simulation of Local Height Observation

The local height systems are created by introducing assumed errors like offsets and tilts into the a priori normal heights from the EUVN system, expressed in terms of geopotential numbers (C_p). To account for more realistic and complex scenarios, an extended measurement model was developed, incorporating five error parameters (a^L, b^L, OT^L, t^L, m^L) for each LHS, illustrated in figure 4.3 (left). These parameters represent offsets, tilts, systematic distortions, and elevation-dependent effects, making the model suitable for evaluating diverse error sources in each local system. The local geopotential number at a point, C_i^L based on equation (2.27), is expressed as the sum of the unified geopotential number C_i^U and the contributions from systematic tilts, elevation effects, offsets, and random noise as

$$C_i^L = C_i^U + (a^L \Delta X_i + b^L \Delta Y_i + t^L \Delta S_i) \cdot g + m^L C_i^U / E + OT^L + RN. \tag{4.2}$$

The systematic tilts a^L, b^L and t^L are associated with latitude (ΔX_i), longitude (ΔY_i) distances and distance from the tide gauge (ΔS_i) in terms of cm/degrees respectively. The elevation-dependent tilt m^L is scaled by the unified height potential C_i^U and normalized with a constant $E = 500$ m. If no points in an LHS exceed 500 m in elevation, the m^L contribution is neglected. Random noise (RN) is modelled as Gaussian noise with a standard deviation of 0.1 $\mathrm{m}^2/\mathrm{s}^2$ (approximately 1 cm height). Hence, a total of 18 unknowns (table 4.1) are defined here. The datum of G3, linked to NAP, is fixed with $OT^3 = 0$, and $m^2 = 0$ for G2 as it lacks high-elevation points (> 500 m).

Table 4.1: Assumed true errors in the four LHSs of the European system before unification

Error parameter	G1	G2	G3	G4
a^L (cm/degree)	3	-2	1.5	-3
b^L (cm/degree)	2	3	-1.5	-2
t^L (cm/degree)	-2	3.5	3	-3
m^L (cm)	1.5	0	2	1.5
OT^L/g (cm)	-18	25	0	8

Simulation of Clock Observations

As outlined in equation (2.28)

$$\Delta W_{ij} = -(C_i^U - C_j^U) - (TE_i - TE_j) + PD_{ij} + CE_i + CE_j, \tag{4.3}$$

clock observations ΔW are affected by uncertainties originating from three main sources: the intrinsic uncertainties of the clocks (CE), tidal effects (TE), and those arising from the process of clock comparison (PD).

The clock sites are strategically placed within each LHS, and clock observations are simulated by assuming that all clocks are interconnected, providing a dense network of observations. For any two clocks, only one observation is simulated, meaning there are no repeated observations. If a total of n clocks are interconnected, the number of observations is given by $\binom{n}{2}$, representing the total number of clock pair combinations. We assumed 5 clocks per local height system (LHS), totaling 20 clocks across 4 LHS. These are interconnected via fiber links with 10^{-19} uncertainty, yielding 190 clock comparisons ($^{20}C_2$) across the network. This setup ensures sufficient redundancy and sensitivity to estimate all error parameters accurately.

Clock-based Adjustment

The European height unification process was carried out by simulating clock-based adjustments. Multiple reunification scenarios were studied, each incorporating different combinations of error parameters to explore the impact of various effects on the unification accuracy.

The unification accuracy was assessed in terms of two measures, adjusted error and assumed "true" error. The adjusted error is defined as the difference between the reunified heights and the a priori heights from the EUVN2000 system. This measure quantifies how closely the adjustment aligns with the reference system. The assumed true error, on the other hand, is the difference between the simulated local heights (including offsets and tilts) and the a priori heights. Comparing these metrics allows for evaluating the effectiveness of the clock-based adjustment process in determining the introduced errors.

The primary objective of the simulations was to identify the optimal clock config-

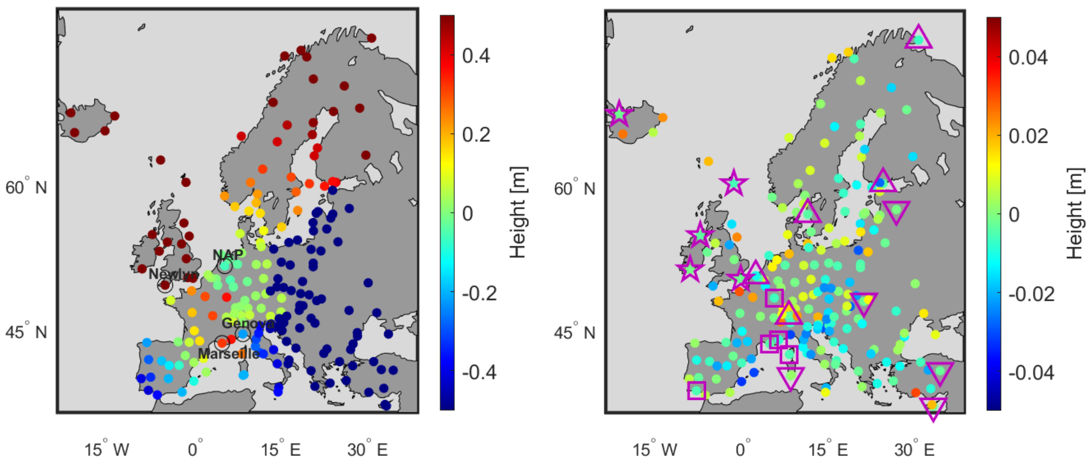

Figure 4.3: True error before unification (left) and the residual errors after unification (right) obtained with the extended model. Different symbols in the right image represent the clock sites in each LHS. The error reduced to $\approx \pm$ 1 cm after the clock-based unification.

Table 4.2: RMS error of each LHS after unification

LHS	G1	G2	G3	G4
RMS Error (cm)	1.46	1.37	1.09	1.33

uration—specifically, the number and spatial distribution of clocks—that yields the best unification accuracy. Various configurations were tested, and the results demonstrated that achieving centimetre-level accuracy in height unification is feasible with strategically distributed clock networks. The configuration presented here, which achieves an accuracy of $\approx$ 1 cm, utilized a carefully selected network of clocks distributed across the LHSs (figure 4.3 (right)). These clocks were positioned to maximize coverage and minimize the impact of the errors in each LHS. The overall unification accuracy for each LHS is in the order of 1 cm (table 4.2). The optimal clock network as demonstrated in figure 4.4, ensures sufficient observational redundancy and reliable parameter estimation.

By leveraging the precision of optical clocks and their ability to detect gravity potential differences, the simulations showcase the potential of clock-based adjustments to significantly enhance the accuracy of height system unification. The study underlines the importance of optimizing clock placement and network design to achieve consistent and reliable results across large-scale geodetic networks.

Clock Network Configuration

The spatial distribution of the clocks is critical for accurately estimating the error parameters in each LHS. Specifically, the estimation of systematic tilts (a^L, b^L) and offsets (OT^L) depends strongly on the strategic placement of the clocks in each LHS.

- Tilt Estimation (a^L, b^L):

  To estimate the tilt values accurately, clocks need to be placed at locations where the tilt effects are at their maximum and minimum. Since tilts ($a^L \Delta X$ and $b^L \Delta Y$) are direction-dependent, their extreme values typically occur at the most northerly, southerly, easterly and westerly points of the LHS. Thus, placing clocks at these most extreme points ensures the best sensitivity to tilt variations.

- Offset Estimation (OT^L):

  Offsets are best estimated at locations where the tilt effect is minimal, ensuring the clock observations are unaffected by systematic gradients.

- Site-Specific Parameters (t^L, m^L):

  A clock near the tide gauge site is essential for accurately estimating the tide gauge-related parameter t^L. Similarly, placing a clock at or near the highest elevation point in the LHS, where the elevation-dependent parameter m^L reaches its maximum, allows for precise estimation of m^L.

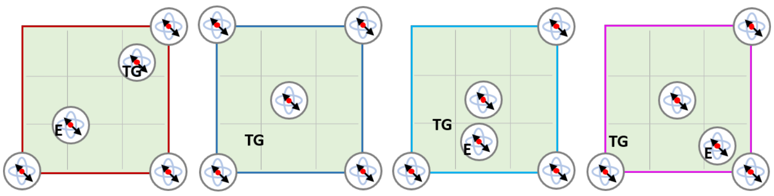

Figure 4.4: Spatial distribution of 5 clocks associated with as used in each LHS – G1, G2, G3 and G4. The preferred clock positions are at the most northerly, southerly, easterly and westerly points, reference tide gauge (TG), maximum elevated point (E) and LHS centre.

For the unification process, a network of five clocks with 10^{-18}-level accuracy was assumed for each LHS (figure 4.4). The clocks were distributed as follows:

1. At the most extreme points and central point of the LHS to capture maximum and minimum tilt effects.

2. One clock positioned randomly near the highest elevation point to improve the estimation of m^L.

Testing and Selection of Optimal Configuration: Before finalizing the above configuration, extensive tests were conducted with different numbers and spatial arrangements of the clocks. The best configuration, shown in figure 4.4, was selected based on its ability to minimize the standard deviations of all error parameters from the covariance matrix after unification using different network configurations (figure 4.5 (left)). The corresponding values associated with a random distribution are also provided (figure 4.5 (right)) for comparison. This spatial arrangement ensures that the unification process achieves high accuracy with minimal uncertainty. The least values obtained with the optimal configuration:

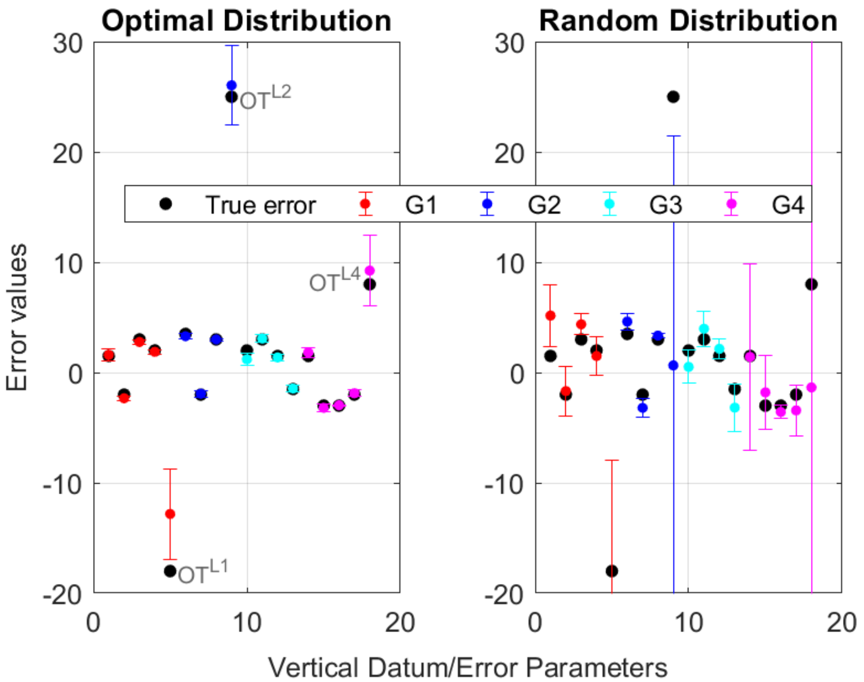

Figure 4.5: Estimated error parameters in an extended model with a total of 18 unknowns with their standard deviations for optimal (left) and random (right) distribution. The assumed true error values are provided for reference. The units are different for tilts (cm/degree) and offsets (cm).

- OT^L, m^{L1}: SD of $\approx$ 5 cm for OT^L/g and for m^L, $\approx$ 1 cm.

- Tilts (a^L, b^L, t^L): SD values below $\approx$ 1 cm/degree.

The correlation matrix is computed for the optimal setup to understand the relatively large standard deviation of OT^L (Figure 4.6). It is observed that OT^L shows medium correlation ($\approx$ 0.5) with other offsets and similar correlation with all error parameters of G3 (unifying datum, $OT^{L3} = 0$), the only parameter that is correlated with other error parameters between the LHS. Within an LHS, OT^L is moderately correlated with b^L and t^L. The other correlation within the LHS is between tilts.

Transportable Clocks for Unification: The proposed approach does not require fixed laboratory clocks, making it practical and flexible. Campaigns with transportable optical clocks can achieve the same results, enabling the deployment of high-precision clocks to strategic locations that are linked as needed for the unification process. This adaptability significantly reduces logistical constraints, facilitating clock-based unification even in regions with limited infrastructure.

This carefully designed clock configuration, combined with the extended model, provides a robust framework for height system unification with centimetre-level accuracy. It highlights the importance of strategic planning in clock placement and the role of advanced transportable clock technology in modern geodesy.

[1]The unit of OT^L is m^2/s^2 whereas OT^L/g is cm.

	m^{L1}	t^{L1}	a^{L1}	b^{L1}	OT^{L1}	t^{L2}	a^{L2}	b^{L2}	OT^{L2}	m^{L3}	t^{L3}	a^{L3}	b^{L3}	m^{L4}	t^{L4}	a^{L4}	b^{L4}	OT^{L4}
m^{L1}	1	0.178	-0.034	0.016	**-0.122**	0	0	0	0	0	0	0	0	0	0	0	0	0
t^{L1}		1	-0.152	0.809	-0.72	0	0	0	0	0	0	0	0	0	0	0	0	0
a^{L1}			1	-0.525	**0.079**	0	0	0	0	0	0	0	0	0	0	0	0	0
b^{L1}				1	-0.671	0	0	0	0	0	0	0	0	0	0	0	0	0
OT^{L1}					1	0	0	0	0.462	0.366	-0.563	0.374	0.516	0	0	0	0	0.525
t^{L2}						1	-0.91	0.601	-0.473	0	0	0	0	0	0	0	0	0
a^{L2}							1	-0.326	**0.256**	0	0	0	0	0	0	0	0	0
b^{L2}								1	-0.648	0	0	0	0	0	0	0	0	0
OT^{L2}									1	0.418	-0.642	0.427	0.588	0	0	0	0	0.599
m^{L3}										1	-0.483	0.851	0.097	0	0	0	0	0.474
t^{L3}											1	-0.63	-0.85	0	0	0	0	-0.729
a^{L3}												1	0.152	0	0	0	0	0.484
b^{L3}													1	0	0	0	0	0.668
m^{L4}														1	0.247	0.173	-0.317	**-0.141**
t^{L4}															1	-0.216	-0.983	-0.446
a^{L4}																1	0.205	**-0.083**
b^{L4}																	1	0.397
OT^{L4}																		1

Figure 4.6: Correlation matrix of estimated error parameters for the optimal setup. The correlation between different LHS is highlighted in green and yellow. Other major correlation within one LHS is provided in blue and red font.

Clocks with Different Frequency Uncertainties

To explore the robustness of clock-based height unification under varying conditions, an alternative scenario is considered where the LHSs are equipped with a mix of clocks with different accuracies. Here, specifically, each LHS contains two high-performance clocks with uncertainties of 10^{-18} and two less accurate clocks with uncertainties of 10^{-17}. This scenario reflects a more practical situation where not all regions have access to the most advanced clock technology.

The height observation equation (2.27) is applied in this scenario, incorporating three error terms in each LHS (a^L, b^L, OT^L). Other tilt terms (t^L, m^L) are set to zero for simplicity, as they are assumed negligible in this scenario.

Table 4.3: RMS error of each LHS after unification

LHS	G1	G2	G3	G4
RMS Error I (cm)	1.38	2.10	1.09	1.95
RMS Error II (cm)	2.13	3.05	4.07	3.13

The unification process is carried out using a weighted least-squares approach. The weights are assigned based on the clock uncertainties (10^{-18} or 10^{-17}), where the observations from more accurate clocks contribute more significantly to the solution. A network of four clocks in each LHS is assumed, with all clocks interconnected. The accuracy of the estimated error parameters (a^L, b^L, OT^L) strongly depends on the spatial distribution of the clocks, particularly the placement of the more accurate (10^{-18}) clocks. Offsets are estimated most accurately when the 10^{-18} clocks are placed at the lower left corner (LLC) and upper right corner

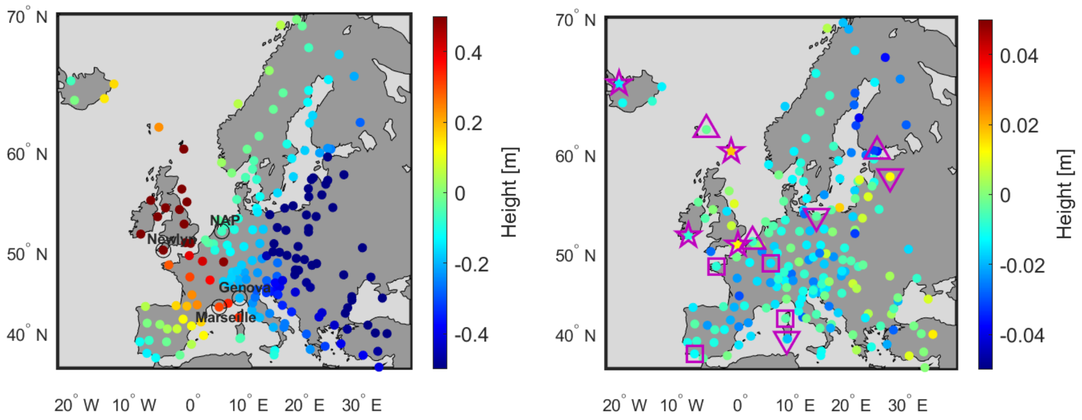

Figure 4.7: "True" error before unification (left) and residual error after unification (right) when clocks with different frequency uncertainties are used in each LHS with more accurate clocks (10^{-18}) placed at LLC (Lower Left Corner) and URC (Upper Right Corner). Different symbols in the right image represent the clock sites in each LHS. The error reduced to ≈ ± 1 cm after clock-based unification.

(URC) of each LHS. These locations minimize the impact of systematic tilts on the offset estimation, providing a clear signal for OT^L. Tilts are estimated effectively when the 10^{-18} clocks are positioned to maximize sensitivity to directional changes in the systematic slopes.

The "true" errors before unification and the adjusted errors after unification are shown in figure 4.7. Despite the presence of less accurate clocks (10^{-17}) in the network, the unification process achieves a high level of accuracy, with adjusted errors reduced to approximately 1 cm. This result demonstrates the feasibility of achieving high-accurate height unification even in scenarios with mixed clock uncertainties.

4.1.3 Case B: Brazilian Height System - Related to Imbituba

Data Preparation

The Brazilian levelling dataset, comprising 71,196 geopotential numbers, was received from the SIRGAS (Geocentric Reference System for the Americas) working group. This comprehensive dataset serves as the basis for simulating the unification process in Brazil. To ensure computational efficiency while maintaining representative coverage, the dataset was refined by defining grid sizes within each region, reducing it to 1,164 geopotential numbers. These points were subsequently classified into 10 LHS: H1 through H10, based on their proximity to selected tide gauge stations (figure 4.8).

Tide gauge data from the Permanent Service for Mean Sea Level (PSMSL)

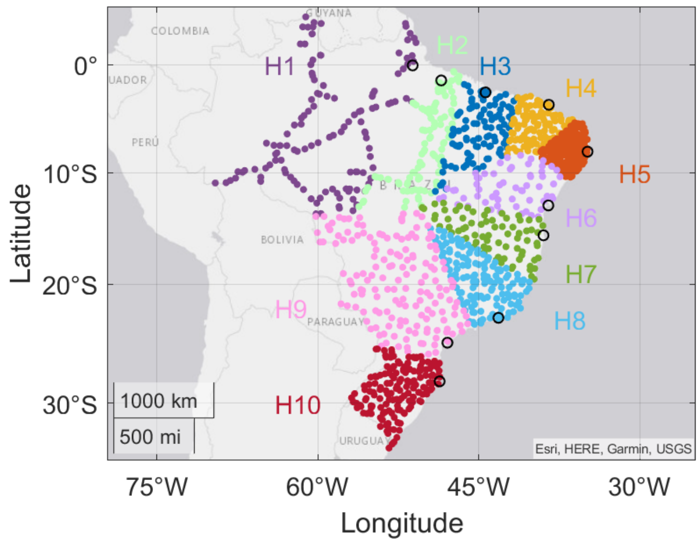

Figure 4.8: Classified Brazilian height system. The 10 generated LHSs: H1, H2, H3, H4, H5, H6, H7, H8, H9 and H10 are indicated in different colours. The tide-gauge locations for each LHS are indicated by black circles.

(PSMSL, 2023) were used to identify and group the levelling points. PSMSL provides a global database of tide gauge records essential for defining height system datums and analyzing sea-level variations. For this study, the tide gauge at Imbituba serves as the unifying datum for the reference system (H10), with its offset ($OT^{10} = 0$) fixed to zero. However, the reference system still includes tilt parameters (a^{10} and b^{10}) to account for possible regional inclinations. The remaining local height systems are created by introducing assumed offsets and tilts (a^L and b^L) into the geopotential numbers, simulating regional distortions relative to the unifying datum (table 4.4, figure 4.9).

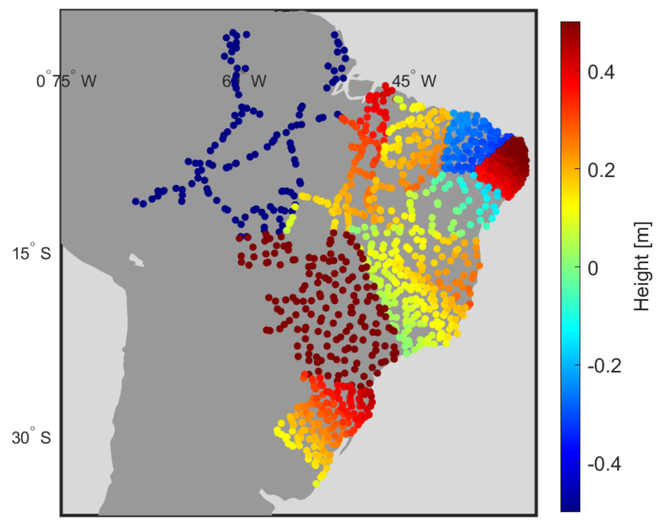

Figure 4.9: Simulated "true" errors before unification for the various classified local heights.

Table 4.4: Assumed true errors in the 10 LHSs of the Brazilian system before unification

Error parameters	H1	H2	H3	H4	H5	H6	H7	H8	H9	H10
a^L (cm/degree)	2	1.5	-2	1.5	3	2.5	2	2	3.5	3
b^L (cm/degree)	3	2	2	-1.5	2.5	-3	1.5	2.5	2	3
OT^L/g (cm)	-34	6	22	-28	30	26	15	-10	35	0

A network of four clocks is strategically distributed at the most extreme points of each LHS to simulate the clock observations. Reduced links between the clocks are considered to ensure observational redundancy for precise parameter estimation. The simulated clock observations include corrections for tidal effects as described in section 4.1.1. For this region, the height observation equation is applied using three error parameters (a^L, b^L, and OT^L) in each LHS, resulting in 29 unknown transformation parameters. This framework provides a robust methodology to assess the unification process under varying error scenarios while leveraging a minimal but strategically positioned clock network.

Modified Clock Links

In contrast to the configuration discussed in Wu et al. (2018) and section 4.1.2, where all clocks are fully linked, we propose a reduced-link configuration that significantly minimizes the number of links while maintaining high unification accuracy. This configuration utilizes one master clock in each LHS, strategically placed at the lower-left corner (LLC) of the LHS, and linked to the master clocks in all other LHSs. Meanwhile, the remaining local clocks in each LHS are only linked to each other internally. This approach drastically reduces the number of links required, ensuring efficiency without a substantial compromise in unification precision (figure 4.10).

Specifically, in this reduced-link configuration, with four clocks in each of the ten LHSs, the internal links in each LHS amount to 60 local connections $(10 \cdot \binom{4}{2})$. Additionally, there are 45 master links $(\binom{10}{2})$ that connect the master clocks between the LHSs, leading to a total of 105 clock observations. The local connections are assumed to use optical fiber links, ensuring high precision in each LHS, while the inter-LHS connections between master clocks are assumed to use free-space links, allowing for flexible and efficient long-distance connectivity.

This configuration represents a significant departure from the EUVN clock network discussed earlier, where all clocks were linked, resulting in a much larger number of observations. By reducing the connections such that only master clocks are linked between LHSs, the total number of clock observations is minimized while maintaining the robustness of the unification process. This strategy not only reduces the logistical complexity of setting up such a network but also optimizes resource allocation by leveraging free-space links for the master clocks and high-precision optical fiber links for the local clocks in LHSs. The reduced-link configuration demonstrates an effective balance between network efficiency

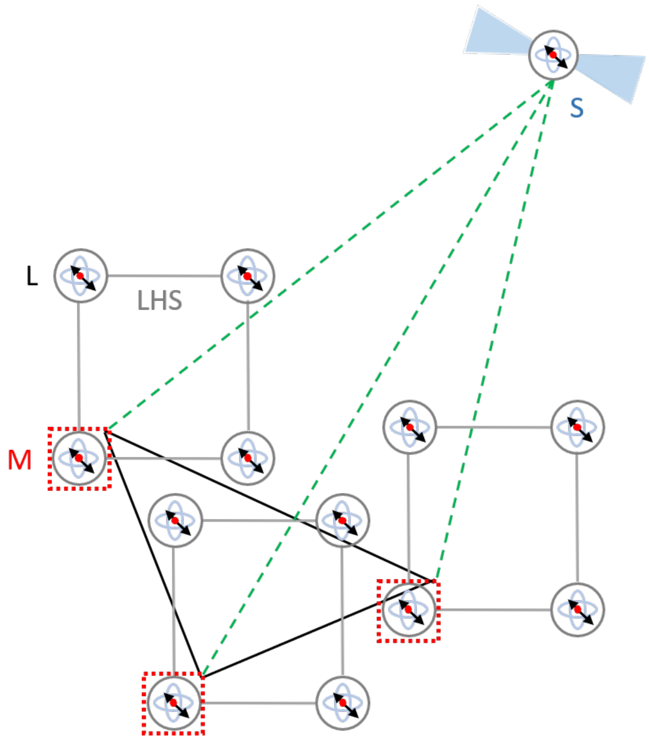

Figure 4.10: Configuration of clock distribution with master clocks (M) and local clocks (L) in each LHS. Local clock connections were assumed with fibre links in the LHS. Master clocks of each LHS can be connected via either optical fibre (black) or free-space links (green).

and unification accuracy, making it a practical approach for real-world implementations.

Clock-based Adjustment

The formulation of link uncertainty during clock comparisons, as detailed in section 2.3.5, plays a crucial role in the unification process, particularly when determining the accuracy of the clock network configuration. In our simulations, the connections between local clocks in each LHS are assumed to utilize high-precision optical fiber links. These fiber links offer an uncertainty in the order of 10^{-19}, ensuring that the dominant source of uncertainty in local connections arises from the inherent clock errors rather than the propagation delay. This assumption provides a robust foundation for minimizing errors in the LHS.

On the other hand, the master links, which connect the master clocks between the different LHSs, are assumed to use free-space links. These links are modelled with a higher uncertainty of 10^{-18}, reflecting the bigger challenges associated with long-distance free-space clock comparisons, including atmospheric variations and signal attenuation. Despite the relatively higher uncertainty, the reduced-link configuration (as described in section 4.1.3) illustrated that the impact of these master link uncertainties is minimized, as they are strategically used in inter-LHS comparisons only.

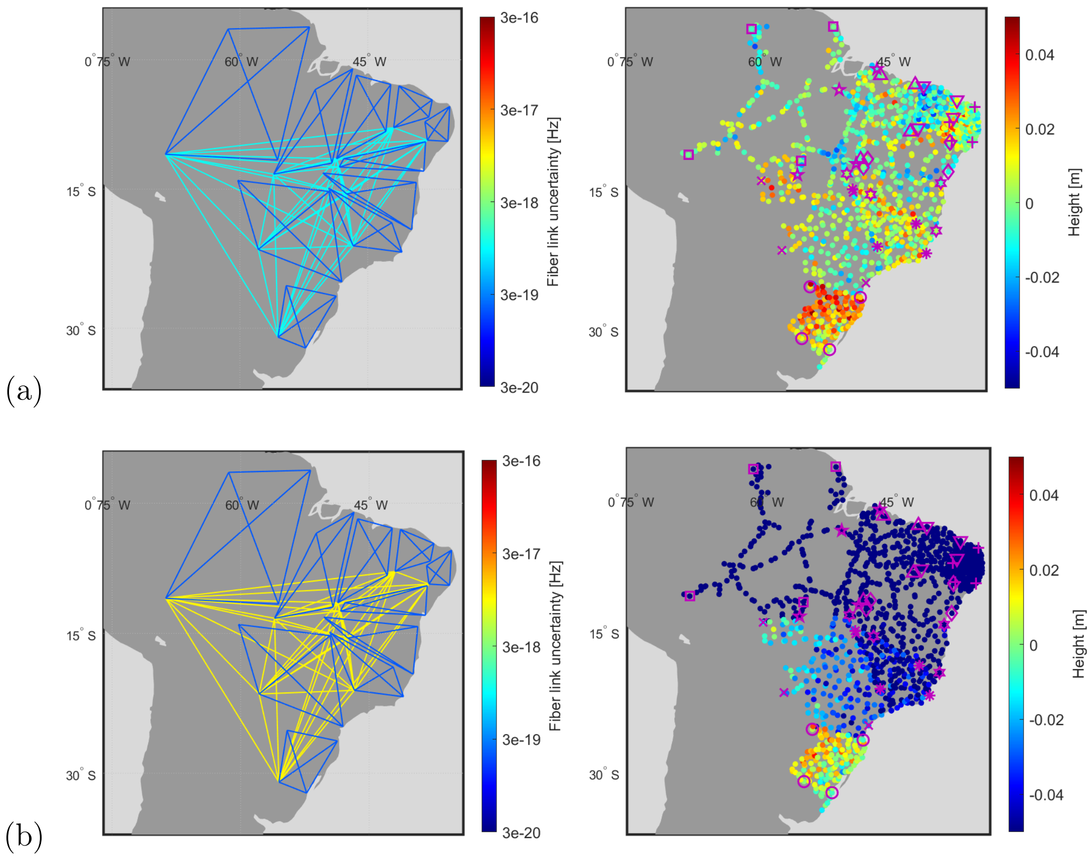

Figure 4.11: Link uncertainty and adjusted error (after unification) with different cases of free-space and fibre links for master and local clock connections. In all cases, local connections are assumed with precise optical fibre links (10^{-19}). All master links are assumed as 10^{-18} free-space links (a) and 10^{-17} free-space links (b).

Table 4.5: RMS error of each LHS after unification

LHS	H1	H2	H3	H4	H5	H6	H7	H8	H9	H10
RMS Error - 10^{-18} (cm)	1.08	1.23	1.03	1.43	1.37	1.42	1.13	1.29	1.19	2.43
RMS Error - 10^{-17} (cm)	18.0	17.1	13.0	12.3	9.83	7.82	6.56	4.88	2.95	1.39

The effectiveness of this approach is demonstrated in figure 4.11, which shows the results of the reunification under varying levels of link uncertainties for the master links. The simulations reveal that a reunification accuracy of approximately 1 cm can still be achieved when 10^{-18} free-space links are combined with 10^{-19} optical fiber links in the specified link configuration. The overall accuracy in each LHS is provided in table 4.5 for the two cases. This level of accuracy underscores the robustness of the proposed clock network design, which leverages the strengths of optical fiber links for local precision and free-space links for inter-LHS connection. By carefully managing the uncertainties associated with each type of link, the network achieves a balance between accuracy, feasibility, and operational efficiency, making it suitable for real-world height system unification scenarios.

Robust Parameter Estimation Approach

In practical applications of clock-based height system unification, the possibility of outliers in clock observations cannot be overlooked. Outliers, which can arise due to errors in clock performance, propagation delays, or measurement inaccuracies, can significantly affect the accuracy of the reunification. This issue becomes particularly critical in configurations with a reduced number of clock links, such as the proposed 105-link network for Brazil. With fewer reliable observations, the impact of even a small number of outliers is amplified. The impact of different outlier distributions on the results can be assessed by varying the number and placement of the outliers. To test the robustness of the unification process under such conditions, outliers are deliberately introduced into the clock observations. These outliers are modelled with errors in the order of $50\,\mathrm{m}^2/\mathrm{s}^2$, equivalent to approximately 5 m in height, ensuring the simulation reflects realistic error magnitudes.

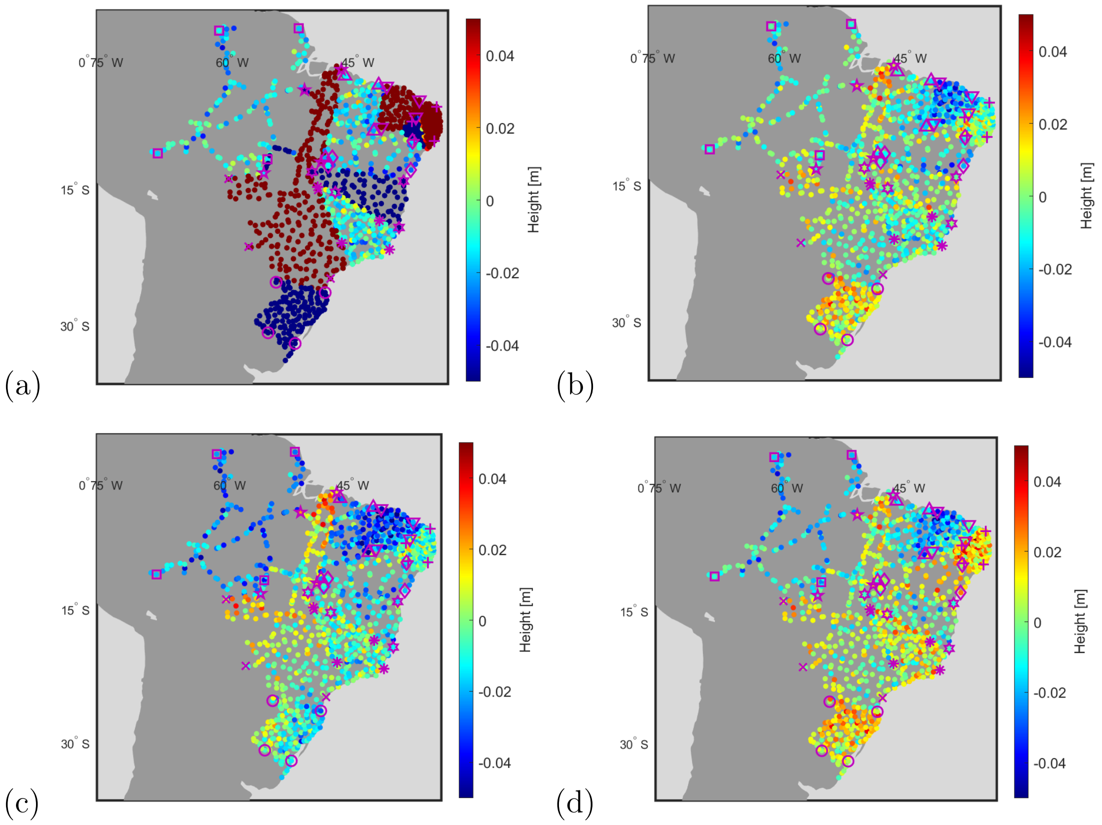

Figure 4.12: Adjusted error after reunification with outliers distributed among all links (a), with zero weight assignment to outliers (b), when Huber's RPE method was applied (c) and when Huber's RPE was applied with outliers introduced only to master links (d).

During the unification process, two approaches are investigated to handle outliers. First, outliers can be completely removed from the dataset by assigning them a weight of zero in the adjustment. In the first iteration, standardized residuals (v_i) are computed, and a cutoff value k (Huber tuning constant) is applied to classify outliers such that if $|v_i| > k$, the weight is set to zero, while inliers retain a weight of one. The second iteration involves re-running the least-squares adjustment with these modified weights, effectively excluding outliers from affecting the solution. A unification accuracy of < 2.4 cm for all LHSs can be achieved with this method (figure 4.12(b)). This approach eliminates the influence of unreliable observations but reduces the total number of observations. Alternatively, a robust estimation method, such as Huber's iteratively reweighting algorithm (Huber, 2011), can be applied (section 2.3.6). This method down-weights the effect of the outliers rather than eliminating them entirely, allowing the remaining portion of the data to contribute to the adjustment. Huber's method is particularly advantageous in cases where it is challenging to definitively classify an observation as an outlier. This method combines the strengths of least-squares regression for small residuals and down-weighting outliers for large residuals. With a tuning constant $k = 1.345 \cdot \sigma$ (where $\sigma = 0.1$), weights (p) were calculated based on the standardised residuals (v): for $v \leq k$, the weight was set to 1, and for $v > k$, the weight was set to k/v. This weighting scheme allows the estimator to achieve 95 % efficiency under Gaussian noise while mitigating the influence of outliers.

When outliers were introduced selectively, affecting only master links (which connect local height systems), the unification accuracy was significantly better, achieving values below 2 cm (figure 4.12(d)). This is because the local systems' internal consistency was preserved, and the impact of master-link outliers was efficiently reduced through the reweighting process. However, when outliers were distributed evenly across both local and master links, the unification accuracy decreased slightly to approximately 3.5 cm (figure 4.12(c)). This drop in performance is attributed to the additional variability introduced by the outliers in the local systems, which increased the overall noise in the adjustment process. The even distribution of the outliers required robust estimation to compensate for both inter- and intra-system inconsistencies, reducing the overall effectiveness compared to the scenario with outliers limited to master links.

The efficacy of this outlier management strategy is evaluated by comparing the unification accuracy before and after applying the detection and handling methods. Simulations demonstrate that the introduction of outliers, even when handled effectively, can impact the standard deviation of the estimated parameters. However, with a carefully designed network and robust outlier handling methods, the unification process can still achieve good accuracy. These results highlight the importance of combining network optimization with advanced statistical techniques to ensure reliable height system unification in the presence of outliers.

Time Correlation in Clock Observation

In the context of clock-based height unification, the impact of time correlations in clock observations was analyzed. With a clock distribution of four clocks in each local height system, the connections in the local systems were assumed to generate correlated observations due to the presence of common clocks. Specifically, each pair of clocks in an LHS is linked, resulting in six clock observations per LHS. However, due to correlations between these local links, the effective number of independent observations is reduced to three (figure 4.13).

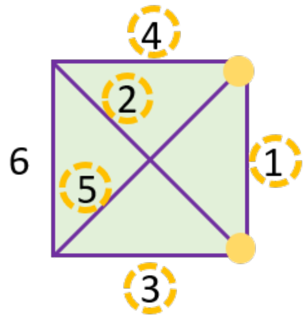

Figure 4.13: Demonstration of correlated and independent clock observations within a local height system. Here, observation labelled 1 is correlated with all other observations except 6 with the common clock at LRC (Lower Right Corner) and URC (Upper Right Corner). Similarly, the other non-correlated observations are between 3 - 4 and 2 - 5.

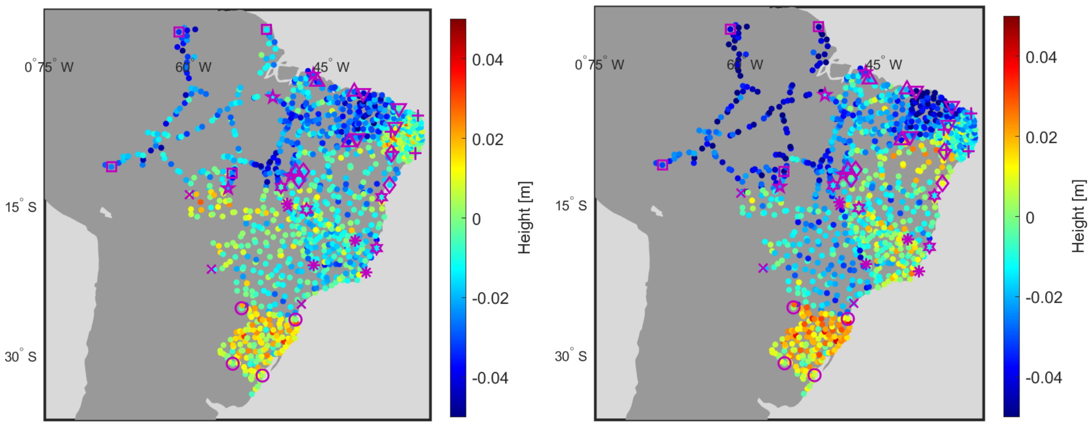

Figure 4.14: Adjusted errors after reunification with correlation coefficients 0.5 (left) and 0.8 (right). Here, CE (Clock Error) is supplied as a random normal distribution of constant variance 0.1 m^2/s^2.

The reduction in the number of independent observations emphasizes the importance of accounting for correlation structures (equation (2.33)) in the adjustment procedure. Time correlations affect the covariance matrix of the observations and, subsequently, the estimation of the transformation parameters such as offsets (OT^L) and tilts (a^L and b^L) in the LHSs. Simulations indicate that even with correlated observations, the network of four clocks per LHS provides sufficient redundancy for achieving a fair unification accuracy, particularly when the spatial distribution of the clocks is optimized as discussed earlier. The results highlight how correlations of the clock observations affect the unification accuracy.

In the case where observations are assumed independent (no correlation), the least-squares adjustment achieves an accuracy of $\approx$ 1 cm in each LHS. This is because each observation provides unique, independent information, maximizing the effectiveness of the adjustment process. However, when a moderate correlation ($\rho = 0.5$) is introduced between some observations, the accuracy significantly reduces to $\approx$ 2.5 cm for some LHSs (figure 4.14 (left)). This reduction occurs because correlated observations contain redundant information, effectively reducing the total amount of independent data available for parameter estimation. With strong correlation $\rho = 0.8$, the rms error further reduces to $\approx$ 4 cm (figure 4.14 (right)). Real-world applications must explicitly incorporate the correlation structure into the covariance matrix, using generalized least-squares or other advanced techniques, to ensure robust unification results. Additionally, the spatial distribution of the clocks should be optimized to minimize the effects of correlation, ensuring high accuracy even in scenarios with significant interdependence between the observations.

4.2 Height System Unification to A Global Geoid

The unification process initially focuses on separately aligning the European and Brazilian height systems to their respective predefined datums. For Europe, the NAP serves as the unifying datum, while Imbituba is chosen as the datum for Brazil. These local systems are not directly aligned with the global geoid (G), requiring an additional step to achieve global unification.

According to Sánchez (2015), the offset between the Imbituba datum and the global geoid is known to be 39 cm with an accuracy of ± 2 cm. This high-accuracy offset value enables a straightforward approach for referencing all heights in the European system to the global geoid. By first unifying the European system to the Imbituba datum and subsequently incorporating the offset of Imbituba to the global geoid, all height values can be consistently defined in relation to the global geoid.

The unification of the two systems involves estimating the offset OT^1, which represents the potential difference between NAP and Imbituba. A single clock observation between the two local systems suffices for this purpose, as only one transformation parameter, OT^1, needs to be determined. Although, for redundancy reasons more observations are recommended. The relationship between the clock observation, geopotential numbers, and OT^1 is given by

$$OT^1 = C_j^{L1} - C_i^{L2} - \Delta W_{ij},$$

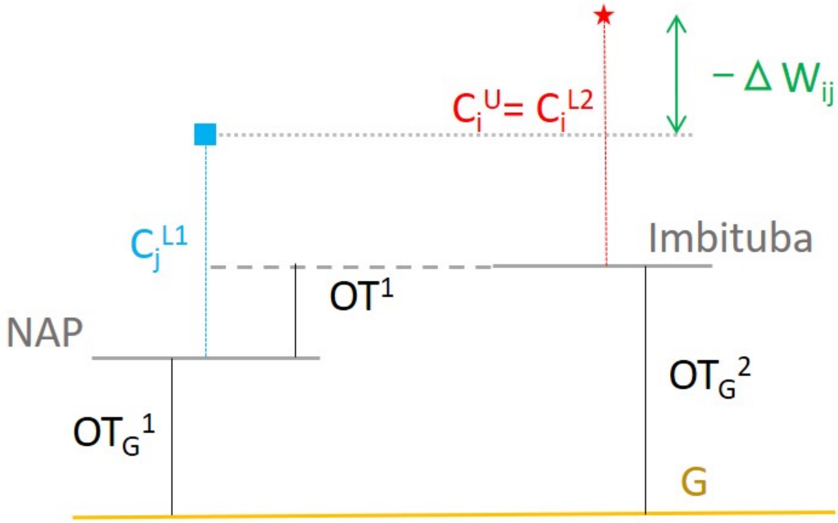

Figure 4.15: Unification to the global geoid using a single clock comparison ΔW_{ij} between site i in Brazil (L2) and site j in Europe (L1).

where C_j^{L1} and C_i^{L2} are the geopotential numbers at the connecting clock sites in Europe and Brazil, respectively, and ΔW_{ij} is the observed gravity potential difference between these clock sites. The relationship is illustrated in figure 4.15.

Once OT^1 is determined, the offset between NAP and the global geoid (OT_G^1) can be calculated as:

$$OT_G^1 = OT^1 + OT_G^2,$$

where OT_G^2 is the known offset of Imbituba to the global geoid. This process enables that all heights in the unified system are referenced to the global geoid, achieving an accuracy of approximately 3 cm when clocks and links with uncertainties of 10^{-18} are employed (**?**). This approach significantly improves upon the current global geoid height accuracy of around 10 cm (Woodworth et al., 2012; Ihde et al., 2017), providing a consistent and highly precise reference framework for global geodetic applications.

Chapter Summary

The potential of chronometric levelling in unifying existing local height systems to establish a global height system is evaluated in this simulation study. In order to propose a more realistic unification approach, we have defined complex transformation parameters between different LHS, considered clocks with different frequency standards (uncertainties), and generated clock observations considering clock errors, tidal corrections, link uncertainties, and outliers. The number of clocks and their spatial distribution are crucial in the estimation of various possible errors. As tidal effects affecting terrestrial clock measurements can be effectively modelled with uncertainties at the 10^{-19} level, they can be corrected or neglected in the unification process. The clock network configuration with the categorization of clocks into master and local ones along with reduced link performances is sufficient to deliver about 1 cm unification accuracy when 10^{-18} clocks are used. Fibre link uncertainties can be achieved at the order of 10^{-19}, thus clock noise dominates when averaging to 3 hourly or daily solutions. For clock comparisons over very large distances on a global scale, free-space links are required, which is challenging. Thus, the study of such comparisons, e.g., via satellite relays in the context of relativity is the topic of future work. But if all external factors such as residuals in the ionospheric models and tidal model, velocity and position errors of the satellites, second-order Doppler shifts, etc. are obtained in the range $\leq 10^{-18}$, then the space clock uncertainty may dominate and has to be reduced. In the present scenario, it is approximately 5×10^{-17} with the ACES mission, although an optimistic value of 10^{-18} is used in the study to achieve a 1 cm unification accuracy.

Time correlation of clock errors significantly degrades the accuracy of clock-based height unification. As correlation increases, the observations become less independent, leading to information redundancy that degrades the adjustment accuracy, from $\approx$ 1 cm with uncorrelated data to around 4 cm under high correlation. To maintain good accuracy, it is essential to model correlations accurately using an appropriate covariance structure and optimize the spatial distribution of the clocks. The unification process of local height systems to the global geoid was demonstrated by aligning the European and Brazilian height systems through a single clock observation, achieving an accuracy of approximately 3 cm when 10^{-18} clocks and links are used.

This approach does not demand fixed lab clocks; campaigns with transportable clocks can be conducted as only a single observation between two clocks is needed at any chosen measurement epoch. As the vertical coordinate of the IHRS is defined as the geopotential number, chronometric levelling has high relevance as clock observations are the only tool that directly provides measurements of gravity potential variations.

5 Application III - Absolute Sea Level Monitoring Networks

5.1 Study Area and Methodology

5.1.1 Study Area

For this study part, we focus on six tide-gauge locations along the European coast, specifically Newlyn (UK), Andenes (Norway), Reykjavik (Iceland), Ibiza (Spain), Genova (Italy), and Kalix (Sweden). These locations were chosen based on the availability of nearby GNSS stations with sufficiently long time-series data to support long-term analyses. The tide-gauge sites are geographically distributed to capture a range of oceanic and geophysical conditions affecting sea level variations. Figure 5.1 illustrates the spatial distribution of the selected sites.

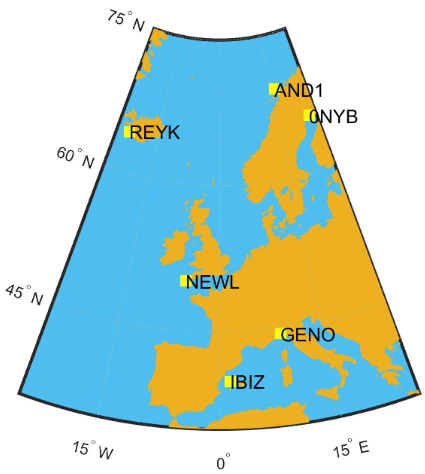

Figure 5.1: Tide-gauge locations considered in this study part: NEWL(Newlyn), AND1 (Andenes), REYK (Reykjavik), IBIZ (Ibiza), GENO (Genova), and, 0NYB (Kalix).

The selected tide-gauge locations represent a variety of coastal environments, offering insights into the spatial variability of Absolute Sea Level (ASL) changes. Key characteristics of these sites are:

- Newlyn, UK: Situated in the northeast Atlantic Ocean, providing data affected by North Atlantic dynamics.

- Andenes, Norway: Located in the Norwegian Sea, where polar tides and Arctic effects are significant.

- Reykjavik, Iceland: Representative for North Atlantic subpolar conditions and tectonic influences.

- Ibiza, Spain: A Mediterranean site capturing semi-enclosed sea dynamics.

- Genova, Italy: Another Mediterranean location, reflecting different geophysical and oceanographic conditions.

- Kalix, Sweden: Positioned in the Baltic Sea, affected by unique regional factors such as isostatic rebound and restricted water exchange.

5.1.2 Methodology

The study uses observational and simulated datasets spanning the time period 2006–2016, based on the availability of relevant data for the selected sites. Monthly RSL (Relative Sea Level) data in Revised Local Reference (RLR) format is obtained from the Permanent Service for Mean Sea Level (PSMSL) (Holgate et al., 2013; PSMSL, 2023). These data are corrected for local variations and represent relative sea level changes measured by the tide gauges. To derive the RSL change over the study period, the mean of the time series is subtracted from the monthly RSL values, resulting in an anomaly time series that reflects temporal variability of the sea level (figure 5.2)

Simulation of Clock Observations

Clock observations are simulated to estimate physical height changes due to the combined effects of tidal and non-tidal effects, as defined in equation (2.39)

$$\Delta H^v = \Delta H^v_{tidal} + \Delta H^v_{non-tidal}. \tag{5.1}$$

The physical height variations include contributions from:

- Tidal Effects (ΔH^v_{tidal}): These include solid Earth tides, ocean-loading tides, pole tides, and other periodic tidal forces (section 5.2.1).

- Non-tidal Effects ($\Delta H^v_{non-tidal}$): These include vertical displacements and mass anomalies caused by mass redistribution in the geosphere, hydrosphere, atmosphere, and biosphere (section 5.2.2).

The simulated clock observations thus represent effective vertical displacements (ΔH^v), which are key to determining time-variable physical height changes at the tide gauge locations.

Derivation of Absolute Sea Level Changes

Absolute sea level changes are computed by combining the simulated physical height changes from clock observations with the RSL anomalies derived from the PSMSL dataset (equation (2.38)). To ensure consistency and accuracy in the ASL estimation, a stable reference clock related to the geoid (W_0) is assumed as described in section 3.2. The systematic uncertainty of the optical fiber link is considered to be at the level of 10^{-19}, as demonstrated in Lisdat et al. (2016),

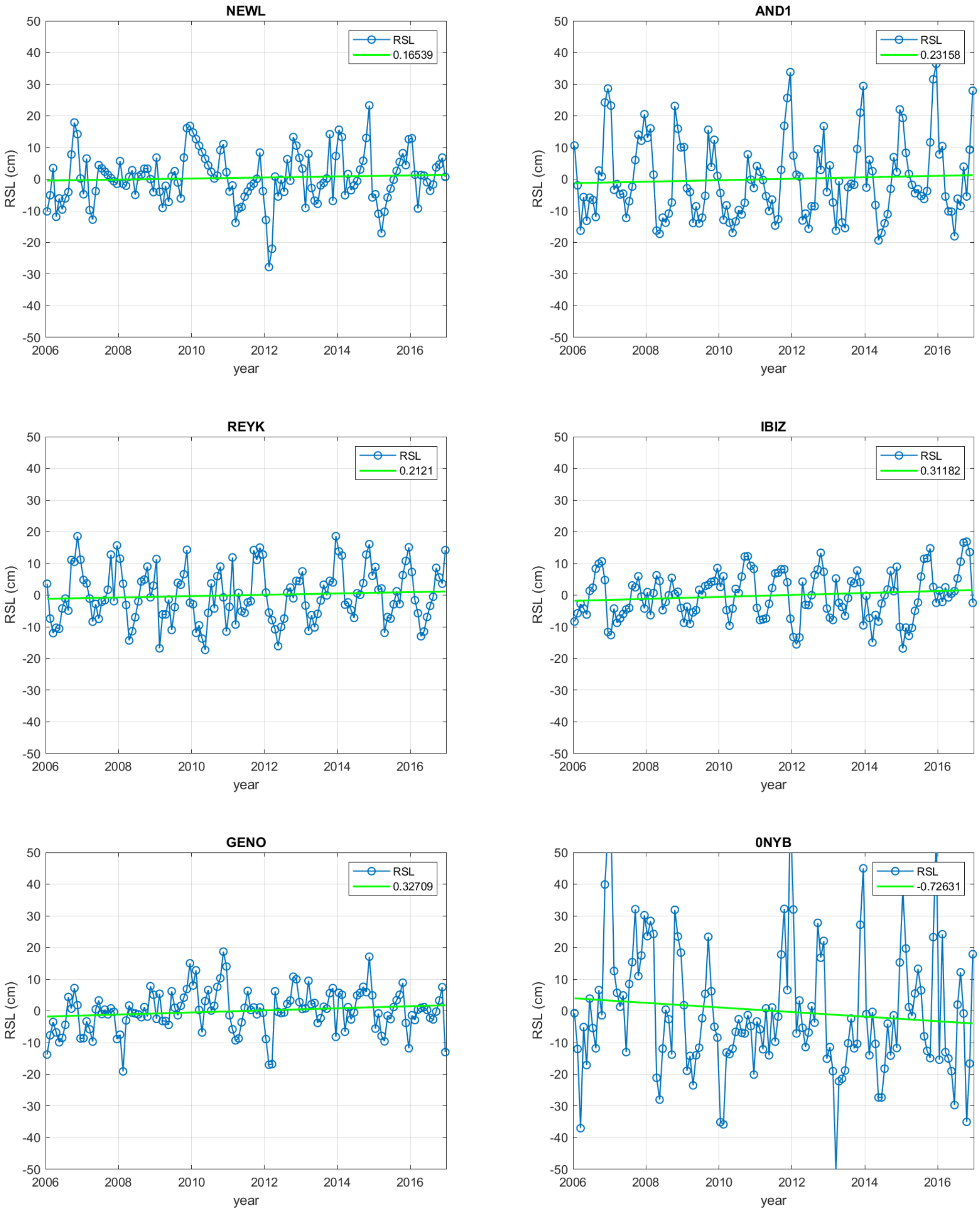

Figure 5.2: RSL change with the trend over the study period (10 years) at the selected clock sites.

while the space link accuracy is assumed to be at the 10^{-18} level (Shen et al., 2023a). These accuracies are sufficient to achieve a accuracy of 1 cm in ASL estimation.

By combining clock-based measurements with traditional tide-gauge data, this approach provides a novel means of assessing ASL changes with high spatial and temporal consistency at diverse locations. This methodology enables referencing land and sea level changes directly to the global geoid, thereby eliminating inconsistencies arising from regional vertical datum variations.

5.2 Land Motion from Clock Observation

The use of terrestrial clocks for measuring land motion provides a direct means of capturing vertical displacements by referencing changes in the gravity potential. Clocks are uniquely sensitive to geopotential variations, enabling the detection of mass redistributions that result in both tidal and non-tidal vertical motions. The physical height changes obtained from clock observations reflect the cumulative effects of various geophysical processes as described in section 2.2.1. These include solid-earth tides, ocean-loading tides, pole tides, and atmospheric influences, as well as non-tidal mass redistributions in the Earth's system. This capability positions clocks as a complementary tool to GNSS systems, offering a highly accurate, equipotential-based approach to monitoring land motion globally. The physical height changes measured through clocks eliminate regional discrepancies caused by variations in vertical datums, ensuring consistent observations across different locations.

5.2.1 Simulation of Tidal Signals

The simulation of tidal signals is crucial for understanding the contribution of tidal effects to land motion and associated potential variations. Potential variations caused by solid-earth tides, pole tides, and LOD (Length of Day) tides are computed on a deformable Earth surface using the modified ETERNA34 (PREDICT program) Earth tide data processing package (Wenzel, 2022). This package incorporates the HW95 (Hartmann and Wenzel, 1995) tidal potential catalogue to derive high-resolution hourly tidal potential values. These hourly values are subsequently averaged to produce monthly values, providing a comprehensive representation of the tidal behavior over the chosen study period. Similarly, the potential variations arising from ocean tidal loading are simulated using the SPOTL3.3.0.2 package (Agnew, 2012). This package leverages the Empirical Ocean Tidal model (EOT11a) (Savcenko and Bosch, 2011) to compute monthly averages of ocean-induced potential variations, capturing the influence of oceanic mass redistribution on land motion.

Both ETERNA34 and SPOTL provide effective potential variations due to mass changes and associated surface displacements. These variations are instrumental in characterizing the impact of tidal effects at the study locations. The simulated major tidal values at the selected clock sites are illustrated in figure 5.3, highlighting the spatial variability of tidal effects at high latitudes (AND1, 0NYB, REYK) and low latitudes (GENO, IBIZ). Among the tidal contributions, LOD tidal values, which are of the order of 0.001 m^2/s^2, can be safely neglected due to their minimal impact. Similarly, atmospheric tidal values, which are orders of magnitude smaller than the sensitivity threshold of 10^{-18} (equivalent to 0.1 m^2/s^2) for high-performance clocks, are also disregarded (Voigt et al., 2016).

The monthly averages of solid-earth tidal effects exhibit significant variability, with amplitudes reaching approximately 10 cm at high-latitude sites. This underscores the importance of including these effects in total land motion simula-

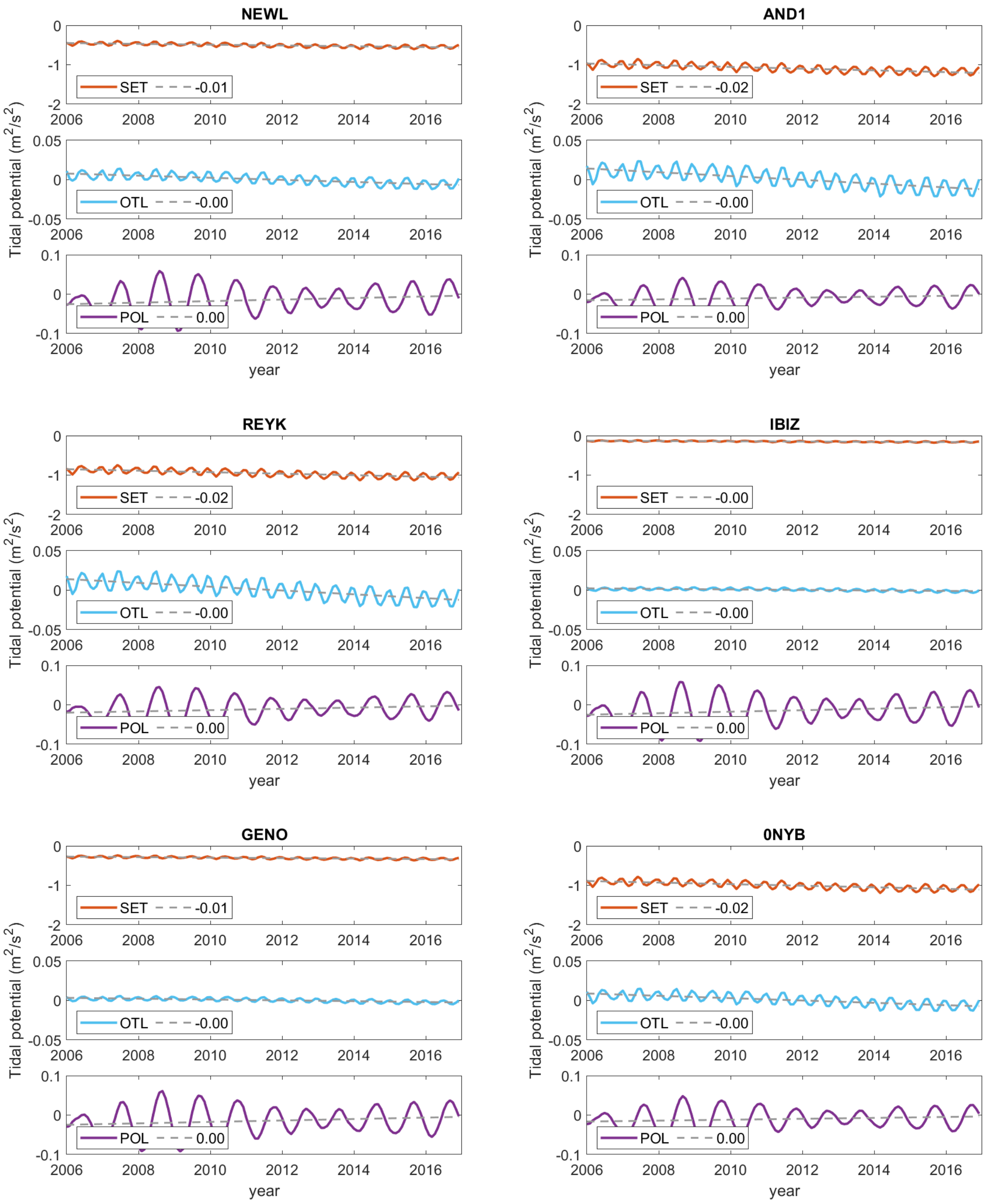

Figure 5.3: Monthly averages of solid-earth tides (SET), ocean-load tides (OTL) and pole tides (POL) with their linear trends at selected clock sites

tions. The three primary tidal contributions—solid-earth tides, pole tides, and ocean tidal loading—are combined to generate the total tidal effects, as depicted in the second subplots of figure 5.6. The observed negative long-term trend in the tidal values is attributed to the 18.61-year lunar nodal cycle (figure 5.4), a well-documented astronomical phenomenon. According to Rochlin and Morris (2017), the Moon's orbital declination was at its smallest from 2005 to 2015, leading to increasing tidal amplitudes and corresponding negative potential variations on the Earth's surface (figure 5.5). This simulation provides a detailed understanding of

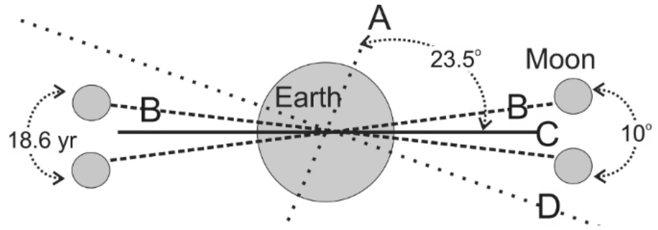

Figure 5.4: llustration of the Earth's rotation (axis A), its orbit around the Sun (plane C), and the Moon's orbital plane (B) inclined by 5.14° to the ecliptic. The lunar declination angle relative to Earth's equatorial plane (D) varies approximately 10° between 18.18° and 28.36° over an 18.6-year period (Rochlin and Morris, 2017).

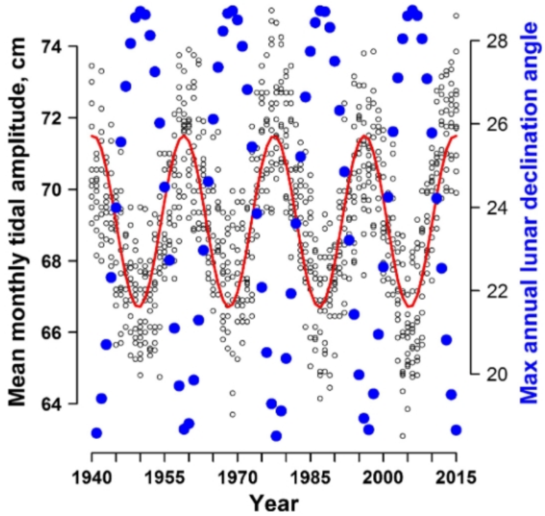

Figure 5.5: Time series showing tidal amplitude and lunar declination angle variations. Data from the NOAA tide gauge at Battery, NYC (Station ID: 8518750) fitted with a harmonic regression (red line, amplitude: 2.4 cm, mean: 69.1 cm, period: 18.6 years) (Rochlin and Morris, 2017).

how tidal forces affect land motion and potential variations over time, enhancing the interpretation of clock-based observations.

5.2.2 Simulation of Non-tidal Signals

Non-tidal mass distributions play a significant role in causing vertical displacements and associated potential variations, resulting from processes such as changes in Terrestrial Water Storage (TWS), atmospheric pressure, ocean bottom pressure, and solid earth dynamics like Glacial Isostatic Adjustment (GIA) (?). These mass redistribution effects are essential to understanding the non-tidal contributions to land motion. The geoid height variations resulting from changes in TWS are derived using monthly spherical harmonic coefficients from the GRACE mission (Kvas et al., 2019). This approach provides a comprehensive representation of hydrological loading effects over the chosen study period. Similarly, atmo-

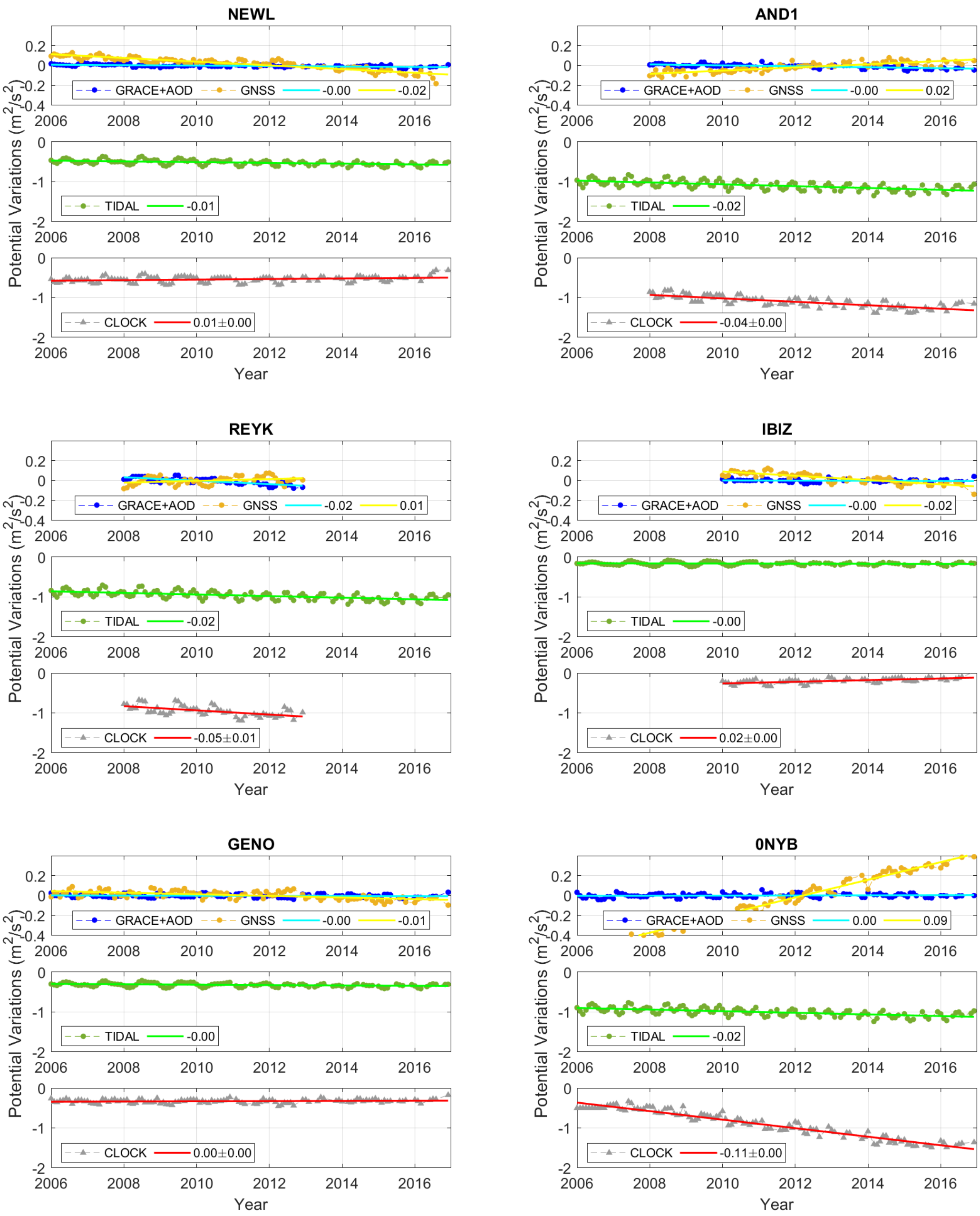

Figure 5.6: Simulated clock observations (CLOCK in each lower panel) by combining the potential variations due to non-tidal effects (mass changes in TWS (GRACE), atmosphere and ocean (AOD) and associated vertical deformations (GNSS) in each upper panel) and tidal effects (TIDAL=SET+OTL+POL in each middle panel) with their linear trends (m^2/s^2yr) at the tide-gauge sites.

spheric and ocean mass variability effects are quantified using fully normalized monthly spherical harmonic coefficients (GAC) from the Atmosphere and Ocean De-aliasing (AOD1B RL06) product (Dobslaw et al., 2017), allowing for a detailed evaluation of atmospheric pressure and ocean loading contributions.

Surface deformations associated with these non-tidal mass distributions are analyzed using GNSS time-series solutions provided by the Nevada Geodetic Laboratory (NGL) (Blewitt et al., 2018). These deformations reflect the impact of loading and unloading effects, where a loading event induces a downward vertical displacement and unloading causes an upward displacement. By combining the potential variations from mass changes (GRACE and AOD1B data) with the vertical displacements observed in GNSS time-series, the effective gravitational potential variations are calculated. This comprehensive approach ensures that both geoid height variations and surface deformations are captured, as illustrated in the first subplots of figure 5.6. The combined effects highlight the interplay between these geophysical processes, contributing to non-tidal signals observed at the study locations.

5.2.3 Monitoring Land Motion with Clock Observations

Simulated clock observations, incorporating both tidal and non-tidal potential variations as outlined in equation (2.39), provide a holistic view of land motion at the selected tide gauge locations. The third subplots of figure 5.6 depict these combined effects, demonstrating the capability of 10^{-18} precision clocks to resolve absolute land motion with an accuracy of 1 cm, corresponding to gravitational potential variations of 0.1 m^2/s^2. This level of sensitivity enables near real-time monitoring of vertical displacements. When considering monthly observations over several years, as performed in this study, the trend accuracy improves significantly, achieving an accuracy of less than 1 mm/yr. This enhanced temporal resolution allows for a detailed assessment of long-term trends and the separation of transient events from steady-state processes.

5.3 Geoid-based Absolute Sea Level Changes

As discussed in section 2.4.2, geoid-based ASL changes can be derived by integrating clock observations with RSL data from tide gauges, see equation (2.38). Clock-based measurements of height variations offer a globally consistent and uniform reference for determining ASL changes, overcoming regional inconsistencies inherent in traditional methods. The use of high-performance optical atomic clocks with a fractional frequency uncertainty of 10^{-18} (McGrew et al., 2018; Takamoto et al., 2022), combined with link accuracies at the same level, facilitates the derivation of ASL changes with a remarkable accuracy of 1 cm.

To estimate ASL changes, the monthly variations of RSL are determined by subtracting the mean value calculated over the selected time span. Clock observations, simulated as potential variations (m^2/s^2), are converted into physical height variations (cm) by multiplying with the mean gravity acceleration g. These height variations are then combined with the RSL changes to produce the ASL estimates. Figure 5.7 illustrates the estimated ASL changes alongside the long-term trend, clock-derived physical height observations, and RSL variations. Notably,

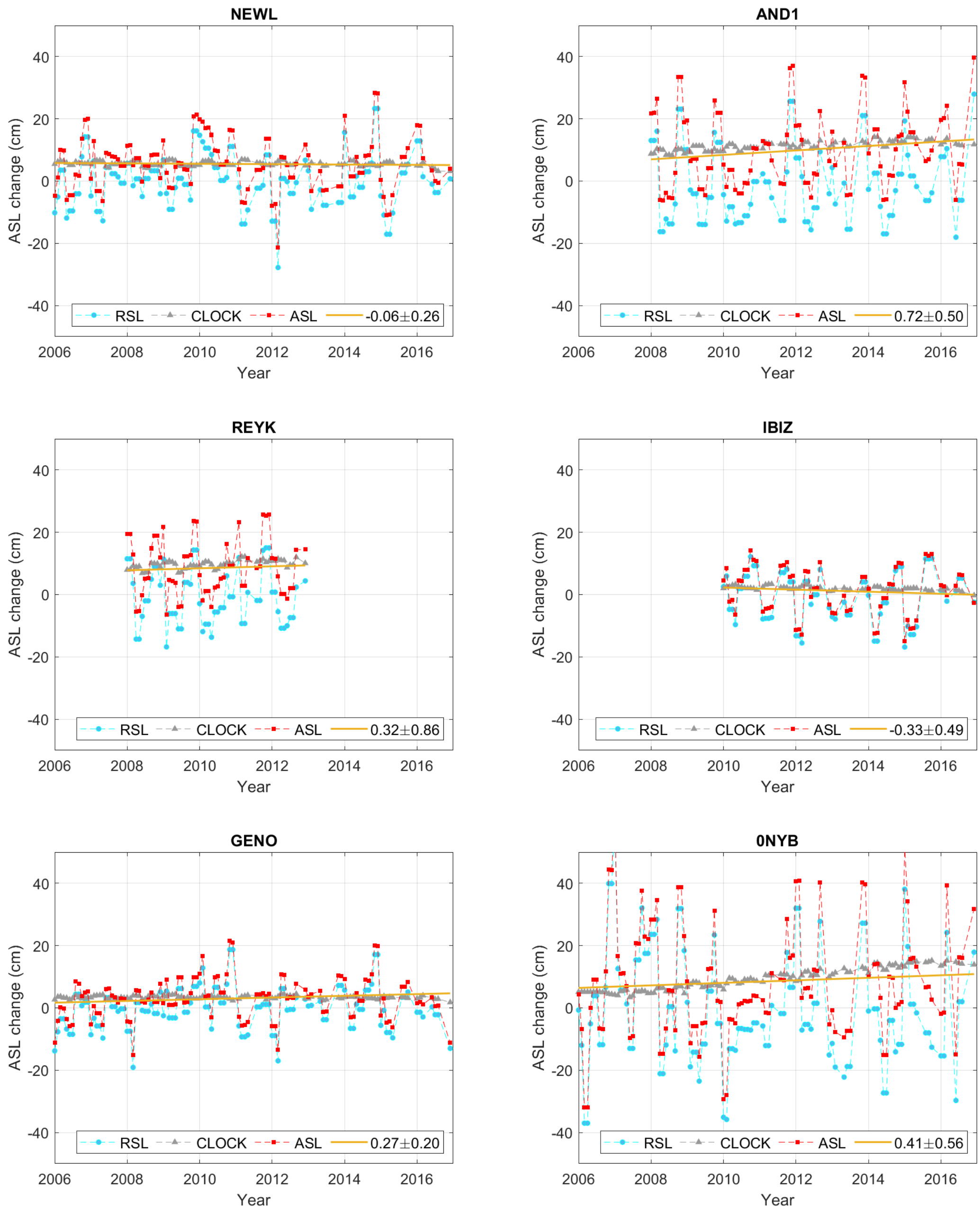

Figure 5.7: Estimated monthly ASL changes (ASL) by reducing the clock observations (CLOCK) from RSL changes (RSL) at the tide gauge sites. The long-term trends of ASL changes (cm/yr) are also given.

measurement noise in RSL data introduces uncertainties in the ASL estimation process.

The impact of present-day land uplift on ASL estimation is significant. For instance, the land uplift at Kalix (0NYB) manifests as a misleading sea level fall. This underscores the importance of accounting for land motion when interpreting sea level changes. As visible in figure 5.7, the monthly average of land motion (CLOCK) contributes to the difference between the monthly averages of ASL change (ASL) and the RSL change (RSL) at the clock sites. The linear trend analysis across the tide gauge locations for the specified time period reveals an overall increase in ASL, confirming the current scenario of global sea level rise.

Seasonal or inter-annual variations in ASL may arise from steric changes due to variations in ocean heat content and barystatic changes caused by the exchange of water mass between land and ocean (Hamlington et al., 2020). Clocks inherently reflect the total effect of both mass redistributions and steric changes, which enables capturing the complete sea level changes similar to satellite altimetry. While these effects were not explicitly modelled in this study, their integration in future analyses could enhance the precision of ASL estimates and provide deeper insights into the mechanisms driving sea level variability. This approach underscores the potential of combining advanced clock observations with traditional tide gauge measurements to achieve accurate, consistent, and comprehensive ASL monitoring.

Chapter Summary

Traditionally, land-based Absolute Sea Level (ASL) measurements have been estimated relative to GNSS benchmarks or local tidal datums, which provide ASL changes with respect to a reference ellipsoid. While effective, these methods require additional calculations to achieve a globally consistent geoid-based measure of ASL. High-performance atomic clocks, with fractional frequency uncertainties as low as 10^{-18}, offer an interesting alternative. When deployed at tide-gauge locations with corresponding link uncertainty, these clocks can measure physical height changes with unprecedented accuracy, enabling the direct determination of geoid-based ASL changes. This approach overcomes the limitations of traditional methods, providing a uniform and globally consistent framework for ASL monitoring.

In this study, we estimated ASL changes at selected tide-gauge locations along the European coasts. Long-term trends derived for the time span 2008–2016 reveal notable geoid-based ASL changes. Among the analyzed sites, Andenes (AND1) exhibited the highest trend value of 0.71 ± 0.49 cm/year. Most sites showed increasing ASL trends, except for Ibiza (IBIZ) and Newlyn (NEWL), highlighting the necessity of site-specific analyses. Sites such as Kalix (0NYB), Andenes (AND1), and Reykjavik (REYK) are affected by substantial land uplift, which must be accurately modelled and accounted for to ensure reliable ASL estimates.

Tidal effects were found to be a critical factor, with monthly averages reaching amplitudes as high as 10–20 cm. This underscores the importance of integrating tidal corrections into ASL measurements. Furthermore, the observed 18.61-year lunar nodal cycle, which significantly affects tidal ranges, highlights the need for long-term observations to distinguish transient effects from underlying trends.

The realization of clock-based networks offers a novel method for ASL monitoring.

By leveraging the unique ability of atomic clocks to measure total gravity potential variations, this approach provides a comprehensive measure that inherently accounts for both mass redistribution and steric effects. This capability eliminates the need for complex corrections, offering a direct and globally consistent method for monitoring vertical land movements and ASL changes.

Our findings demonstrate the added value of deploying clock-based networks at tide gauge locations to address challenges associated with traditional sea level monitoring methods. As the accuracy and accessibility of atomic clocks continue to improve, their integration into geophysical and oceanographic studies promises to enhance our understanding of ASL dynamics, support global climate monitoring, and inform mitigation strategies for sea level rise.

6 Conclusions and Future Research

6.1 Conclusions

In this thesis, the potential of high-performance optical atomic clocks in geodesy has been investigated, focusing on three primary applications: monitoring time-variable gravity signals, realizing a global height reference system, and monitoring absolute sea level changes. By leveraging the achievable high accuracy of these clocks, some of the most pressing challenges in understanding and quantifying Earth's dynamic processes have been addressed.

The integration of clock networks into geodesy offers a novel approach to directly measure gravity potential changes, bypassing the limitations of conventional methods. The immense potential of high-precision clocks in capturing and interpreting a diverse array of geophysical signals is underscored in chapter 3. Through the detailed analysis of five case studies, the capability of clock-based observations to detect effective potential variations caused by mass redistribution and vertical deformations across different temporal and spatial scales has been demonstrated. In time series analysis with terrestrial clocks, the temporal variations in Earth's rotation can be ignored. The proposed constellation—a space-based clock coupled with ground-based regional clocks—proves effective for minimizing stability issues of the reference clock and reducing the required number of space links.

Seasonal hydrological processes in the Himalayan region induce effective potential variations within $[-0.2, 0.2]$ $\mathrm{m}^2/\mathrm{s}^2$, detectable by clocks with relative uncertainties at the 10^{-18} level. This capability opens pathways for detailed studies of monsoon dynamics and water resource management, offering a unified approach to integrating atmospheric and geodetic data. The Amazon exhibits more pronounced temporal water storage variations ($[-0.5, 0.5]$ $\mathrm{m}^2/\mathrm{s}^2$) due to its dominant hydrological cycle. Clock observations can capture the contrasting seasonal patterns across the basin, driven by the migration of the intertropical convergence zone. This emphasizes the clocks' ability to monitor extreme hydrological phenomena in one of the Earth's most dynamic regions. Simulated linear potential variations reveal ice mass loss-induced changes of up to 1 $\mathrm{m}^2/\mathrm{s}^2$ between 2004 and 2015. This highlights the efficacy of clocks in detecting regional differences in ice melting, complementing satellite gravimetry and other geodetic methods. In Fennoscandia, clocks can capture vertical land uplift trends near the uplift centre, with potential variations of 0.11 $\mathrm{m}^2/\mathrm{s}^2$ per year. The vertical uplift at the clock sites dominates the effective potential variations, and the mass change has only a minor effect. Therefore, clock networks may not provide more information than GNSS in Fennoscandia. The 2011 Tōhoku earthquake's co-seismic potential variations were captured, with GRACE detecting mass redistribution signals and GNSS providing geometric displacement data. Clock observations can offer insights into pre- and post-seismic phenomena. Geometric changes are the main factor in those tectonic process. Therefore, future high-performance atomic clocks with fractional frequency uncertainties around 10^{-19} hold promise for predicting geophysical events like earthquakes or volcanic eruptions. These case studies illustrate the versatility of clock networks in studying geophysical processes, from hydrology and ice mass loss to tectonic events. The spatial and temporal accuracy offered by clocks can enhance our understanding of the Earth's dynamic systems, by enabling the detection of subtle, localized changes to which other techniques may not be sensitive.

The realization of the international height reference system represents another relevant application of clock networks. By unifying local height systems into a global reference frame based on the geoid, this study has demonstrated the potential of clocks to overcome errors inherent in classical levelling methods and enhance spatial and temporal resolution compared to satellite-based approaches. Such a unified framework supports consistent elevation data critical for geophysical studies and practical applications like infrastructure planning and flood management. By integrating clock-based observations with classical levelling and gravimetric data, we have shown that the unification of regional height systems can achieve centimetre-level accuracy, significantly surpassing current methods.

For Europe, based on the EUVN2000 system linked to the Normaal Amsterdams Peil datum, and Brazil, tied to the Imbituba datum, the simulations illustrate the effectiveness of clock observations in correcting offsets, tilts, and site-specific errors. Tidal effects on terrestrial clocks, modelled with 10^{-19} uncertainty, can be corrected in the unification process considering daily averaged clock observations. Strategic placement of the clocks, particularly at the most extreme points of the local height systems, reference tide gauges, and high-elevation points, proved critical for accurately estimating the related error parameters. With an optimal clock network operating at 10^{-18}-level accuracy, unification errors are reduced to ≈ 1 cm for both regions, highlighting the effectiveness of clock-based approaches. A reduced-link configuration, where only the master clocks in local height systems are interconnected, was shown to maintain high accuracy while minimizing observational redundancy and logistical complexity. This configuration showcases the strengths of optical fibre and free-space links, achieving a practical balance between accuracy and feasibility for large-scale implementations.

Advanced statistical techniques, such as Huber's reweighting algorithm, ensure resilience against outliers, maintaining a unification accuracy below 2.4 cm in the presence of data inconsistencies. The simulations emphasized the importance of robust estimation methods in handling uncertainties, particularly in master links connecting local systems. Time correlations of clock observations introduce challenges to parameter estimation and unification accuracy (≈ 4 cm at high correlation levels) by reducing the effective number of independent measurements. To ensure robust results, time-correlated clock observations must be properly modeled using an appropriate covariance structure, and the spatial distribution of the clocks should be optimized to minimize correlation effects. The alignment of the European and Brazilian systems to a global geoid reference demonstrated the feasibility of establishing a unified height system at the global scale. By using the known offset between the Imbituba datum and the global geoid, all heights can consistently be referenced to the global geoid with an accuracy of approximately 3 cm.

Finally, the research has explored the feasibility of clock-based monitoring of absolute sea level (ASL) changes, offering a geoid-referenced approach that overcomes the inconsistencies of current relative sea level measurements and land motion. By simulating clock observations at tide gauge locations, a way for globally consistent and accurate tracking of sea level changes has been demonstrated, essential for understanding the impacts of climate change and supporting coastal resilience efforts. Clocks, with their remarkable sensitivity to changes in the Earth's gravity potential, enable the detection of both tidal and non-tidal mass redistributions. By capturing cumulative geophysical processes, including solid-earth tides, ocean-loading tides, pole tides, and non-tidal effects, clock-based measurements can provide a globally consistent and equipotential-based framework for monitoring vertical displacements. This capability complements traditional GNSS methods, eliminating regional discrepancies caused by variations in vertical datums and offering uniform observations.

Generally, tidal effects were found to be significant, particularly at high-latitude sites. Simulations revealed amplitudes of up to 10 cm for monthly averaged tidal effects, underscoring the need to account for these variations in land motion analyses. Similarly, non-tidal mass redistributions contribute substantially to vertical displacements and must be incorporated for an accurate interpretation of clock-based observations. By combining clock-derived height changes with relative sea level data from tide gauges, geoid-based ASL changes were estimated with cm level accuracy. The analysis, covering the period from 2008 to 2016, revealed notable spatial variability in ASL trends. Andenes exhibited the highest trend value of 0.71 ± 0.49 cm/year, while locations such as Ibiza and Newlyn had decreasing ASL trends. These variations underline the importance of site-specific analyses. Additionally, substantial land uplift was observed at high-latitude sites like Kalix, Andenes, and Reykjavik, highlighting the necessity of accurately modelling vertical land motion to ensure reliable ASL estimates. Long-term trend analyses confirm an overall increase in ASL, consistent with current global sea level rise scenarios. The sensitivity of clocks to both mass redistribution and steric effects allows for the complete capture of sea level changes, analogous to satellite altimetry. Our investigation highlights the enhanced potential achieved by high-performance atomic clocks, which can resolve land motion with an accuracy of 1 cm, reaching sub-millimetre precision for long-term trends. This capability supports the separation of transient events from steady-state processes, providing deeper insights into the mechanisms driving sea level variability. In conclusion, the integration of clock-based observations with tide gauge measurements can establish a novel and robust methodology for ASL monitoring.

Through dedicated simulations and realistic observational scenarios, the versatility and accuracy of atomic clock networks in advancing geodetic science have been highlighted in this thesis. Those clocks can revolutionize measurements of Earth's dynamic processes, providing a robust framework for sustainable geodetic practice and addressing critical global challenges.

6.2 Future Research

Future advancements in clock technology and clock-network configurations, including further optimization of clock distribution will strengthen their utility in geodesy. The integration of clock observations into a fully relativistic framework and addressing challenges in free-space clock links will expand their applicability, particularly for global-scale comparisons. The selection of an external reference clock for deriving time-variable signals at sites of interest can be further enhanced with forward-looking innovations, such as deploying space reference clocks on the Moon or geostationary satellites. Ultimately, high-performance clocks represent a promising tool for monitoring temporal signals, fostering innovative approaches to understanding Earth's dynamic processes. Further detailed studies can be conducted assuming 10^{-19} (and beyond) clocks to enable real-time estimation of gravity potential variations caused by precursor signals of geophysical processes (e.g., volcanic eruptions, earthquakes, etc.), facilitating the prediction and possible mitigation of various catastrophic events.

The flexibility offered by transportable clocks further increases their practicality for real-world implementations, even in regions with limited infrastructure. Future work should focus on the spatial distribution of clock networks, refining the handling of time-correlated observations, and exploring hybrid configurations that combine fixed and transportable clocks with proper links. Future accuracy will require a thorough study of chronometric reference frames in the context of general relativity beyond the first post-Newtonian order. There is yet a definition of generalized geopotential numbers that builds on the so-called redshift potential that holds to any order. Thus, it has to be analyzed how future, high-accuracy clock networks have to be described in a fully relativistic framework. Moreover, chronometric networks regarding, e.g., clock numbers, distribution, positions, and geometry can be further optimized. By addressing these challenges, clock-based height unification can play a pivotal role in the development of a consistent global height reference system, contributing to scientific and societal advancements in geodesy, hydrology, and climate science. An alternative to height system unification is the novel establishment of an international clock-based network with proper links, a futuristic vision that offers a method for providing consistent physical heights on a global scale.

As clock technologies continue to advance, their deployment in geophysical and oceanographic studies promises to redefine the standards for accurate, consistent, and comprehensive sea level monitoring on a global scale. With proper modelling and reduction of mass-related effects, steric effects can be estimated from the clock-based monitoring of total absolute sea level changes. Seasonal or inter-annual ASL variations, influenced by ocean heat content and barystatic changes, were not explicitly modelled in this study but represent a promising direction for future research.

Machine learning and artificial intelligence (AI) can greatly enhance clock-based geodetic applications by optimizing clock network design, improving real-time calibration and synchronization, and enabling advanced data fusion and signal processing. AI can also aid in detecting anomalies, high-resolution geopotential mapping and Earth observation, predicting geophysical events like earthquakes or volcanic eruptions, and refining geoid models for better sea level monitoring and climate studies. Additionally, these technologies could enhance satellite navigation accuracy, detect subtle space-time variations, and improve the prediction of long-term trends in sea level rise and other geophysical processes. By integrating AI, clock-based measurements can become an even more powerful tool for improving geophysical monitoring and disaster mitigation.

List of Figures

List of Tables

List of Abbreviations

ACES	Atomic Clock Ensemble in Space
AOD1B RL06	Atmosphere and Ocean De-aliasing Level-1B
ASL	Absolute Sea Level
BCRS	Barycentric Celestial Reference System
CE	Clock Intrinsic Uncertainties
EIGEN-6C4	European Improved Gravity Model of the Earth by New Techniques
EOT11a	Empirical Ocean Tide Model 2011 (With Altimeter Data)
ETERNA34	Earth Tide Data Processing Package version 3.40
EUVN2000	European Vertical Reference Network 2000
EVRF	European Vertical Reference Frame
GBM	Ganges-Brahmaputra-Meghna River Basin
GBVP	Global Boundary Value Problem
GCRS	Geocentric Celestial Reference System
GFZ	German Research Centre for Geosciences
GGM	Global Gravity Models
GIA	Glacial Isostatic Adjustment
GNSS	Global Navigation Satellite System
GOCE	Gravity Field and Steady-State Ocean Circulation Explorer
GRACE	Gravity Recovery And Climate Research
GRACE-FO	GRACE Follow-On
GRT	General Relativity Theory
HW95	Hartmann and Wenzel 1995
IAG	International Association of Geodesy
ICRF	International Celestial Reference Frame
IGS14	International GNSS Service 2014
IHRS	International Height Reference System
ITCZ	Intertropical Convergence Zone
ITRF	International Terrestrial Reference Frame
ITSG-Grace2018	Institute of Geodesy at Graz University of Technology GRACE Gravity Field Solution
JASON	Joint Altimetry Satellite Oceanography Network
LHS	Local Height System
LOD	Length-of-Day Tides
MSL	Mean Sea Level
NAP	Normaal Amsterdams Peil
NGL	Nevada Geodetic Laboratory
NIST	National Institute of Standards and Technology
NTAL	Non-tidal Atmospheric Loading
OLS	Ordinary Least Squares
OT	Offsets

OTL	Ocean Load Tides
PD	Propagation Delay
POL	Pole Tides
PSMSL	Permanent Service for Mean Sea Level
PTB	Physikalisch-Technische Bundesanstalt
RIKEN	Rikagaku Kenkyūjo
RLR	Revised Local Reference
RN	Random Noise
SET	Solid Earth Tides
SI	International System of Units
SIRGAS	Geocentric Reference System for the Americas
SPOTL3.3.0.2	Some Programs for Ocean-Tide Loading Version 3.3.0.2
ST	Systematic Tilts
TE	Tidal Effects
TGP	Tidal Potential Catalogue
TP	Total Precipitation
TWS	Terrestrial Water Storage
WLS	Weighted Least Squares

Bibliography

A. Aeppli, K. Kim, W. Warfield, M. S. Safronova, and J. Ye. Clock with 8× 10-19 systematic uncertainty. Physical Review Letters, 133 (2):023401, 2024.

D. C. Agnew. Spotl: Some programs for ocean-tide loading. 2012. URL https://api.semanticscholar.org/CorpusID:127800542.

T. Baker. Absolute sea level measurements, climate change and vertical crustal movements. Global and Planetary Change, 8(3):149–159, 1993.

F. Barthelmes. Global models. Encyclopedia of Geodesy, Springer International Publishing, pages 1–9, 2014.

A. Bauch. Caesium atomic clocks: function, performance and applications. Measurement Science and Technology, 14(8):1159, 2003.

R. E. Beehler, R. C. Mockler, and J. M. Richardson. Cesium beam atomic time and frequency standards. Metrologia, 1(3):114, 1965.

J. Benveniste, F. Birol, F. Calafat, A. Cazenave, H. Dieng, Y. Gouzenes, J. Legeais, F. Leger, F. Niño, M. Passaro, C. Schwatke, and A. Shaw. Coastal sea level anomalies and associated trends from jason satellite altimetry over 2002–2018. Scientific Data, 7, 10 2020. doi:10.1038/s41597-020-00694-w.

A. Bjerhammar. On a relativistic geodesy. Bulletin géodésique, 59(3):207–220, 1985. doi:10.1007/BF02520327.

A. Bjerhammar. Relativistic geodesy. U.S. Dept. of Commerce, National Oceanic and Atmospheric Administration, National Ocean Service, Charting and Geodetic Services, For sale by the National Geodetic Information Center, NOAA, Rockville, MD, 1986.

G. Blewitt, W. C. Hammond, and C. Kreemer. Harnessing the gps data explosion for interdisciplinary science. Eos, 99:485, 2018. doi:10.1029/2018EO104623.

M. Bondarescu, R. Bondarescu, P. Jetzer, and A. Lundgren. The potential of continuous, local atomic clock measurements for earthquake prediction and volcanology. In EPJ Web of Conferences, volume 95, page 04009. EDP Sciences, 2015.

B. Bookhagen and D. W. Burbank. Toward a complete himalayan hydrological budget: Spatiotemporal distribution of snowmelt and rainfall and their impact on river discharge. Journal of Geophysical Research: Earth Surface, 115(F3), 2010.

T. Bothwell, D. Kedar, E. Oelker, J. M. Robinson, S. L. Bromley, W. L. Tew, J. Ye, and C. J. Kennedy. Jila sri optical lattice clock with uncertainty of 2.0×1018. Metrologia, 56(6):065004, 2019. doi:10.1088/1681-7575/ab4089.

T. Bothwell, C. J. Kennedy, A. Aeppli, D. Kedar, J. M. Robinson, E. Oelker, A. Staron, and J. Ye. Resolving the gravitational redshift across a millimetre-scale atomic sample. Nature, 602(7897):420–424, 2022.

R. K. Burkard. NOAA Reprint of Geodesy for the Layman. US Department of Commerce, National Oceanic and Atmospheric Administration, 1977.

L. Cacciapuoti and C. Salomon. Atomic clock ensemble in space. Journal of Physics: Conference Series, 327:012049, 2011. URL https://api.semanticscholar.org/CorpusID:110370616.

L. Cacciapuoti, A. Busso, R. Jansen, S. Pataraia, T. Peignier, S. Weinberg, P. Crescence, A. Helm, J. Kehrer, S. Koller, et al. Atomic clock ensemble in space. In Journal of Physics: Conference Series, volume 2889, page 012005. IOP Publishing, 2024.

E. D. Caldwell, J.-D. Deschenes, J. Ellis, W. C. Swann, B. K. Stuhl, H. Bergeron, N. R. Newbury, and L. C. Sinclair. Quantum-limited optical time transfer for future geosynchronous links. Nature, 618(7966): 721–726, 2023. doi:10.1038/s41586-023-06032-5.

A. Cazenave and R. S. Nerem. Present-day sea level change: Observations and causes. Reviews of Geophysics, 42:RG3001, 2004.

J. Chen, A. Cazenave, C. Dahle, W. Llovel, I. Panet, J. Pfeffer, and L. Moreira. Applications and challenges of grace and grace follow-on satellite gravimetry. Surveys in Geophysics, 43(1):305–345, 2022.

I. Clock, O. Networking, Collaboration, :, A. Amy-Klein, E. Benkler, P. Blondé, K. Bongs, E. Cantin, C. Chardonnet, H. Denker, S. Dörscher, C.-H. Feng, J.-O. Gaudron, P. Gill, I. R. Hill, W. Huang, M. Y. H. Johnson, Y. B. Kale, H. Katori, J. Klose, J. Kronjäger, A. Kuhl, R. L. Targat, C. Lisdat, O. Lopez, T. Lücke, M. Mazouth, S. Mukherjee, I. Nosske, B. Pointard, P.-E. Pottie, M. Schioppo, Y. Singh, K. Stahl, M. Takamoto, M. Tønnes, J. Tunesi, I. Ushijima, and C. Vishwakarma. International comparison of optical frequencies with transportable optical lattice clocks, 2024. URL https://arxiv.org/abs/2410.22973.

J. R. Clynch. Earth models and maps. 2002.

B. A. C. O. N. B. Collaboration et al. Frequency ratio measurements at 18-digit accuracy using an optical clock network. Nature, 591(7851):564–569, 2021.

M. Collins. El niño-or la niña-like climate change? Climate Dynamics, 24: 89–104, 2005.

T. Damour, M. Soffel, and C. Xu. General-relativistic celestial mechanics. i. method and definition of reference systems. Phys. Rev. D, 43:3273–3307, May 1991. doi:10.1103/PhysRevD.43.3273. URL https://link.aps.org/doi/10.1103/PhysRevD.43.3273.

K. Dawidowicz. Sea level changes monitoring using gnss technology–a review of recent efforts. Acta adriatica, 55 (2):145–162, 2014.

P. Delva, H. Denker, and G. Lion. Chronometric Geodesy: Methods and Applications, pages 25–85. Springer International Publishing, Cham, 2019. doi:10.1007/978-3-030-11500-5_2.

H. Denker. Regional gravity field modeling: theory and practical results. In Sciences of Geodesy-II: Innovations and Future Developments, pages 185–291. Springer, 2012.

H. Denker. A new european gravimetric (quasi) geoid egg2015. 2015.

H. Denker, J.-P. Barriot, R. Barzaghi, D. Fairhead, R. Forsberg, J. Ihde, A. Kenyeres, U. Marti, M. Sarrailh, and I. Tziavos. The development of the european gravimetric geoid model egg07. In Observing our changing earth, pages 177–185. Springer, 2009.

H. Denker, L. Timmen, C. Voigt, S. Weyers, E. Peik, H. S. Margolis, P. Delva, P. Wolf, and G. Petit. Geodetic methods to determine the relativistic redshift at the level of 10^{-18} in the context of international timescales: a review and practical results. Journal of Geodesy, 92(5):487–516, 2018. doi:10.1007/s00190-017-1075-1.

R. Dietrich. Sea Level, pages 1–9. Springer Netherlands, Dordrecht, 2014. ISBN 978-94-007-6644-0. doi:10.1007/978-94-007-6644-0_173-1.

R. Dill and H. Dobslaw. Numerical simulations of global-scale high-resolution hydrological crustal deformations. Journal of Geophysical Research: Solid Earth, 118(9):5008–5017, 2013. doi:/10.1002/jgrb.50353.

P. A. M. Dirac. General theory of relativity, volume 14. Princeton University Press, 1996.

H. Dobslaw, I. Bergmann-Wolf, R. Dill, L. Poropat, M. Thomas, C. Dahle, S. Esselborn, R. König, and F. Flechtner. A new high-resolution model of non-tidal atmosphere and ocean mass variability for de-aliasing of satellite gravity observations: AOD1B RL06. Geophysical Journal International, 211(1):263–269, 07 2017. ISSN 0956-540X. doi:10.1093/gji/ggx302.

C. J. Donlon, R. Cullen, L. Giulicchi, P. Vuilleumier, C. R. Francis, M. Kuschnerus, W. Simpson, A. Bouridah, M. Caleno, R. Bertoni, et al. The copernicus sentinel-6 mission: Enhanced continuity of satellite sea level measurements from space. Remote Sensing of Environment, 258: 112395, 2021.

L. M. Dorman and B. T. Lewis. Experimental isostasy: 1. theory of the determination of the earth's isostatic response to a concentrated load. Journal of Geophysical Research, 75 (17):3357–3365, 1970.

B. C. Douglas. Sea level change in the era of the recording tide gauge. In International geophysics, volume 75, pages 37–64. Elsevier, 2001.

M. R. Drinkwater, R. Haagmans, D. Muzi, A. Popescu, R. Floberghagen, M. Kern, and M. Fehringer. The goce gravity mission: Esa's first core earth explorer. In Proceedings of the 3rd international GOCE user workshop, pages 6–8. Citeseer, 2006.

A. Eicker, L. Schawohl, K. Middendorf, M. Bagge, L. Jensen, and H. Dobslaw. Influence of gia uncertainty on climate model evaluation with grace/grace-fo satellite gravimetry data. Journal of Geophysical Research: Solid Earth, 129(5):e2023JB027769, 2024.

A. Einstein. The field equations of gravitation. Sitzungsber. Preuss. Akad. Wiss. Berlin (Math. Phys.), 1915: 844–847, 1915.

M. Ekman. A consistent map of the postglacial uplift of fennoscandia. Terra Nova, 8(2):158–165, 1996. doi:10.1111/j.1365-3121.1996.tb00739.x.

J. C. Espinoza, J. Ronchail, J. A. Marengo, and H. Segura. Contrasting north–south changes in amazon wet-day and dry-day frequency and related atmospheric features (1981–2017). Climate Dynamics, 52(9): 5413–5430, 2019.

W. Farrell. Deformation of the earth by surface loads. Reviews of Geophysics, 10(3):761–797, 1972. doi:10.1029/RG010i003p00761.

L. Favier. Sea level "for dummies". `https://blogs.egu.eu/divisions/cr/2016/10/19/sea-level-for-dummies/`, 2016. Blog post.

W. Featherstone. Absolute and relative testing of gravimetric geoid models using global positioning system and orthometric height data. Computers & Geosciences, 27(7):807–814, 2001.

C. Förste, S. L. Bruinsma, O. Abrikosov, J.-M. Lemoine, T. Schaller, H. Gtze, J. Ebbing, J. Marty, F. Flechtner, G. Balmino, et al. Eigen-6c4 the latest combined global gravity field model including goce data up to degree and order 2190 of gfz potsdam and grgs toulouse. GFZ Data Services., 10, 2014. doi:10.5880/icgem.2015.1.

D. A. Freedman. On the so-called "huber sandwich estimator" and "robust standard errors". The American Statistician, 60(4):299–302, 2006.

L.-L. Fu and A. Cazenave. Satellite altimetry and earth sciences: a handbook of techniques and applications. Elsevier, 2000.

M. Fujieda, S.-H. Yang, T. Gotoh, S.-W. Hwang, H. Hachisu, H. Kim, Y. K. Lee, R. Tabuchi, T. Ido, W.-K. Lee, M.-S. Heo, C. Y. Park, D.-H. Yu, and G. Petit. Advanced satellite-based frequency transfer at the 10^{-16} level. IEEE Trans. Ultrason. Ferroelectr. Freq. Control, 6:973–978, Oct. 2018. doi:10.1109/TUFFC.2018.2821159.

C. Gerlach and R. Rummel. Global height system unification with goce: a simulation study on the indirect bias term in the gbvp approach. Journal of Geodesy, 87:57–67, 2013.

S. K. Gill and J. R. Schultz. Tidal datums and their applications. 2001.

V. Gornitz. Sea-level rise: A review of recent past and near-future trends. Earth surface processes and landforms, 20(1):7–20, 1995.

E. Grafarend. The definition of the telluroid. Bulletin Géodésique, 52(1): 25–37, 1978.

J. Grotti, I. Nosske, S. Koller, S. Herbers, H. Denker, L. Timmen, G. Vishnyakova, G. Grosche, T. Waterholter, A. Kuhl, S. Koke, E. Benkler, M. Giunta, L. Maisenbacher, A. Matveev, S. Dörscher, R. Schwarz, A. Al-Masoudi, T. Hänsch, T. Udem, R. Holzwarth, and C. Lisdat. Long-distance chronometric leveling with a portable optical clock. Phys. Rev. Appl., 21:L061001, Jun 2024. doi:10.1103/PhysRevApplied.21.L061001. URL `https://link.aps.org/doi/10.1103/PhysRevApplied.21.L061001`.

T. Gruber, R. Rummel, J. Ihde, G. Liebsch, A. Rülke, U. Schäfer, M. Sideris, L. Rangelova, and P. Woodworth. Height system unification with goce summary and final report. Technical report, Technical Report GO-HSU-PL-0021, 2014.

R. Hackney and W. Featherstone. Geodetic versus geophysical perspectives of the 'gravity anomaly'. Geophysical Journal International, 154(1):35–43, 2003.

B. D. Hamlington, A. S. Gardner, E. Ivins, J. T. Lenaerts, J. Reager, D. S. Trossman, E. D. Zaron, S. Adhikari, A. Arendt, A. Aschwanden, et al. Understanding of contemporary regional sea-level change and the implications for the future. Reviews of Geophysics, 58(3): e2019RG000672, 2020.

J. Hartle. Gravity: An Introduction to Einstein's General Relativity. Cambridge University Press, Cambridge, 2021. ISBN 9781316517543. doi:10.1017/9781009042604.

T. Hartmann and H.-G. Wenzel. The hw95 tidal potential catalogue. Geophysical research letters, 22(24): 3553–3556, 1995.

S. Hawking and G. Ellis. The Large Scale Structure of Space-Time. Cambridge Monographs on Mathematical Physics. Cambridge University Press, 1975. ISBN 9781139810951. URL `https://books.google.de/books?id=9AUhAwAAQBAJ`.

D. M. Hawkins. A new test for multivariate normality and homoscedasticity. Technometrics, 23(1):105–110, 1981.

B. Heck. A brovar-type solution of the fixed geodetic boundary-value problem. Studia Geophysica et Geodaetica, 55:441–454, 2011.

A. T. Hoang, Z. Shen, and W.-B. Shen. Unifying the regional height system using optic-fiber clock network: A simulation test for southeast asia. IEEE Access, 11:92996–93003, 2023. doi:10.1109/ACCESS.2023.3308519.

B. Hofmann-Wellenhof and H. Moritz. Physical geodesy. Springer Science & Business Media, Vienna, 2006. doi:10.1007/b139113.

S. J. Holgate, A. Matthews, P. L. Woodworth, L. Rickards, M. E. Tamisiea, E. Bradshaw, P. R. Foden, K. Gordon, S. Jevrejeva, and J. Pugh. New data systems and products at the permanent service for mean sea level. 2013. URL `https://api.semanticscholar.org/CorpusID:129718672`.

P. J. Huber. Robust Statistics, pages 1248–1251. Springer Berlin Heidelberg, Berlin, Heidelberg, 2011. ISBN 978-3-642-04898-2. doi:10.1007/978-3-642-04898-2_594. URL https://doi.org/10.1007/978-3-642-04898-2_594.

R. Huggett. Earth's spheres: Conceptual and definitional debates. Progress in Physical Geography: Earth and Environment, 48(5-6):651–670, 2024.

J. Ihde, J. Adam, W. Gurtner, B. Harsson, M. Sacher, W. Schlüter, and G. Wöppelmann. The height solution of the european vertical reference network (euvn). Veröff. Bayer. Komm. für die Internat. Erdmessung, Astronom. Geod. Arb, 61:132–145, 2000.

J. Ihde, L. Sánchez, R. Barzaghi, H. Drewes, C. Foerste, T. Gruber, G. Liebsch, U. Marti, R. Pail, and M. Sideris. Definition and proposed realization of the international height reference system (ihrs). Surveys in geophysics, 38:549–570, 2017.

T. Imakiire and M. Koarai. Wide-area land subsidence caused by "the 2011 off the pacific coast of tohoku earthquake". Soils and Foundations, 52(5): 842–855, 2012.

T. Imakiire and T. Kobayashi. The crustal deformation and fault model of the 2011 off the pacific coast of tohoku earthquake. Bulletin of the Geospatial Information Authority of Japan, 59:21–30, 2011.

M. Jacobson, R. J. Charlson, H. Rodhe, and G. H. Orians. Earth System Science: from biogeochemical cycles to global changes. Academic Press, 2000.

C. Jekeli. Heights, the geopotential, and vertical datums. 2000.

C. Jekeli. Potential theory and static gravity field of the earth. Geodesy, 3: 11–42, 2007.

G. Jentzsch. Earth tides and ocean tidal loading. Tidal phenomena, pages 145–171, 2005.

T. Jeon, K.-W. Seo, K. Youm, J. Chen, and C. R. Wilson. Global sea level change signatures observed by grace satellite gravimetry. Scientific Reports, 8(1):13519, 2018.

B. Jian, S. Beattie, S. Weyers, J. Rahm, B. Donahue, and M. Gertsvolf. GPS PPP-AR frequency transfer and its application for comparing atomic fountain primary frequency standards between NRC and PTB. Metrologia, 60(6):065002, sep 2023. doi:10.1088/1681-7575/acfa04.

K.-R. Koch. Parameter estimation and hypothesis testing in linear models. Springer Science & Business Media, 2013.

S. Koke, A. Kuhl, T. Waterholter, S. M. F. Raupach, O. Lopez, E. Cantin, N. Quintin, A. Amy-Klein, P.-E. Pottie, and G. Grosche. Combining fiber Brillouin amplification with a repeater laser station for fiber-based optical frequency dissemination over 1400 km. New J. Phys., 21(12):123017, dec 2019. doi:10.1088/1367-2630/ab5d95.

S. Kopeikin, M. Efroimsky, and G. Kaplan. Relativistic celestial mechanics of the solar system. John Wiley & Sons, 2011.

S. Kopejkin. Celestial coordinate reference systems in curved space-time. Celestial mechanics, 44(1-2):87–115, 1988.

S. Kopejkin. Relativistic manifestations of gravitational fields in gravimetry and geodesy. manuscripta geodaetica, 16(5):301–312, 1991.

J. Kusche, V. Klemann, and W. Bosch. Mass distribution and mass transport in the earth system. Journal of Geodynamics, 59:1–8, 2012.

A. Kvas, S. Behzadpour, M. Ellmer, B. Klinger, S. Strasser, N. Zehentner, and T. Mayer-Gürr. Itsg-grace2018: Overview and evaluation of a new grace-only gravity field time series. Journal of Geophysical Research: Solid Earth, 124(8):9332–9344, 2019. doi:10.1029/2019JB017415.

C. Lämmerzahl. What determines the nature of gravity? a phenomenological approach. In Probing The Nature of Gravity, pages 551–572. Springer, 2009.

C. Lämmerzahl and H. Dittus. Time, clocks and fundamental physics. International Journal of Modern Physics D, 16(12b):2455–2467, 2007.

F. W. Landerer. Hyperwall: Greenland ice mass loss 2002-2021 - nasa, Jan 2022. URL `https://svs.gsfc.nasa.gov/31156`.

K. M. Larson, R. D. Ray, F. G. Nievinski, and J. T. Freymueller. The accidental tide gauge: A gps reflection case study from kachemak bay, alaska. IEEE Geoscience and Remote Sensing Letters, 10:1200–1204, 2013. URL `https://api.semanticscholar.org/CorpusID:11995621`.

R. Le Targat, L. Lorini, Y. Le Coq, M. Zawada, J. Guéna, M. Abgrall, M. Gurov, P. Rosenbusch, D. Rovera, B. Nagórny, et al. Experimental realization of an optical second with strontium lattice clocks. Nature communications, 4(1):2109, 2013.

D. R. Leibrandt, S. G. Porsev, C. Cheung, and M. S. Safronova. Prospects of a thousand-ion sn2+ coulomb-crystal clock with sub-10- 19 inaccuracy. Nature Communications, 15(1): 5663, 2024.

A. Leick. GPS satellite surveying. Wiley, 2015.

R. Lindsey. The amazon's seasonal secret, May 2007. URL `https://earthobservatory.nasa.gov/features/AmazonLAI/amazon_lai.php`.

R. S. Lindzen and S. Chapman. Atmospheric tides. Space science reviews, 10:3–188, 1969.

G. Lion, I. Panet, P. Wolf, C. Guerlin, S. Bize, and P. Delva. Determination of a high spatial resolution geopotential model using atomic clock comparisons. Journal of Geodesy, 91(6): 597–611, 2017.

C. Lisdat, G. Grosche, N. Quintin, C. Shi, S. Raupach, C. Grebing, D. Nicolodi, F. Stefani, A. Al-Masoudi, S. Dörscher, et al. A clock network for geodesy and fundamental science. Nature communications, 7(1):1–7, 2016. doi:10.1038/ncomms12443.

C. Lisdat, J. Grotti, S. B. Koller, S. Herbers, E. Benkler, A. Al-Masoudi, R. Schwarz, S. Dörscher, N. Huntemann, R. Lange, et al. Using a transportable optical lattice clock for chronometric levelling. In Geophysical Research Abstracts, volume 21, 2019.

I. Longman. A green's function for determining the deformation of the earth under surface mass loads: 2. computations and numerical results. Journal of Geophysical Research, 68 (2):485–496, 1963.

A. E. H. Love. The yielding of the earth to disturbing forces. Proceedings of the Royal Society of London. Series A, Containing Papers of a Mathematical and Physical Character, 82(551):73–88, 1909. doi:10.1098/rspa.1909.0008.

F. Lyard, F. Lefevre, T. Letellier, and O. Francis. Modelling the global ocean tides: modern insights from fes2004. Ocean dynamics, 56:394–415, 2006.

C. J. Marone, C. Scholtz, and R. Bilham. On the mechanics of earthquake afterslip. Journal of Geophysical Research: Solid Earth, 96(B5):8441–8452, 1991.

D. D. McCarthy and B. J. Luzum. An analysis of tidal variations in the length of day. Geophysical Journal International, 114(2):341–346, 1993.

W. McGrew, X. Zhang, R. Fasano, S. Schäffer, K. Beloy, D. Nicolodi, R. Brown, N. Hinkley, G. Milani, M. Schioppo, et al. Atomic clock performance enabling geodesy below the centimetre level. Nature, 564(7734): 87–90, 2018. doi:10.1038/s41586-018-0738-2.

T. E. Mehlstäubler, G. Grosche, C. Lisdat, P. O. Schmidt, and H. Denker. Atomic clocks for geodesy. Reports on Progress in Physics, 81(6):064401, 2018.

A. Michel and J.-P. Boy. Viscoelastic love numbers and long-period geophysical effects. Geophysical Journal International, 228(2):1191–1212, 2022.

C. Misner, K. Thorne, J. Wheeler, and D. Kaiser. Gravitation. Princeton University Press, 2017. ISBN 9781400889099. URL `https://books.google.de/books?id=zAAuDwAAQBAJ`.

H.-G. Müller and U. Stadtmüller. Estimation of heteroscedasticity in regression analysis. The annals of statistics, pages 610–625, 1987.

J. Müller, M. Soffel, and S. A. Klioner. Geodesy and relativity. Journal of Geodesy, 82(3):133–145, 2008. doi:10.1007/s00190-007-0168-7.

J. Müller, D. Dirkx, S. M. Kopeikin, G. Lion, I. Panet, G. Petit, and P. Visser. High performance clocks and gravity field determination. Space Science Reviews, 214(1):1–31, 2018. doi:10.1007/s11214-017-0431-z.

R. J. Nicholls, D. Lincke, J. Hinkel, S. Brown, A. T. Vafeidis, B. Meyssignac, S. E. Hanson, J.-L. Merkens, and J. Fang. A global analysis of subsidence, relative sea-level change and coastal flood exposure. Nature Climate Change, 11(4):338–342, 2021.

V. C. Oliveira Jr, L. Uieda, K. A. Hallam, and V. CF. Should geophysicists use the gravity disturbance or the anomaly? Geophysics, 2018.

P.-A. Olsson, K. Breili, V. Ophaug, H. Steffen, M. Bilker-Koivula, E. Nielsen, T. Oja, and L. Timmen. Postglacial gravity change in fennoscandia—three decades of repeated absolute gravity observations. Geophysical Journal International, 217(2):1141–1156, 2019. doi:10.1093/gji/ggz054.

S. Ozawa, T. Nishimura, H. Suito, T. Kobayashi, M. Tobita, and T. Imakiire. Coseismic and postseismic slip of the 2011 magnitude-9 tohoku-oki earthquake. Nature, 475 (7356):373–376, 2011.

S. Ozawa, T. Nishimura, H. Munekane, H. Suito, T. Kobayashi, M. Tobita, and T. Imakiire. Preceding, coseismic, and postseismic slips of the 2011 tohoku earthquake, japan. Journal of Geophysical Research: Solid Earth, 117(B7), 2012.

R. Pail, R. Bingham, C. Braitenberg, H. Dobslaw, A. Eicker, A. Güntner, M. Horwath, E. Ivins, L. Longuevergne, I. Panet, et al. Science and user needs for observing global mass transport to understand global change and to benefit society. Surveys in Geophysics, 36(6): 743–772, 2015. doi:10.1007/s10712-015-9348-9.

W. Peltier. The impulse response of a maxwell earth. Reviews of Geophysics, 12(4):649–669, 1974. doi:10.1029/RG012i004p00649.

W. R. Peltier, D. F. Argus, and R. Drummond. Comment on “an assessment of the ice-6g_c (vm5a) glacial isostatic adjustment model” by purcell et al. Journal of Geophysical Research: Solid Earth, 123:2019–2028, 2018. doi:10.1002/2016JB013844.

D. Peng, L. Feng, K. M. Larson, and E. M. Hill. Measuring coastal absolute sea-level changes using gnss interferometric reflectometry. Remote Sensing, 13(21), 2021. ISSN 2072-4292. doi:10.3390/rs13214319.

G. Petit, B. Luzum, et al. Iers conventions (2010). 2010.

D. Philipp, E. Hackmann, and C. Laemmerzahl. Redshift and frequency comparison in schwarzschild spacetime. arXiv preprint arXiv:1711.01237, 2017.

PSMSL. Permanent service for mean sea level (psmsl), 2023, "tide gauge data", May 2023. URL `http://www.psmsl.org/data/obtaining/`.

D. Pützfeld and C. Lämmerzahl. Relativistic geodesy. Fundamental theories of physics, 2019.

G. Ramillien, J. S. Famiglietti, and J. Wahr. Detection of continental hydrology and glaciology signals from grace: a review. Surveys in geophysics, 29:361–374, 2008.

P. H. Richter. Estimating errors in least-squares fitting. The Telecommunications and Data Acquisition Report, 1995.

F. Riedel, A. Al-Masoudi, E. Benkler, S. Dörscher, V. Gerginov, C. Grebing, S. Häfner, N. Huntemann, B. Lipphardt, C. Lisdat, et al. Direct comparisons of european primary and secondary frequency standards via satellite techniques. Metrologia, 57 (4):045005, 2020.

F. Riehle. Towards a redefinition of the second based on optical atomic clocks. Comptes Rendus. Physique, 16(5):506–515, 2015.

I. Rochlin and J. T. Morris. Regulation of salt marsh mosquito populations by the 18.6-yr lunar-nodal cycle. Ecology, 98(8):2059–2068, 2017. doi:10.1002/ecy.1861.

M. Rodell and J. T. Reager. Water cycle science enabled by the grace and grace-fo satellite missions. Nature Water, 1(1):47–59, 2023.

T. Rojo, W. Brand, T. Bothwell, E. Swiler, R. Brown, and A. Ludlow. Characterization of the nist transportable yb optical lattice clock towards 10-18 level systematic uncertainty. Bulletin of the American Physical Society, 2024.

H. E. Roman. Time dilation effects on earth surface: Optical lattice clocks measurements. Physical Review D, 102(8):084064, 2020.

G. D. Rovera, M. Abgrall, C. Courde, P. Exertier, P. Fridelance, P. Guillemot, M. Laas-Bourez, N. Martin, E. Samain, R. Sherwood, J.-M. Torre, and P. Uhrich. A direct comparison between two independently calibrated time transfer techniques: T2L2 and GPS commonviews. J. Phys.: Conf. Ser., 723 (1):012037, 2016. doi:10.1088/1742-6596/723/1/012037.

A. Rülke, G. Liebsch, M. Sacher, U. Schäfer, U. Schirmer, and J. Ihde. Unification of european height system realizations. Journal of geodetic science, 2(4):343–354, 2012.

R. Rummel. Height unification using goce. Journal of geodetic science, 2 (4):355–362, 2012.

R. Rummel and P. Teunissen. Height datum definition, height datum connection and the role of the geodetic boundary value problem. Bulletin géodésique, 62:477–498, 1988.

L. Ryder. Introduction to General Relativity. Cambridge University Press, 2020. ISBN 9781139478229. URL `https://books.google.de/books?id=7fA8gIaZN80C`.

L. Sánchez. Towards a vertical datum standardisation under the umbrella of global geodetic observing system. Journal of Geodetic Science, 2(4): 325–342, 2012.

L. Sánchez. Unification of height systems in the frame of ggos. In EGU2015, Vienna, Austria, 2015.

L. Sánchez, J. Ågren, J. Huang, Y. M. Wang, J. Mäkinen, R. Pail, R. Barzaghi, G. S. Vergos, K. Ahlgren, and Q. Liu. Strategy for the realisation of the international height reference system (ihrs). Journal of Geodesy, 95 (3):1–33, 2021.

L. Sánchez, H. Wziontek, Y. M. Wang, G. Vergos, and L. Timmen. Towards an integrated global geodetic reference frame: preface to the special issue on reference systems in physical geodesy. Journal of Geodesy, 97(6): 59, 2023.

R. Savcenko and W. Bosch. Eot11a-a new tide model from multi-mission altimetry. In Proceedings of the OSTST Meeting, pages 19–21, 2011.

B. G. Schmidt. Einstein's Field Equations and Their Physical Implications: Selected Essays in Honour of Jürgen Ehlers, volume 540. Springer Science & Business Media, 2000.

R. Schroder, U. Hubner, and D. Griebsch. Design and realization of the microwave cavity in the ptb caesium atomic fountain clock csf1. IEEE transactions on ultrasonics, ferroelectrics, and frequency control, 49(3):383–392, 2002.

S. Schröder, S. Stellmer, and J. Kusche. Potential and scientific requirements of optical clock networks for validating satellite-derived time-variable gravity data. Geophysical Journal International, 226(2):764–779, 2021. doi:10.1093/gji/ggab132.

M. Shamsudduha and D. K. Panda. Spatio-temporal changes in terrestrial water storage in the himalayan river basins and risks to water security in the region: A review. International Journal of Disaster Risk Reduction, 35: 101068, 2019. ISSN 2212-4209. doi:https://doi.org/10.1016/j.ijdrr.2019.101068. URL https://www.sciencedirect.com/science/article/pii/S2212420919300615.

L. Sharma, H. Rathore, S. Utreja, A. Roy, S. De, S. Panja, et al. Optical atomic clocks for redefining si units of time and frequency. MAPAN, 35(4): 531–545, 2020. doi:10.1007/s12647-020-00397-y.

Z. Shen, W. Shen, X. Xu, S. Zhang, T. Zhang, L. He, Z. Cai, S. Xiong, and L. Wang. A method for measuring gravitational potential of satellite's orbit using frequency signal transfer technique between satellites. Remote Sensing, 15(14), 2023a. ISSN 2072-4292. doi:10.3390/rs15143514. URL https://www.mdpi.com/2072-4292/15/14/3514.

Z. Shen, W. Shen, S. Zhang, C. K. Shum, T. Zhang, L. He, Z. Cai, S. Xiong, and L. Wang. Unification of a global height system at the centimeter-level using precise clock frequency signal links. Remote Sensing, 15(12), 2023b. ISSN 2072-4292. doi:10.3390/rs15123020. URL https://www.mdpi.com/2072-4292/15/12/3020.

S. Shibahara. The 2011 tohoku earthquake and devastating tsunami. The Tohoku journal of experimental medicine, 223(4):305–307, 2011.

M. Shirzaei, J. Freymueller, T. E. Törnqvist, D. L. Galloway, T. Dura, and P. S. Minderhoud. Measuring, modelling and projecting coastal land subsidence. Nature Reviews Earth & Environment, 2(1):40–58, 2021.

M. Sideris, F. Willi, N. Zuhair, and S. Thomas. Geodetic world height system unification. Handbook of geomathematics, pages 1–16, 2014.

M. Soffel. Space-time reference systems. Springer, 2013.

H. Steffen and P. Wu. Glacial isostatic adjustment in fennoscandia—a review of data and modeling. Journal of geodynamics, 52(3-4):169–204, 2011.

M. Steinel, H. Shao, M. Filzinger, B. Lipphardt, M. Brinkmann, A. Didier, T. Mehlstäubler, T. Lindvall, E. Peik, and N. Huntemann. Evaluation of a sr+ 88 optical clock with a direct measurement of the blackbody radiation shift and determination of the clock frequency. Physical Review Letters, 131(8):083002, 2023.

T. Sun, K. Wang, T. Iinuma, R. Hino, J. He, H. Fujimoto, M. Kido, Y. Osada, S. Miura, Y. Ohta, et al. Prevalence of viscoelastic relaxation after the 2011 tohoku-oki earthquake. Nature, 514(7520):84–87, 2014.

L. Sánchez and M. G. Sideris. Vertical datum unification for the International Height Reference System (IHRS). Geophysical Journal International, 209(2): 570–586, 01 2017. ISSN 0956-540X. doi:10.1093/gji/ggx025. URL https://doi.org/10.1093/gji/ggx025.

M. Takamoto and H. Katori. Optical lattice clocks and related platforms. In Quantum Photonics, pages 449–480. Elsevier, 2024.

M. Takamoto, Y. Tanaka, and H. Katori. A perspective on the future of transportable optical lattice clocks. Applied Physics Letters, 120(14): 140502, 2022. doi:10.1063/5.0087894.

Y. Tamura, T. Sato, M. Ooe, and M. Ishiguro. A procedure for tidal analysis with a bayesian information criterion. Geophysical Journal International, 104(3):507–516, 1991.

B. D. Tapley, M. M. Watkins, F. Flechtner, C. Reigber, S. Bettadpur, M. Rodell, I. Sasgen, J. S. Famiglietti, F. W. Landerer, D. P. Chambers, et al. Contributions of grace to understanding climate change. Nature climate change, 9(5):358–369, 2019. doi:10.1038/s41558-019-0456-2.

W. M. Telford, L. P. Geldart, and R. E. Sheriff. Applied geophysics. Cambridge university press, 1990.

A. Tofful. Advances in performance and automation of a single ytterbium ion optical clock. PhD thesis, Imperial College London, 2023.

W. Torge, J. Müller, and R. Pail. Geodesy. De Gruyter Oldenbourg, Berlin, Boston, 2023. ISBN 9783110723304. doi:doi:10.1515/9783110723304.

P. Tregoning, C. Watson, G. Ramillien, H. McQueen, and J. Zhang. Detecting hydrologic deformation using grace and gps. Geophysical Research Letters, 36(15), 2009.

S. Unjoh, M. Kaneko, S. Kataoka, K. Nagaya, and K. Matsuoka. Effect of earthquake ground motions on soil liquefaction. Soils and Foundations, 52(5):830–841, 2012.

T. van Dam and J. Wahr. Displacements of the earth's surface due to atmospheric loading: Effects on gravity and baseline measurements. Journal of Geophysical Research: Solid Earth, 92(B2):1281–1286, 1987.

T. van Dam, J. Wahr, Y. Chao, and E. Leuliette. Predictions of crustal deformation and of geoid and sea-level variability caused by oceanic and atmospheric loading. Geophysical Journal International, 129(3):507–517, 1997.

I. Velicogna. Increasing rates of ice mass loss from the greenland and antarctic ice sheets revealed by grace. Geophysical Research Letters, 36 (19), 2009.

O. Vestøl, J. Ågren, H. Steffen, H. Kierulf, and L. Tarasov. Nkg2016lu: a new land uplift model for fennoscandia and the baltic region. Journal of Geodesy, 93:1759–1779, 2019.

A. Vincent and J. Müller. Vision of a clock-based network for absolute sea level monitoring. Springer, 2024.

A. Vincent and J. Müller. Detection of time variable gravity signals using terrestrial clock networks. Advances in Space Research, 2023. ISSN 0273-1177. doi:10.1016/j.asr.2023.07.058.

A. Vincent, J. Müller, C. Lisdat, and D. Philipp. Realization of a clock-based global height system: A simulation study for europe and brazil, 2025. URL https://arxiv.org/abs/2411.07888.

C. Voigt, H. Denker, and L. Timmen. Time-variable gravity potential components for optical clock comparisons and the definition of international time scales. Metrologia, 53 (6):1365, 2016. doi:10.1088/0026-1394/53/6/1365.

J. Wahr. Earth tides. Global Earth physics, AGU Reference Shelf, 1 (1995):40–45, 1995.

J. Wahr, M. Molenaar, and F. Bryan. Time variability of the earth's gravity field: Hydrological and oceanic effects and their possible detection using grace. Journal of Geophysical Research: Solid Earth, 103(B12): 30205–30229, 1998.

J. Wahr, S. Swenson, and I. Velicogna. Accuracy of grace mass estimates. Geophysical Research Letters, 33(6), 2006.

J. M. Wahr. Deformation induced by polar motion. Journal of Geophysical Research: Solid Earth, 90(B11): 9363–9368, 1985.

R. Wald. General Relativity. University of Chicago Press, 2010. ISBN 9780226870373. URL https://books.google.de/books?id=9S-hzg6-moYC.

Y. M. Wang. Geodetic boundary value problems. Encyclopedia of Geodesy. Switzerland: Springer International Publishing (Outside the USA), 2016.

H.-G. Wenzel. Eterna - programs for tidal analysis and prediction, 2022.

K. Wilhelm and B. N. Dwivedi. On the gravitational redshift. New Astronomy, 31:8–13, 2014.

P. A. Williams, W. C. Swann, and N. R. Newbury. High-stability transfer of an optical frequency over long fiber-optic links. JOSA B, 25(8):1284–1293, 2008.

P. Woodworth and R. Player. The permanent service for mean sea level: An update to the 21stcentury. Journal of Coastal Research, pages 287–295, 2003.

P. Woodworth, C. Hughes, R. Bingham, and T. Gruber. Towards worldwide height system unification using ocean information. Journal of Geodetic Science, 2(4):302–318, 2012.

H. Wu and J. Müller. Towards an international height reference frame using clock networks. In J. T. Freymueller and L. Sánchez, editors, Beyond 100: The Next Century in Geodesy, pages 3–10, Cham, 2022. Springer International Publishing. ISBN 978-3-031-09857-4.

H. Wu, J. Müller, and C. Lämmerzahl. Clock networks for height system unification: a simulation study. Geophysical Journal International, 216(3):1594–1607, 11 2018. ISSN 0956-540X. doi:10.1093/gji/ggy508. URL https://doi.org/10.1093/gji/ggy508.

K. Wu, W.-B. Shen, X. Sun, C. Cai, and Z. S. and. Measuring the gravity potential between two remote sites with cvstt technique using two hydrogen clocks. Geo-spatial Information Science, 27(5):1719–1738, 2024. doi:10.1080/10095020.2023.2231515. URL https://doi.org/10.1080/10095020.2023.2231515.

G. Wöppelmann and M. Marcos. Vertical land motion as a key to understanding sea level change and variability. Reviews of Geophysics, 54(1):64–92, 2016. doi:10.1002/2015RG000502.

H. J. Zwally, W. Abdalati, T. Herring, K. Larson, J. Saba, and K. Steffen. Surface melt-induced acceleration of greenland ice-sheet flow. Science, 297 (5579):218–222, 2002.

Acknowledgement

With immense gratitude, I would first like to express my heartfelt thanks to my supervisor, Prof. Dr.-Ing. habil. Jürgen Müller, for his constant guidance, support, and understanding from the very beginning of my research journey. His encouragement fostered my ability to think independently in a stimulating work environment and strengthened my self-esteem by motivating me to attend various conferences, which significantly shaped my academic perspective and research approach.

I am also deeply grateful to Prof. Dr. rer. nat. Claus Lämmerzahl for serving as my co-supervisor, providing valuable support and insightful comments throughout this project. Additionally, I extend my sincere thanks to Prof. Dr.-Ing. habil. Monika Sester for being my ancillary supervisor.

A special note of appreciation goes to Dr.-Ing. Hu Wu, whose guidance in the early stages of my Ph.D. was instrumental in helping me understand the theoretical foundations. His mentorship and support were invaluable as I integrated into a great research team.

This work was carried out as part of the joint collaborative initiative Relativistic and Quantum-based Geodesy 'TerraQ' (SFB-1464), specifically within project C02: Atomic Clocks – Fundamental Physics and Applications. I am truly grateful to the TerraQ team for providing me with the opportunity to conduct my research in such a well-organized and enriching environment. I also acknowledge the Deutsche Forschungsgemeinschaft (DFG) for its financial support, throughout the research period.

I extend my sincere gratitude to Ms. Petra Heldt-Bertrand and Dr. Mona Weyrauch for their invaluable support in joining from India and facilitating my transition to Germany during the COVID-19 pandemic, assisting with accommodation, administrative matters, and overall well-being. My appreciation also goes to Ms. Britta Michaela Frankel and Dr.-Ing. Raúl Villanueva Granados for their financial and administrative assistance, which helped me navigate various official processes smoothly.

I also thank my colleagues Dr.-Ing. Minguye Zhang and Dr.-Ing. Alexey Kupriyanov, whose collaboration and enthusiasm made this journey more inspiring and enjoyable.

Above all, I am deeply grateful to my wonderful and loving family, Pappa, Mommy, Achettai, Sonamol, Kunjanja, Ginumol, dear Isakutty, and my love and love only, for their unwavering support and encouragement throughout this journey. Their presence filled this time with longing, joy, laughter, fights, and even sorrow - all of which gave this chapter of my life its true depth and meaning.

This work is lovingly dedicated to my Kunjanja, my strongest pillar of support, who taught me to stand tall and explore without fear. Your strength, spirit, and love remain with me always.

Curriculum Vitae

Personal Information

Name: Asha Vincent

Date of Birth: 17.01.1996

Place of Birth: Kerala, India

Nationality: Indian

Mail: vincent@ife.uni-hannover.de

Work Experience

2021 – Present: Research Assistant

Institute for Geodesy, Leibniz University Hannover, Germany
TerraQ, SFB 1464, project C02 titled 'Terrestrial Clock Networks: Fundamental Physics and Applications'

2019 – 2021: Project Assistant

CSIR – 4PI, Bangalore, India
GAP1016 project titled 'Assessment of Regional Hydrology using Spaceborne Gravity Observations' (Department of Science &Technology)

Education

Since 09.2021: Ph.D. candidate in Relativistic Geodesy

Institute for Geodesy, Leibniz University Hannover, Germany

2018 – 2019: Post Graduate Diploma in Remote Sensing and GIS (Photogrammetry and Remote Sensing)

Indian Institute of Remote Sensing, ISRO, Dehradun, Uttarakhand, India

2016 – 2018: MSc. Physics

Loyola College Chennai, University of Madras, Tamil Nadu, India

2013 – 2016: BSc. Physics

Mahatma Gandhi University, Kottayam, Kerala, India

Wissenschaftliche Arbeiten der Fachrichtung Geodäsie und Geoinformatik der Leibniz Universität Hannover

(Eine vollständige Liste der Wiss. Arb. ist beim Geodätischen Institut, Nienburger Str. 1, 30167 Hannover erhältlich.)

Nr. 384	ZOURLIDOU, Stefania:	Traffic Regulation Recognition from GPS Data (Diss. 2023)
Nr. 385	SLEDZ, Artuom:	Thermal anomaly detection based on information fusion from optical and infrared images (Diss. 2023)
Nr. 386	WITTICH, Dennis:	Deep Domain Adaptation for the Pixel-wise Classification of Aerial and Satellite Images (Diss. 2023)
Nr. 387	SINGH, Vishwa Vijay:	Lunar Laser Ranging - Improved Modelling and Parameter Estimation (Diss. 2023)
Nr. 388	HARTMANN, Jens:	Hochgenaue 3D-Erfassung von Großstrukturen durch kinematisches terrestrisches Laserscanning (Diss. 2023)
Nr. 389	ZHUGE, Xia:	Characterizing slope instability kinematics by integrating multi-sensor satellite remote sensing observations (Diss. 2023)
Nr. 390	DOROZYNSKI, Mareike Marianne:	Image Classification and Retrieval in the Context of Silk Heritage using Deep Learning (Diss. 2023)
Nr. 391	KNABE, Annike:	New Concepts for Gravity Field Recovery using Satellites (Diss. 2023)
Nr. 392	KALIA, Andre:	Landslide activity detection based on nationwide Sentinel-1 PSI datasets (Diss. 2023)
Nr. 393	BROCKMEYER, Marco:	Modellierung von Bodenbewegungen anhand heterogener Messverfahren am Beispiel der niedersächsischen Landesfläche (Diss. 2023)
Nr. 394	ZHANG, Mingyue:	Characteristics and Benefits of Differential Lunar Laser Ranging (Diss. 2023)
Nr. 395	DENNIG, Dirk:	Entwicklung eines kinematischen Profilvermessungssystems am Beispiel Kranbahnvermessung (Diss. 2024)
Nr. 396	FUEST, Stefan:	Nudging travelers to societally favorable routes by means of cartographic symbolization (Diss. 2024)
Nr. 397	MOFTIZADEH, Rozhin:	Advanced Particle Filtering for Vehicle Navigation based on Collaborative Information (Diss. 2024)
Nr. 398	VASSILEVA, Magdalena Stefanova:	Satellite Radar Interferometry for Geohazards: from ground deformation to processes understanding (Diss. 2024)
Nr. 399	MALINOVSKAYA, Anna:	Statistical Process Monitoring of Networks (Diss. 2024)
Nr. 400	BANNERT, Jörn:	Der Einfluss von Straßenverkehrslärm und Umgehungsstraßen auf Grundstücks-werte in Ortslagen - Bestimmung mittels Expertenbefragung nach der Delphi-Methode (Diss. 2024)
Nr. 401	AXMANN: Jeldrik:	Maximum consensus localization using LiDAR (Diss. 2024)
Nr. 402	TENNSTEDT, Benjamin:	Concept and Evaluation of a Hybridization Scheme for Atom Interferometers and Inertial Measurement Units (Diss. 2024)
Nr. 403	HAKE, Frederic:	Schadenserkennung an Bauwerken mittels maschinellem Lernens (Diss. 2025)
Nr. 404	KARIMIDOONA, Ali:	On Integrity Prediction for Network-RTK Positioning in Urban Environments (Diss. 2025)
Nr. 405	ORTEGA, Mabel:	Domain Adaptation for Deforestation Detection in Remote Sensing: Addressing Class Imbalance and Performance Estimation (Diss. 2025)
Nr. 406	KUPRIYANOV, Alexey:	Investigation of Optical Accelerometry and Novel Satellite Formations for Future Gravimetry Missions (Diss. 2025)
Nr. 407	BREVA, Yannick:	On the Observation Quality of Robot-based GNSS Antenna Calibration for Determining Codephase Corrections (Diss. 2025)
Nr. 408	GUO, Zelong:	Co- and Post-seismic Slip Models Inferred from InSAR Geodesy (Diss. 2025)
Nr. 409:	YUAN, Yunshuang:	Collective Perception: A Fully-Sparse Deep Learning Framework for Multi-Agent Data Fusion (Diss. 2025)
Nr. 410	SU, Jingyao:	Towards interval-based autonomous integrity monitoring: Error bounding and uncertainty propagation (Diss. 2025)
Nr. 411	VINCENT, Asha:	Clock Networks for Geodetic Applications (Diss. 2025)